Shaping surface waves for diagnostics

Yannyk Parulian Julian Bourquin

Submitted in the fulfilment of the requirements for the
Degree of Doctor of Philosophy

School of Engineering
College of Science and Engineering
University of Glasgow

December 2012

Abstract

Infectious diseases continue to kill millions of people every year and are a significant burden on the socio-economic development of developing countries. After many years of international policy aimed at containing diseases, it has recently become an explicit aim to move towards elimination of infectious diseases. However, if this is to occur, it will be necessary to have highly efficacious diagnostic tools to ensure infected individuals are identified and treated. However, the diagnosis of infectious diseases in the developed and developing world requires the full integration of complex assays in easy-to-use platforms with robust analytical performances at low cost. Many relevant bioanalytical technologies have been developed for use in laboratories and clinics, including the current gold standard for the diagnosis of tuberculosis and malaria.

The miniaturization and integration of complex functions into lab-on-a-chip (LOC) technologies using microfluidics have only had limited success in translating diagnosis assays out of a centralized laboratory to point-of-care (POC) settings, because they still remain constrained due to chip interconnection and they are either not likely to go out of research laboratories or are not appropriate for low resource settings.

In this thesis, a new microfluidic platform was developed that reduced the dependency of the diagnostic procedure on large laboratory instruments providing simplicity of use, enabling the patient sample to be processed and diagnosed on a low cost, disposable biochip. Surface acoustic wave (SAW) devices, which are commonly used in mobile phone technologies, were adapted to provide controlled microfluidic functions by shaping the SAW using particular designs of electrodes and phononic structures.

The control of lateral positioning of the SAW was demonstrated using a slanted finger interdigitated transducer (IDT) in a frequency tuneable manner allowing microfluidic functions such as mixing, moving and merging, sequentially performed using a single IDT both on the substrate and on a disposable chip. Alternatively, phononic bandgaps were designed to break the symmetry of the SAW in a tuneable manner and gradient index phononic crystals (GRIN-PC) lenses were designed to focus the SAW and successfully increased the amplitude of the wave by a factor 3 while the focal position could be tuned with the frequency.

The potential of these techniques was demonstrated by controlling the amplitude and direction of water jet towers by the use of a phononic horn structure that allowed the enhancement of energy at defined positions and by propelling and directing a

macrometer scale object in water using a slanted IDT.

As proof of concepts of diagnostic devices for the developing world, an immunoassay for tuberculosis using only mobile phone technologies (SAW, light-emitting diode (LED) and complementary metaloxidesemiconductor (CMOS) camera) was demonstrated with a limit of detection of 1 pM, which is the limit required in an interferon-γ release assay. This limit of detection was only achievable because of the ability of SAW to increase the mixing and to reduce the non-specific binding. Furthermore, a method to enrich malaria infected cells, based on SAW and isopycnic gradient, was also demonstrated and showed an enrichment up to 100x in the equivalent of a fingerprick of blood in 3 seconds. This technique will allow to reduce the limit of detection of the current gold standard.

This platform not only opens a clear road toward POC diagnostics due to its size, cost, versatility and ease in integration, but has also the potential to provide useful tools in laboratory settings for large scale, high-throughput technologies.

Publications

1. **Yannyk Bourquin** et al., Focusing surface waves using a gradient index phononic crystals lens, 2012, *submitted*.

2. **Yannyk Bourquin** et al., Surface Acoustic Waves Isopycnic Enrichment of Plasmodium falciparum for Low Cost Diagnostics, 2012, *submitted*.

3. **Yannyk Bourquin** and Jonathan M. Cooper, Swimming Using Surface Acoustic Waves, *PLoS One*, 8(2):e42686, 2013.

4. Julien Reboud, **Yannyk Bourquin** et al., Shaping Acoustic Fields as a Toolset for Microfluidic Manipulations in Diagnostic Technologies, *Proceedings of the National Academy of Sciences*, 109(38):15162-15167, 2012.

5. Julien Reboud, Rab Wilson, Yi Zhang, Mohd H Ismail, **Yannyk Bourquin** and Jonathan M Cooper, Nebulization on a disposable array structured with phononic lattices, *Lab on a Chip*, 12:1268-1273, 2012.

6. **Yannyk Bourquin** et al., Phononic Crystals for Shaping Fluids, *Advanced Materials*, 23:14581462, 2011. Highlighted by *Nature Materials*, 10:264, 2011.

7. **Yannyk Bourquin** et al., Integrated immunoassay using tuneable surface acoustic waves and lensfree detection, *Lab on a Chip*, 11:2725-2730, 2011.

8. Rab Wilson, Julien Reboud, **Yannyk Bourquin** et al., Phononic Crystal Structures for Acoustically-Driven Microfluidic Manipulations, *Lab on a Chip*, 11:323-328, 2011.

9. **Yannyk Bourquin** et al., Tuneable surface acoustic waves for fluid and particle manipulations on disposable chips, *Lab on a Chip*, 10:1898-1901, 2010.

Conferences/Seminars

1. **Yannyk Bourquin**, Surface Acoustic Waves for Travelling in the Microworld, *Set for Britain*, House of Parliament, London, UK, 2012, poster presentation.

2. **Yannyk Bourquin** et al., Phonofluidics, *Lorentz workshop on Acoustic Waves for the Control of Microfluidics Flows*, Leiden, The Netherlands, 2012, poster presentation.

3. **Yannyk Bourquin**, Shaping Acoustic Waves for microfluidics, Nationa Tsing Hua University, Taiwan, 2011, invited lecture.

4. **Yannyk Bourquin**, Using Surface Acoustic Waves for to Drive Microfluidics, Tianjin University, Tianjin, China, 2011, invited lecture.

5. **Yannyk Bourquin** et al., Low cost diagnostic device using mobile phone technologies, *the 6th UKRI PG Biomed*, Glasgow, UK, 2011, oral presentation.

6. **Yannyk Bourquin** et al. Shaping Acoustic Waves for Fluid Manipulation, *Gordon Research Conference (GRC) in Physics and Chemistry of Microfluidics*, Waterville Valley (NH), US, 2011, poster presentation.

Contents

List of Tables

List of Figures

Acknowledgement

I would like first to thank Prof. Jon Cooper for giving me the opportunity to carry out this research within his group. His advice and guidance have been invaluable.

Acknowledgements also go to the members of the group I had the chance to interact with. Thanks in particular to Dr. Rab Wilson, Dr. Yi Zhang, Dr. Julien Reboud, Dr. Manlio Tassieri, Dr. Andrew Glidle, Abeer Syed, Christian Witte, Dr. Shelley Li and Chiara Martino for the fruitful discussions and their advices.

A special thank to Pr. Xia Xiao and Pr. Tsung-Tsong Wu, who kindly invited me to visit their labs during my PhD as well as the members of their groups.

Finally and most importantly, to my parents François-Thierry and Marince, my brother Edo, my two sisters Zubaidah and Naomi and my niece Layna for their infinite support.

Author's Declaration

The work presented in this thesis was conducted by the author and has not previously been submitted for a degree or diploma at this university or any other institution.

Yannyk Bourquin

Abbreviations

A_0	first antisymmetric
Ab	antibody
BCG	bacille Calmette-Guerin
BSA	bovine serum albumin
CAD	computer aided design
CCD	charge-coupled device
CMOS	complementary metal-oxide-semiconductor
DI	deionized
EDC	1-ethyl-3-(3-dimethylaminopropyl)carbodiimide
ELISA	enzyme-linked immunosorbent assay
FE	finite-element
ff	filling fraction
FHWM	full half width maximum
GRIN-PC	gradient-index phononic crystal
IDT	interdigitated transducers
IFN	interferon
IGRA	interferon gamma realease assay
IR	infrared
iRBC	infected red blood cell
LDV	laser Doppler vibrometer
LED	light-emitting diode
LOC	Lab-on-a-chip
LOD	limit of detection
MAb	monoclonal antibody
MDR-TB	multiple drug-resistant tuberculosis
MES	2-(N-morpholino)ethanesulfonic acid
MRDT	malaria rapid diagnosis tests
PBC	periodic boundary condition
PBS	phosphate buffered saline
PDMS	polydimethylsiloxane
PC	phononic crystal
PCR	polymerase chain reaction

POC	Point-of-care
RBC	red blood cell
Re	Reynolds number
Re_A	acoustic Reynolds number
RPMI	Roswell Park Memorial Institute medium
S_0	first symmetric
SAW	surface acoustic wave
SEM	scanning electron micrograph
SFIDT	slanted finger interdigitated transducer
SH-SAW	shear-horizontal surface acoustic wave
SPR	surface plasmon resonance
SW	surface wave
TB	tuberculosis
TST	tuberculin skin test
UST	ultrasonic thrusters
UV	ultraviolet
VSWR	voltage standing wave ratio
We	Weber number

Chapter 1

Introduction

In this chapter, the burden of infectious diseases in the developing world as well as the current diagnosis standard is first described with a particular attention on malaria and tuberculosis. The field of Lab-on-a-chip and Point-of-care diagnostics is introduced to show their potential application in the diagnostic of infectious diseases in ressource limited settings. Then, reviews of surface acoustic waves based microfluidic functions and phononic crystals applications are given. Finally, the motivations and objectives of this thesis are described.

1.1 Infectious diseases and diagnostics

Infectious diseases are transmissible diseases resulting from the presence in the body of pathogenic agents, such as viruses, bacteria and parasites. Every year, almost 1 million people, mostly children, die from malaria, 2.8 million from AIDS and 1.6 million from tuberculosis [144]. Hundreds of thousands of deaths also result due to other sexually transmitted infections (e.g. hepatitis B) and tropical parasitic infections [144]. In total, infectious diseases are responsible of 14 millions deaths each year and the majority of these deaths (95%) happen in developing countries. Accurate, sensitive and cheap diagnostic tests are necessary to combat these diseases, but are generally unavailable [144].

For most infectious diseases in developing countries, laboratory-based tests exist, although they are not accessible to the majority of the population. The current diagnostics techniques used to detect parasitic and mycobacterial infections still depend either upon visual identification with microscopy or serological identification. Both

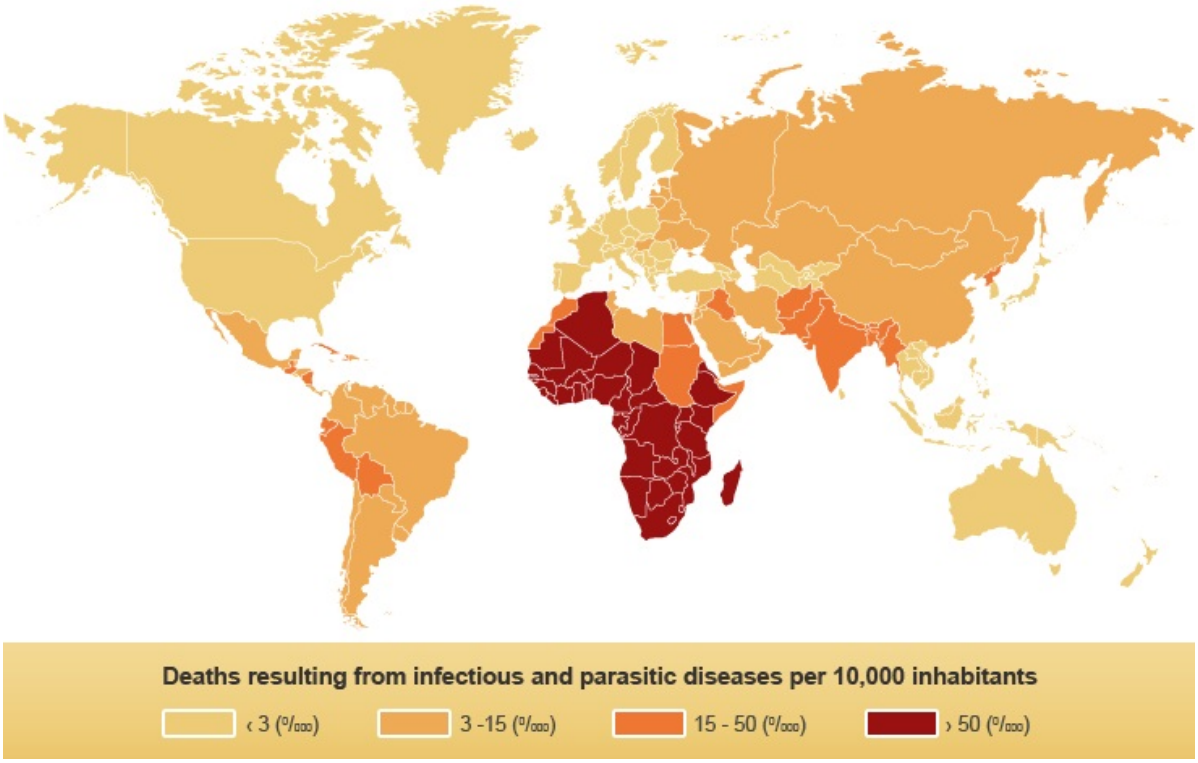

Figure 1.1: Burden of infectious diseases in the world. (World Health Report 2006, Millennium Goals)

methods require well-trained technologists. Various biomarker approaches have recently added to this capability, although these techniques again often involve complex laboratory instrumentation [159].

Point-Of-Care (POC) tests are already available in the market for infectious diseases such as AIDS, malaria and syphilis. These tests need to be cheap to fabricate, simple to perform and generate rapid visual readouts. However, most of these POC tests fail to meet the needs of disease-endemic areas mainly because of the poor sensitivity and the high cost [159].

1.1.1 Malaria

Malaria is an infectious disease caused by four species of parasites called *Plasmodium falciparum*, *Plasmodium vivax*, *Plasmodium ovale* and *Plasmodium malariae*. *Plasmodium falciparum* and *Plasmodium vivax* are the most common, but *Plasmodium falciparum* is also the most deadly. Malaria is transmitted exclusively through the bites of Anopheles mosquitoes and most of the cases and deaths occur in sub-tropical countries. The disease causes serious illness in over 500 million people every year and over 1 million deaths a year, from which 90 % occur in Sub-Saharan Africa [115, 145, 46].

The life cycle of malaria parasites in the human body starts when a mosquito infects

a person by taking a meal (blood). The parasites in sporozoite stage go into the bloodstream and migrate to the liver. They infect hepatocytes where they proliferate into merozoites, break the hepatocytes and are released into the bloodstream. Afterwards, the merozoites infect red blood cells (RBC), where they develop into the ring forms, followed by a feeding stage called the trophozoites, a reproduction stage called schizonts, and then, back into merozoites. During these stages, the mechanical properties of the infected red blood cells (iRBC) evolve. RBCs have a particular biconcave shape and a high flexibility. The iRBCs become stiff, slightly less dense, and their volume changes during the different stages [14, 54, 44, 120].

The symptoms of this disease (fever, headache, chills and vomiting) appear at least one week after the infective mosquito bite and may be mild and not easy to diagnose as malaria. Thus, an early diagnosis technique is needed to be able to give the appropriate treatment. This would prevents deaths and also contributes to reducing malaria transmission [7].

The diagnosis of malaria involves identification of malaria parasite or its antigens in the blood of the patient. The efficacy of the diagnosis is subject to many limiting factors: the different species (requiring different treatments), the different stages in the blood and the sequestration of the parasites in the small blood vessels. So far, the gold standard for the diagnosis of malaria is the microscopic examination of blood films. It permits the screening of a large volume of blood and an experienced microscopist is able to detect parasite levels as low as 100 parasites per μl for a thin smear and 10 parasites per μl for a thick smear [89]. The time needed for such screening is around 40 min. The problems with this method is the need of a laboratory with well-trained technicians and the time required for the analysis. Most of the people in developing country do not have access to this type of diagnosis.

Therefore, malaria rapid diagnosis tests (MRDT) are needed in endemic area. Unfortunately, current MRDTs, including immunochromatographic tests, have many limitations making them not effective in the field. So far, they fail to detect mixed infections and detect infections with low but clinically relevant concentrations of parasites (below 200 parasites per μl) [143, 89, 79, 1].

1.1.2 Tuberculosis

Tuberculosis (TB) is a infectious disease caused by a mycobacteria, *Mycobacterium tuberculosis*. It commonly attacks the lungs and it is spread when infected people

cough or sneeze. Most of the cases of infections are asymptomatic and latent (90%), but they eventually progress to active disease. In such a case the infected patient has only 50% of chance to survive, if not treated [146]. The typical symptoms of active TB infection are cough with blood, fever, night sweats and weight loss.

The treatment of TB requires administration of antibiotics over a long period of time (6 months). Antibiotic resistance is a growing issue in multiple drug-resistant tuberculosis (MDR-TB) infections (4% of the infections in 2010) [55]. The prevention of TB relies on the early diagnostics of the infection and the vaccination.

In 2010, there were an estimated 8.8 million new cases and 1.7 million associated deaths, mainly occurring in developing countries (6500 case in the UK) and in jails. In fact, the proximity and low hygiene in jails increase the rate of tranmission. The high rate of HIV infection in developing country also increases the possibility of contracting the disease. Those who are infected by HIV are 50 times more likely to develop active tuberculosis; 230 thousand of the deaths are from people who are also infected by HIV [85, 49, 41].

The gold standard for the diagnosis of active TB relies on microscopic examination and microbiological culture of body fluids and radiology (chest X-rays) [5, 111]. For latent TB, the Mantoux tuberculin skin test (TST) is generally performed although it shows up to 40% false-positive, especially for people vaccinated with the bacille Calmette-Guerin (BCG) vaccine [114, 106]. For this reason, a blood test is usually performed for the patient positive to the Mantoux test. The interferon gamma release assay (IGRA) is thus performed. It consists in stimulating the T-cells of the patient using an antigen specific to the mycobacteria; if the patient has been in contact with the mycobacteria, the T-cells will release a large quantity of interferon gamma which is detected using an enzyme-linked immunosorbent assay (ELISA) [56, 97, 98, 95].

IGRA kits are available commercially, however they still require a technician and cost around 20 $ [93]. They also require the performance of a cell-based assay and are not suitable for developping countries. Moving this type of test into a low cost point-of-care setting would allow access to this technology to a larger population, although there are significant obstacles.

1.2 Lab-on-a-chip and Point-of-care Diagnostics

The miniaturization and integration of complex functions into lab-on-a-chip (LOC) have already had success in translating diagnosis assays out of a centralized laboratory

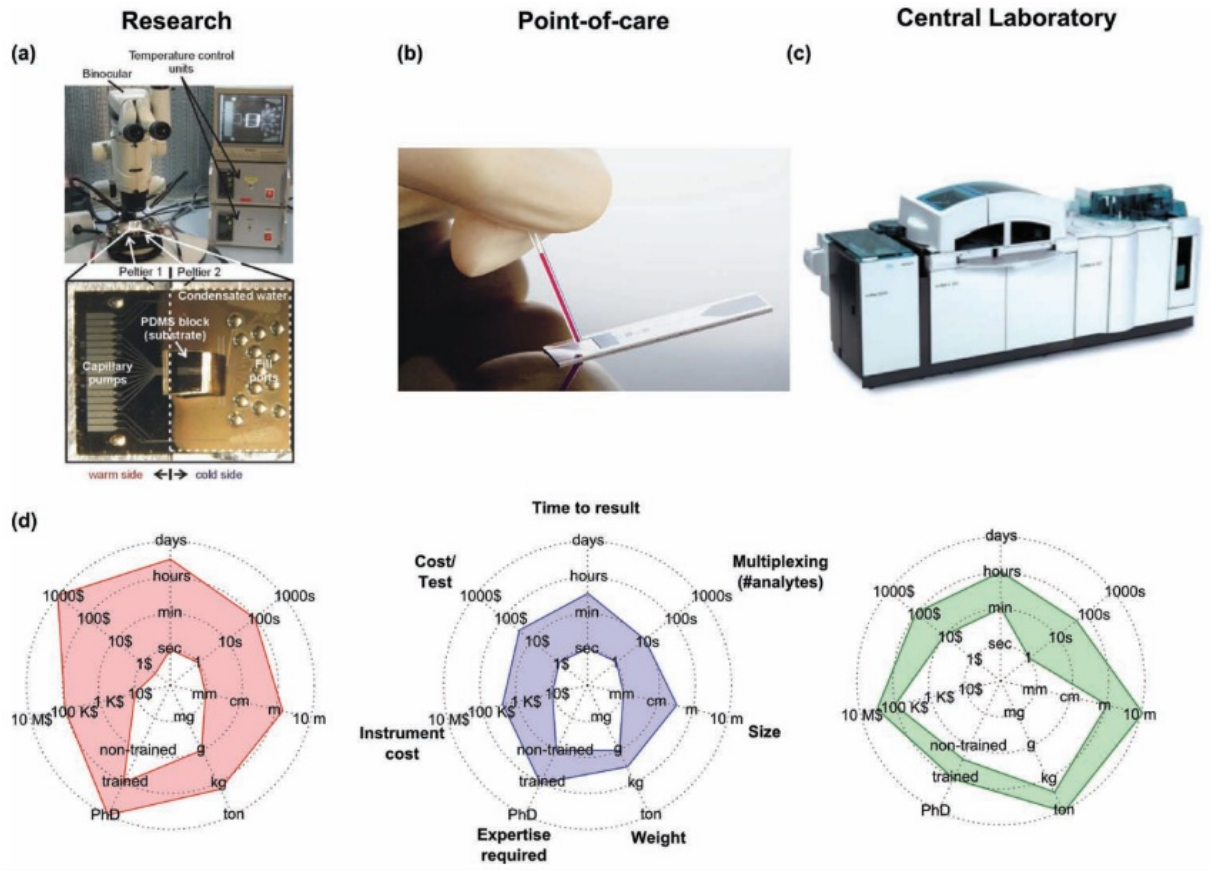

Figure 1.2: Comparison in the requirements for biological analysis in research, point-of-care and central laboratory diagnostics settings. (a) An example of a research microfluidics platform is shown. It requires peripherals such as a microscope, computer, temperature and humidity control and pumps. (b) The POC device is small and requires a peripheral reader. (c) The central laboratory platform provides over 80 ready to use tests and the system is large. (d) Radar charts illustrating the tradeoffs for each biological analysis platform. (Gervais et al., 2011)

to POC settings, for example with the measurement of glucose levels by diabetics. In the field of infectious disease diagnostics, where detection of markers at the pM level is required, lateral-flow immunochromatographic strips, which are based on transport of fluid using capillary forces, have also found applications. However, this technology has shown some limitations in sensitivity (30 pM in laboratory)[43] and in the integration of complex diagnostics procedures [160, 159]. Other immunoassay technologies, with high detection limits (up to the fM level) have been developed in laboratories [86, 19, 92], but these require complex manipulation steps that are challenging to achieve in a POC or developing world environment.

In fact, the ideal POC diagnostic devices for developing world would use a small volume (few μl) of unprocessed sample taken directly from a patient. The device would first perform pretreatment (e.g. separating blood cells from plasma) before analyzing the sample. The sensitivity would have to be <pM level. The device would

preferrably be able to do multiplexing and it would also show the result in a simple way understable by a non-specialist. Moreover, it would have to resist high himidity (up to 100%) and temperatures (up to 40 °C) common in tropical countries and be self-powered or powered by a battery [40].

Until now, most of the POC devices in development relie on the manipulation of small amounts of fluid in channels where pumps and valves are required. Microfluidics has promised to achieve such functions, but it remains constrained due to difficulties associated with chip interconnection and cost.

More recently, influenced by the goal of achieving a low cost diagnostics for the developing world, paper diagnostics have been brought back in the forefront of research [91, 76, 74]. New techniques have been developed since the initial strips for pregnancy, such as the printed 3D channels [75]. However, the limit of detection still remains similar to the lateral flow immunoassays and the cost is, at the end, not so cheap due to the need of a external reader to have accurate results.

Other promising techniques which do not involve pumping have relied upon manipulations of the assay components on magnetic particles, for example [15].

1.3 Surface acoustic wave microfluidics

Surface acoustic waves (SAWs) are mechanical waves propagating on the surface of a substrate and are most commonly excited using interdigitated transducers (IDT) on top of a piezo-electric substrate. They have already been widely used in electronics as filters for signal processing [125], for example, in mobile phones. Long before the application of SAWs to electronics, extensive knowledge was accumulated by seismologists and researchers interested in non-destructive testing. Interestingly, the first mention of the interaction of the SAWs with a fluid was made by Shiokawa in 1989 [122]. This work had been ignored for a decade until the recent increase of interest in microfluidics, especially for biomedical applications. It has previously been shown that SAWs can be used to enable basic microfluidic actuation, such as droplet mixing [148, 126, 121, 37], heating [60, 61], movement [148, 134], atomization [63, 22, 59, 104], jetting [135, 13] as well as particle collection [134] and concentration [121, 68, 165, 113, 105, 147].

A small number of applications have emerged using SAW methods, including a planar device for polymerase chain reaction (PCR) [47], an atomizer for the production of nanoparticles [3], drug delivery[103], a method to sort cells [33, 34] and the development of an efficient interface with mass spectrometry [48, 50]. In these cases, each

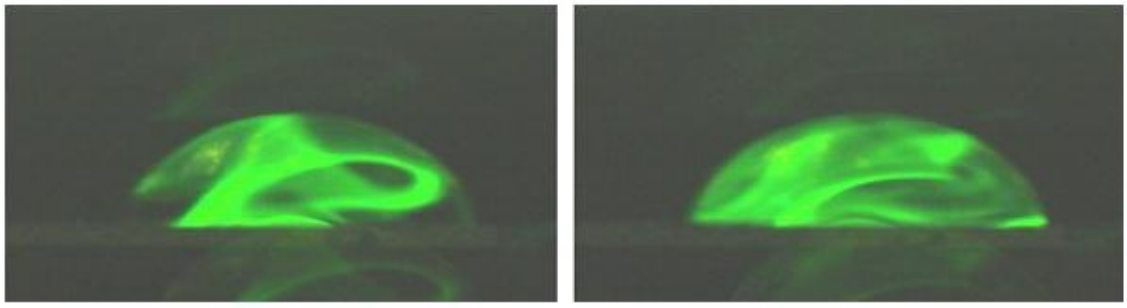

Figure 1.3: SAW induced internal streaming in a small water droplet (side view, approx. 50 nL). A dried fluorescent dye on the surface of the chip is dissolved by SAW agitation, and rapidly fills the whole droplet volume. (Wixforth, 2006)

fluidic function requires a specific IDT, limiting their further integration.

There follows a review of the original development of SAW microfluidic function and their most relevant applications on planar surface.

Mixing

Mixing small amounts of fluids is usually a delicate task. The surface to volume ratio is small in microfluidic systems which induces a low Reynolds number(< 1) [102]. At low Reynolds number, the viscosity dominates over inertia, which significantly influences the hydrodynamic behavior of a liquid. As turbulent streaming only occurs at high Reynolds numbers (> 2000), its absence in turn leads to reduced rates of mixing in microfluidic systems.

The interaction between SAWs and a fluid confined to a microfluidic device induces pronounced streaming effects which in turn acts as an internal stirrer to the fluid under consideration [148, 126, 121, 37].

Based on this approach, a microarray hybridization chamber for genetic and proteomic assays has successfully been brought into market (SlideBooster by Advalytix AG, Brunnthal, Germany). The advantage of using acoustic agitation during the hybridization of a microarray assay reduces the hybridization time significantly and improves the homogeneity of the fluorescent labelled spots on the microarray. Similarly, SAW streaming has been used in order to increase the capture of antigen in a biosensor based on surface plasmon resonance (SPR) [110].

Movement

The acoustic streaming effect can also induce a strong deformation of the droplet leading to a movement of the whole droplet into the direction away from the SAW

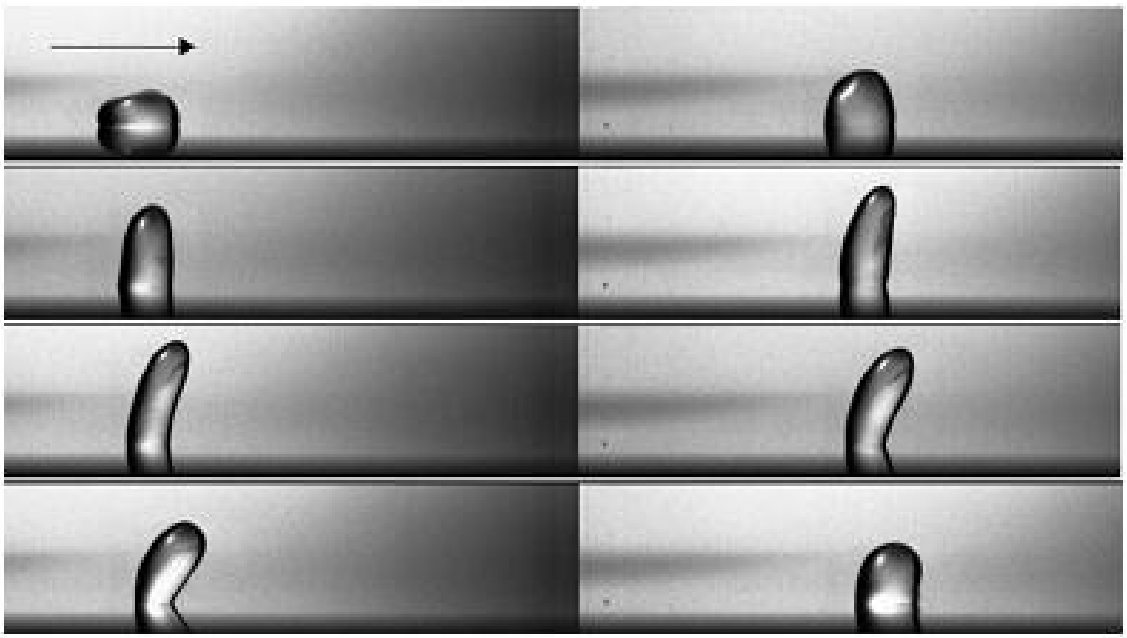

Figure 1.4: Successive snapshots of a water drop displaced by SAW, showing a periodic creeping and jumping flow. The arrow shows the direction of the displacement. (Brunet et al., 2010)

[148, 134]. This phenomenon originally observed by Shiokawa in 1989 [122] was only used several years later, although the physical principle remains poorly understood. The movement of the fluid is mainly due to the deformation of the droplet and the fluid streaming [118, 10, 16]. The surface chemistry also plays a major role as it defines the contact angle of the droplet [47]. Droplet actuation at high or low contact angle is very different and still not well understood.

By modifying the surface chemistry to defined hydrophobic and hydrophilic regions on the chip surface, it has been possible to guide a microdroplet in a track. This technique has been further developed to create a PCR on a planar surface. The SAW was used here to move the droplet on the different heating zone [47]. The actuation of droplet with SAW has also been used to collect particles from a surface [134].

Jetting

When the displacement of the surface due to the SAW is in the order of nanometers and when the droplet is sitting on a hydrophobic surface, the jetting phenomenon occurs as shown in Figure 1.5 [134]. This phenomenon was initially studied by using two elliptical focusing electrodes at two opposite ends of the substrate to create a standing wave. The transmission of radiation into the liquid causes the fluid to deform into an elongated liquid column which breaks into several droplets. Such jetting phenomenon demonstrates the ability for the SAW to drive strong inertial forcing on a liquid that

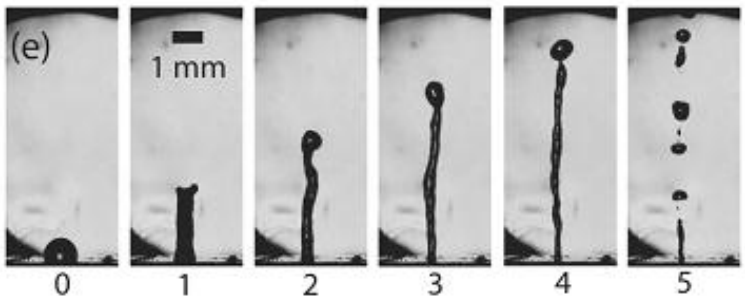

Figure 1.5: Jetting of a sessile drop using a standing surface acoustic wave. (Tan et al., 2009)

is unique in microfluidic flows. The jets observed present opportunities for the development of new methods in ink-jet or soft biological printing.

Atomization

When an acoustic wave propagates within a droplet, capillary waves appear at the air-liquid interface. Under sufficient power, liquid atomization is induced. This phenomenon is similar to the one used in modern ultrasonic nebulizers.

The SAW atomizer was first described by Shiokawa in 1989 [122] and further developed by Kurosawa in 1995 [63]. As for the movement of droplet, this technique has attracted only little interest until very recently [22, 59, 104]. Several studies have been made on the atomizer to determine the size of the droplets ejected which range from tens of nanometers to tens of micrometers. The sizes of the droplets are mainly determined by the proprieties of the fluid [3, 104].

The applications of SAW-actuated atomization include protein chip fabrication, rapid generation of protein aerosols [3], formation of periodic polymer patterns on a substrate [4], a method for drug delivery [103] and as an interface for mass spectrometry [48, 50].

Particle concentration

Particle concentration within a droplet has been first observed by by Li (Figure 1.6) [68]. By asymmetrically actuating the droplet with the SAW (Figure 1a), a circular streaming motion was generated within the droplet [121, 68, 165, 113, 105, 147]. This circular motion induces a secondary flow, traveling inward along the bottom surface and bringing the particles to the centre of the droplet. The drag force is however not strong enough to lift up the particles. The effect obtained here is counter intuitively different from centrifugation expected in a rotational motion and has been erroneously

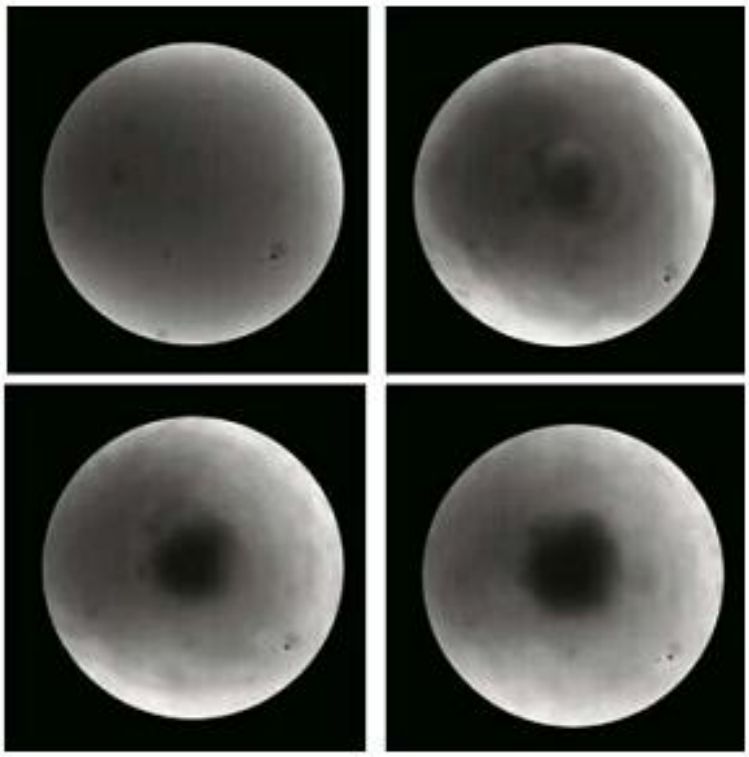

Figure 1.6: Concentration of microparticles within a droplet sitting on a surface using SAW. (Li et al., 2009)

named like this [164].

Several different types of particle have been concentrated including beads, pollens, cells and red blood cells [121, 68, 165, 105, 147]. But the separation of particles of different size has been possible only later by using the force arising from the acoustic pressure generated by the acoustic wave propagation in the fluid to differentially move larger particle away from the center [113].

1.4 Phononics

The term phononics is used to define the field of engineering artificial acoustic materials with tailored dispersion properties. A phononic crystal is a material that possesses a periodic ordering of regions with a contrast in the constituent. Such ordered arrays, which are often simple cubic or hexagonal close packed 3-D structures, or square, hexagonal or honeycomb 2-D structures, scatter the sound waves either as a function of its direction and-or its frequency.

An example of a real but fortuitous phononic crystal is the sculpture by Eusebio Sempere (1923-1985) [77]. This sculpture is a two-dimensional periodical arrangement of steel tubes sitting in a park in Madrid (Figure 1.7). In 1995, the acoustic filtering

Figure 1.7: Sculpture by Eusebio Sempere in Madrid discovered to be a phononic structure. (Martinez-Sala et al., 1995)

was determined experimentally by placing microphones around the sculpture and the measurements showed that attenuation occur at particular frequencies in the kilohertz range.

Phononic crystals have already shown the ability to create complete bang gaps [123, 64, 136, 138, 58, 20] as well as positive and negative refraction [167, 129] as described below. Research has been made both on pressure and elastic wave.

1.4.1 Band gap

The first phononic band gap was determined by Sigalas and Economou (1993) [123] followed by Kushwaha in 1995 [64]. The existence of full band gaps has led to a range of applications such as filters [99], acoustic waveguides [67, 149] and strong resonators [156].

The concept of band gaps can be explained by considering the interference of multiple waves scattered within a phononic crystal. When a set of scattering elements is positioned periodically, waves are dispersed from one element to the other, and end up

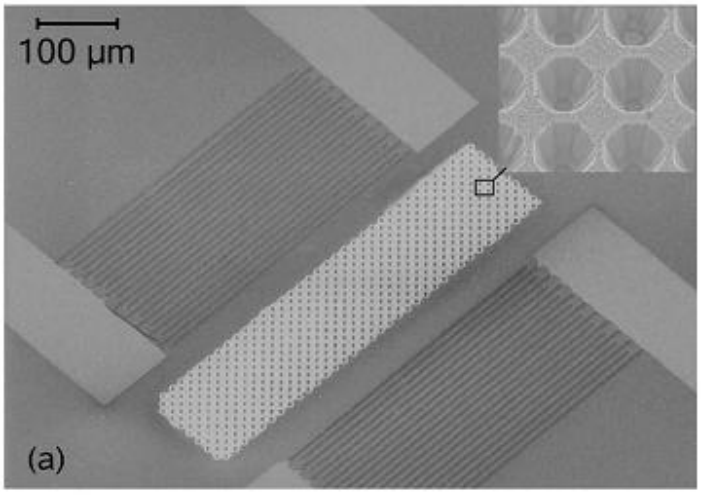

Figure 1.8: Scanning electron microscope image of a phononic crystal for surface acoustic waves. The structure, consisting of 9 μm diameter air holes with a 10 μm pitch, is surrounded by a pair of IDTs to ensure surface wave transduction. The inset in the top-right corner shows a more detailed view of the holes etched in the lithium niobate single crystal substrate. (Benchabane et al., 2006)

filling all available space and propagating in every direction. The waves interfere constructively or destructively depending upon the frequency and on the phononic crystal geometry. A band gap appears when the scattered waves interfere destructively in a given direction.

For surface acoustic waves, a complete band gap is found experimentally in a two-dimensional square-lattice piezoelectric phononic crystal etched in lithium niobate [8]. Similar experiments have been conducted in a silicon plate and showed the complete bandgap for Lamb waves, which are waves propagating in a thin plate [166].

Several lattices have been investigated. The most common is the square lattice, although full band gap are difficult to achieve especially in solid material. The triangular and hexagonal lattices allow the creation of larger bandgaps [153, 80]. However, in order to induce a wide frequency band gap, the hexagonal lattice requires the film thickness to be approximately the same of the lattice constant.

Because etching holes in a substrate is a straightforward fabrication method, it has been widely use to investigate the band gap of a phononic crystal. However, it has been shown that using two solid materials with strong contrast in the elastic modulus, it is possible to obtain larger bandgaps [90].

The ability to create band gaps also gave the possibility to confine the energy and create waveguides (Figure 1.9). Waveguides are important in the communication field to avoid the loss of energy due to the diffraction of the waves. Waveguides have been

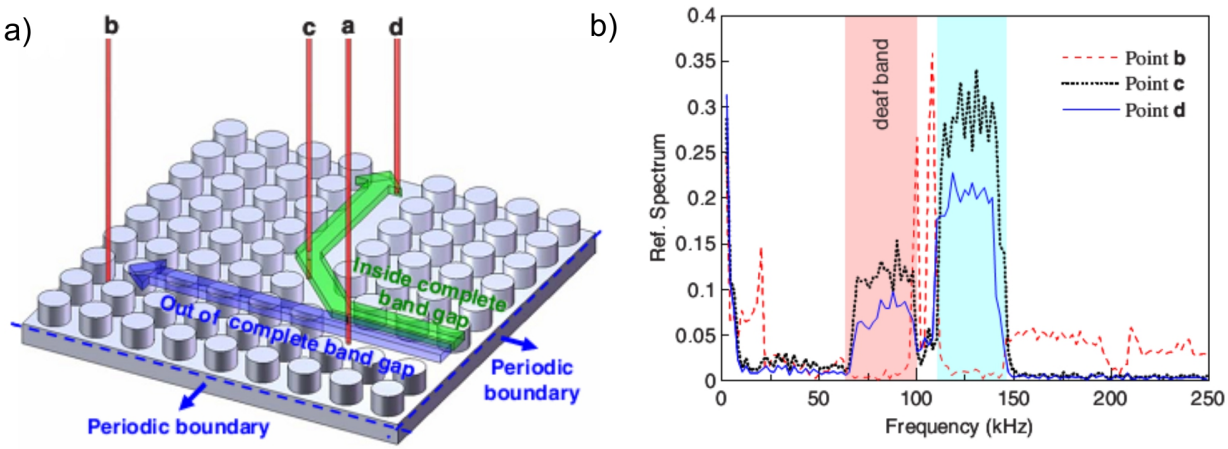

Figure 1.9: (a) Paths of the waves with frequency, respectively, outside and inside the complete band gap propagating in the structure with a bent waveguide. (b) Comparison among the spectra measured at points b, c, and d. (Wu et al., 2009)

demonstrated for SAW by creating an array of pillars and show a confinement of the energy [67, 149].

1.4.2 Refractive devices

In acoustics, a standard lens similar to an optical lens is not possible because (1) the sound velocity is larger in solids than in air and (2) solid materials are not transparent to sounds.

It has been shown that a sonic crystal made of periodic distributions of rigid cylinders in air can act as a new material which allows the construction of refractive acoustic devices for airborne sound (Figure 1.10). It was demonstrated that the crystal has low impedance and that the sound is transmitted at subsonic velocities [167, 18]. Interestingly, the refractive devices based on sonic crystals behave in a manner similar to that of optical systems.

Furthermore, with by taking advantage of the negative refraction, it has been possible to design a 3D flat focusing lens for audible sound (Figure 1.11) [161]. Negative refraction occurs at interfaces between materials where one has an ordinary positive phase velocity (i.e. a positive refractive index), and the other has the more exotic negative phase velocity (a negative refractive index). Negative refractive index exists in the band structure of a phononic crystal [57].

For mechanical waves, however, only simulations have shown so far focusing behavior using a phononic lens [72, 151].

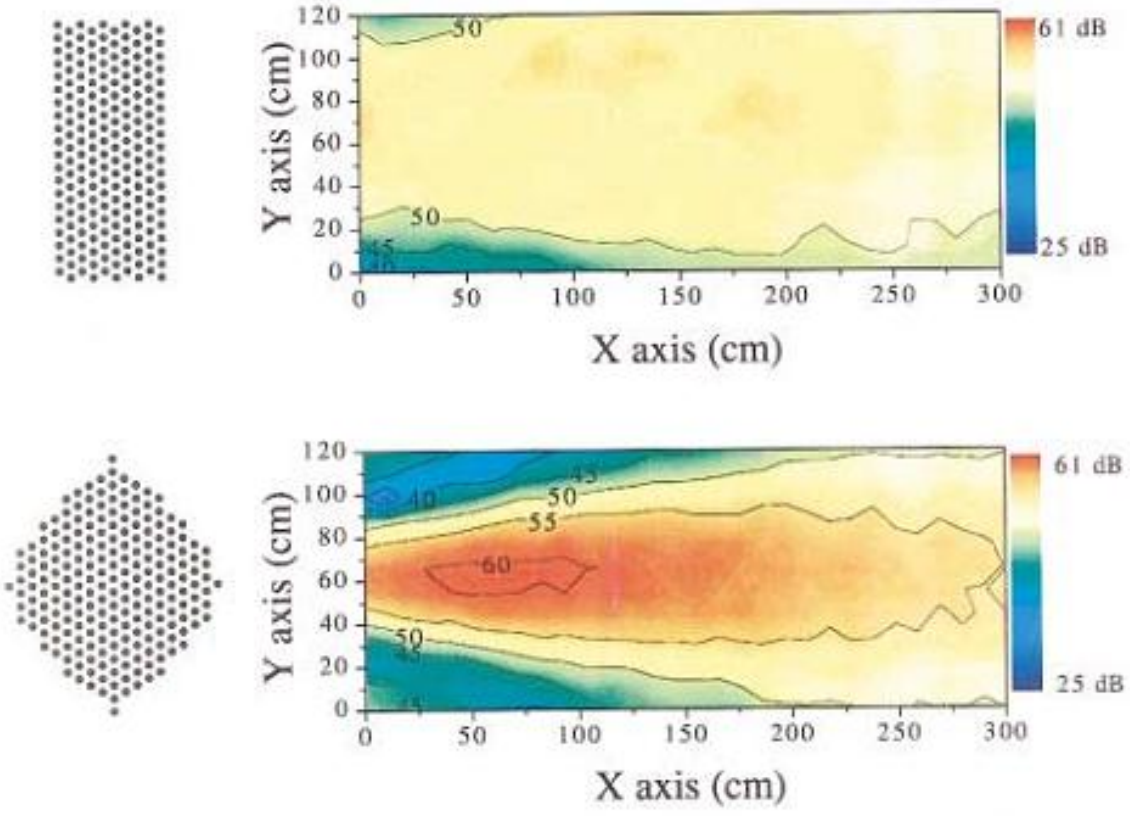

Figure 1.10: Sound level maps taken at 1700 Hz along with the samples' sketches. The sketches are drawn to scale: both samples are 1.2 m wide. (Cervera et al., 2001)

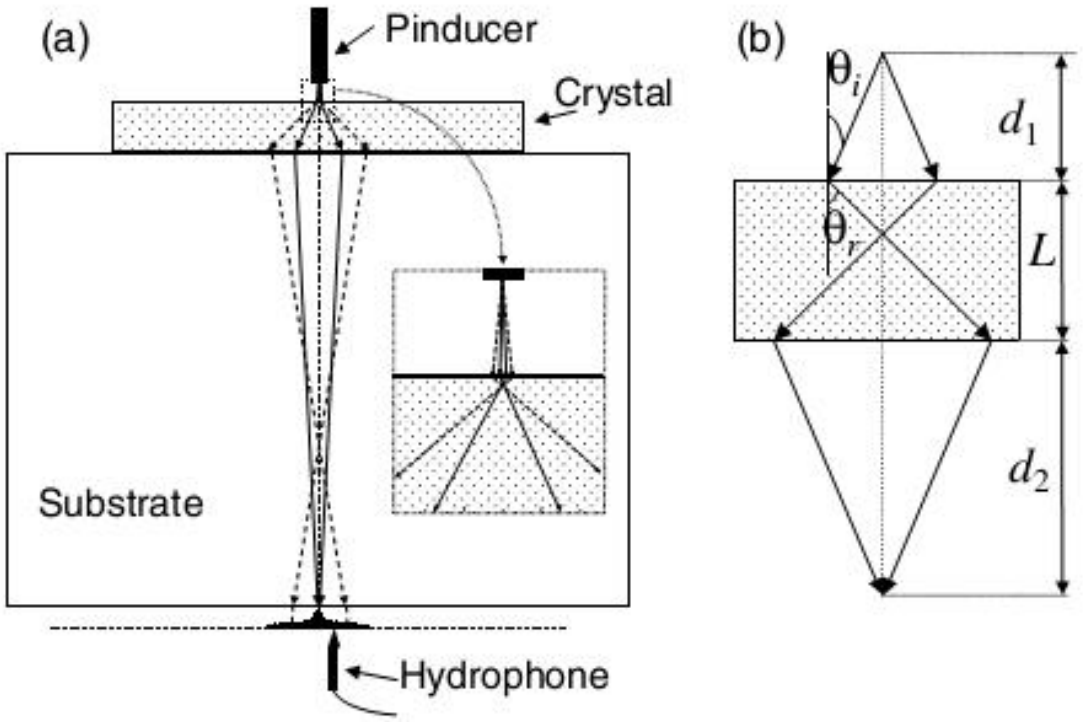

Figure 1.11: (a) Experimental setup, with rays indicating the predicted directions of the group velocity at 1.6 MHz for angles of incidence of 1.5° and 5°. (b) Diagram showing the focusing condition in a medium with negative refraction. (Yang et al., 2004)

1.5 Motivation and Objectives

Motivation

Infectious diseases continue to kill millions of people each year and are a significant burden on the socio economic development of developing countries. After many years of international policy aimed at containing the diseases, it has recently become an explicit aim to move towards elimination of infectious diseases. However, if this is to occur, it will be important to have highly efficacious diagnostic tools to ensure infected individuals are found. Unfortunately, the diagnosis of infectious diseases in the developed and developing world requires the full integration of complex assays in easy-to-use platforms with robust analytical performances at minimal cost. Many current bioanalytical technologies have been developed for use in laboratories and clinics, including the current gold standard for the diagnosis of tuberculosis and malaria.

The miniaturization and integration of complex functions into LOC technologies have already had some success in translating diagnosis assays out of a centralized laboratory to POC settings. In the field of infectious diseases, where detection of markers at the pM level is required, lateral-flow immunochromatographic strips have also found

applications, although, this technology has shown some limitations in sensitivity and in the integration of complex diagnostics procedures. Other microfluidic technologies have been developed but still remain constrained due to chip interconnection and are either not likely to go out of research laboratories or not appropriate for low resource settings.

Objectives

The goal of the PhD was to develop a new microfluidic platform that reduced the dependency of the diagnostic procedure on large laboratory instruments and provide simplicity of use, enabling the patient sample to be processed and diagnosed on a low cost, disposable biochip. To do so, SAW devices, which are commonly used in mobile phone technologies, were adapted to provide controlled microfluidic function.

First, the idea of shaping the SAW was initiated by using particular designs of electrodes. This system allowed a spatial control of the waves required to create complex microfluidc functions. Then, the unique properties of phononic crystals were use to add another level of control on the shape of the wave and more importantly on the intensity. The power of these techniques was demonstrated by controling the amplitude and direction of water jet towers and by propulsing a macrometer scale object in water. As a proof of concept of a diagnostic device for the developing world using shaped SAW, an immunoassay using only mobile phone technologies (SAW, LED and CMOS camera) and a method to enrich malaria infected cells in a microdroplet were demonstrated.

Chapter 2

Theory

In this chapter, the basic theory of surface acoustic waves is explored with an emphasis on the Rayleigh and Lamb types of waves. The standard way to generate surface acoustic waves is then described, before describing at the theory of surface acoustic wave streaming. Finally, a desciption of the wave propagation in phononic crystals is made as well as its numerical modelling.

2.1 Surface acoustic waves

Waves propagating in a medium can be divided in two main categories: body waves and surface waves. Surface acoustic waves are mechanical waves propagating along the surface of a medium. Most of the SAWs consist of a combination of a compressional (or longitudinal) wave, a z-polarized shear (or transversal) waves and a y-polarized shear (or transversal) wave represented in Figure 2.1 [25, 36]. Moreover, in the case of a piezoelectric solid, there is also an accompanying electrostatic wave.

For example, Rayleigh waves combine a longitudinal and a z-polarized shear motion, while shear-horizontal surface acoustic wave (SH-SAW) combine a longitudinal and a y-polarized shear motion. Lamb waves are another type of surface acoustic wave and

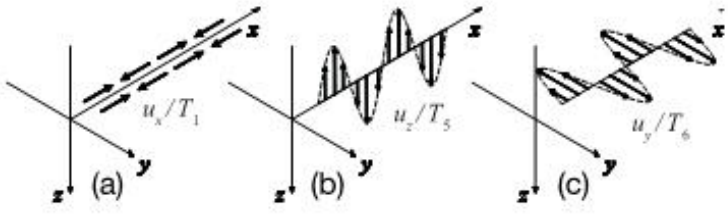

Figure 2.1: Representation of (a) compressional, (b) z-polarized shear, (c) y-polarized shear motion. (Friend et al., 2010

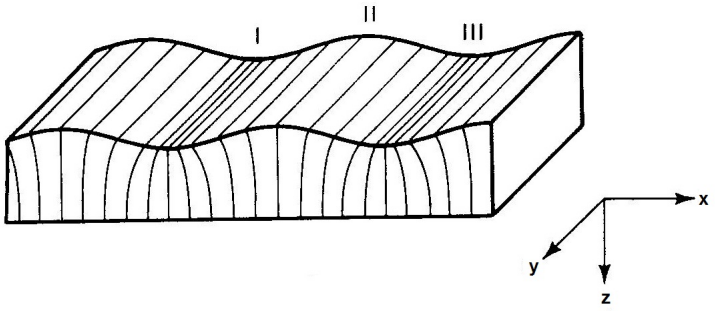

Figure 2.2: Rayleigh wave in a semi-infite solid. (I) and (III) are compression and (II) is dilatation regions. (Data, 1986)

may have several modes as discussed later.

From the literature, surface acoustic waves and Rayleigh wave are often confused and Lamb wave are sometimes not considered as SAW. In this thesis, the term surface acoustic wave will be used to call any type of mechanical wave propagating along a surface (Rayleigh, Lamb, ...).

In the next section, a more precise definition of the Rayleigh wave and Lamb wave will be given.

2.1.1 Rayleigh waves

The Rayleigh wave is a type of surface acoustic wave propagating on the surface of a semi-infinite solid. It decays away exponentially from the surface so that most of the energy is confined at the surface. The particle moves both in the direction of wave propagation (x) and perpendicular to the depth (z) shown in Figure 2.2. There is no variation in the transverse direction along the surface (y). Thus, it is a combination of a longitudinal and a z-polarized shear motion [25].

At the surface of a material, there is no restraining force perpendicular to the surface so that compressing a material in z direction automatically produces motion in the x direction. In a Rayleigh wave, there are alternate regions of compression and dilatation. The compression bends the surface down while dilatation cause it to bulge up.

Lord Rayleigh predicted this type of wave in 1885 [108] and found the following characteristic equation:

$$\eta^6 - 8\eta^4 + 8(3 - 2\xi^2)\eta^2 - 16(1 - \xi^2) = 0 \tag{2.1}$$

given that η and ξ are the ratio between velocities of longitudinal (l), shear (s) and

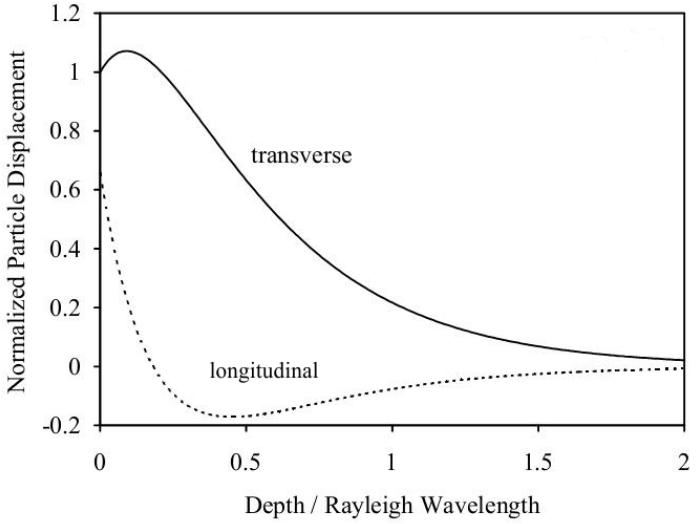

Figure 2.3: Variation of particle displacement as a function of the depth for a Rayleigh wave showing a rapid decay within a wavelength. The nature of this plot depend on the substrate material and the orentation. The particle displacement is normalized to the maximum displacement at the surface. (Data, 1986)

Rayleigh (R) waves:

$$\xi = \frac{c_s}{c_l} \tag{2.2}$$

$$\eta = \frac{c_R}{c_s} \tag{2.3}$$

Since $\xi^2 = \frac{1-2\nu}{2(1-\nu)}$, where ν is the Poisson Ratio, Viktorov found that the solution can be approximated by [139]:

$$\eta = \frac{0.87 + 1.12\nu}{1 + \nu} \tag{2.4}$$

Rayleigh wave velocities in a homogeneous half space are independent of the wavelength and thus are non-dispersive. In the field of seismology, shear wave velocities generally increase with depth in the Earth due to non-homogenous space. Since long-wavelength Rayleigh waves have motions at a significantly greater depth than do short wavelength Rayleigh waves, the velocities of Rayleigh waves generally increases with wavelength, for the Earth.

Figure 2.3 shows the variation of the particle displacement in y and z direction with the depth. The displacement decays for both components with the depth. However, the sign reverses for the z component as shown in Figure 2.3. This effect is similar to what one would obtain by bending a simple rod, for example. In one side of the rod there

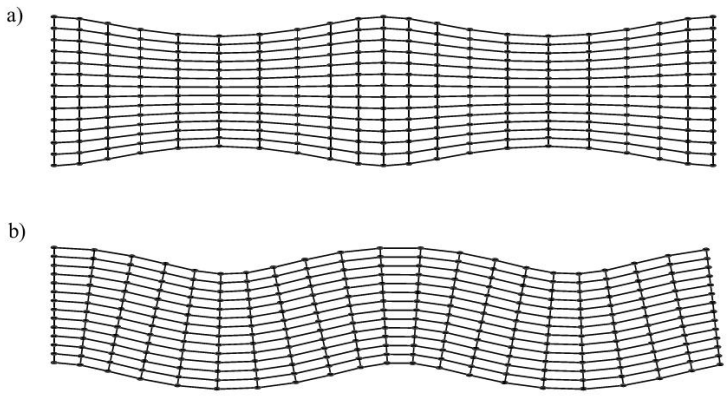

Figure 2.4: (a) Symmetric and (b) antisymmetric waves. (Kuttruff, 1991)

would be dilation and on the other side compression, between the two there would be an unstrained region. The sign would therefore change when crossing the unstrained region. The particle displacement decays rapidly within a wavelength. SAW devices are usually made on substrates whose thickness is at least five wavelengths to avoid interference from the back surface. Due to the compressional and shear motion, the particle motion is an ellipse in the x-z plane with the top of the ellipse moving in the opposite direction of the wave propagation.

2.1.2 Lamb waves

Lamb waves are elastic waves propagating in a solid plate with free boundaries, for which displacements occur both in the direction of wave propagation and perpendicularly to the plane of the plate. They are named after the English mathematician Horace Lamb who published an analysis and description of acoustic waves of this type in 1917 [65].

Plates support two infinite sets of Lamb wave modes, whose velocities depend on the relationship between wavelength and plate thickness. Examples of the deformations are shown in Figure 2.4. It can be either a symmetric (S_0, S_1,...) or an antisymmetric (A_0, A_1, ...) wave.

The two characteristic equations are given by:

$$\frac{\tan \beta d}{\tan \alpha d} = -\frac{4\alpha\beta k^2}{(k^2 - \beta^2)^2} \tag{2.5}$$

for the symmetric modes and:

$$\frac{\tan \beta d}{\tan \alpha d} = -\frac{(k^2 - \beta^2)^2}{4\alpha\beta k^2} \tag{2.6}$$

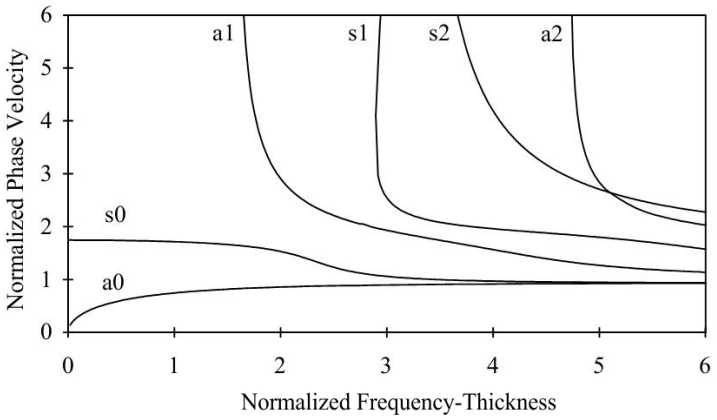

Figure 2.5: Dispersion curve of Lamb waves. The phase velocity in normalized to the shear wave velocity (c/c_s) and the product of the frequency and thickness normalized to the shear wave velocity ($\omega d/c_s$).

for the antisymmetric modes, considering

$$\alpha^2 = \frac{\omega}{c_l^2} - k^2 \tag{2.7}$$

and

$$\beta^2 = \frac{\omega}{c_s^2} - k^2 \tag{2.8}$$

where ω is the angular frequency and k the wavenumber.

These characteristic equations give the phase velocity as a function of frequency and thickness for the symmetric and asymmetric Lamb modes, respectively.

The Lamb waves are dispersive, which means that the phase velocity of the wave changes with the frequency. A typical dispersion curve for Lamb waves is represented in Figure 2.5. At high frequencies or large thickness, the velocities of both zero-order modes approach the Rayleigh velocity.

2.2 SAW devices

In SAW technology, the purpose is to generate and control suface waves. SAWs are commonly created using interdigitated electrodes implemented on top of a piezoelectric material.(Figure 2.6)

The piezoelectric effect characterizes the ability of certain solid material to produce an electric charge when it is subject to a mechanical pressure, and vice versa. The piezoelectric materials may be the bulk of the substrate, such as lithium niobate

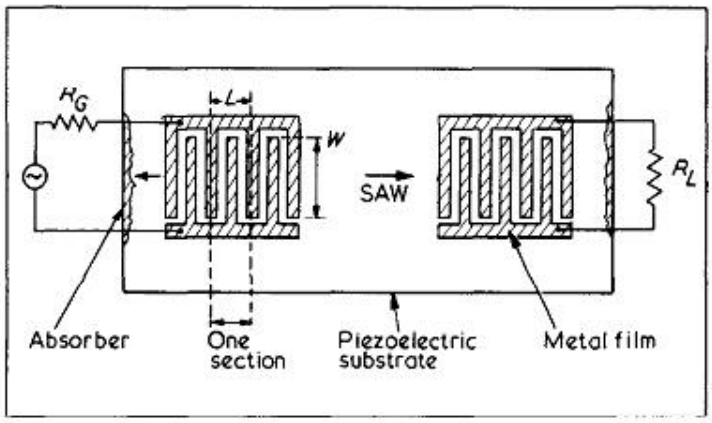

Figure 2.6: Sketch of a typical SAW device made of a interdigitated transducer on a piezoelectric substrate.(Morgan, 1973)

Table 2.1: Wave velocity (c) and coupling constant (K^2) for Lithium niobate and Lithium tantalate.

Material	Cut	Direction	$c(ms^{-1})$	$K^2(\%)$
Lithium niobate	Y 128°-rotated	Z	3488	4.6
		X	3996	5.6
Lithium tantalate	77.5°-rotated Y	90° to X	3379	1.6

($LiNbO_3$) and lithium tantalate ($LiTaO_3$), or a thin film material, such as zinc oxide (ZnO) or aluminium nitride (AlN), on the surface of a substrate. The choice of the piezoelectric material and cut is critical and is influenced by two principal aspects. The first consideration is the beam steering. In an anisotropic solid, the surface wave velocity depends on the direction of propagation [25]. In an anisotropic media, the flow of power is not necessarily perpendicular to the phase front. The wave will tend to be steered towards low velocities directions.

The second restriction arises from the need of a strong piezoelectric coupling K^2, which is an indicator of the effectiveness with which a piezoelectric material converts electrical energy into mechanical energy, or converts mechanical energy into electrical energy. The effective coupling constant K^2 depends on the cut and orientation as shown in Table 2.1. For example, for a y-cut $LiNbO_3$ the x direction has the highest K^2 and is preferred for SAW devices in microfluidics.

In the case of a standard interdigitated transducer shown in Figure 2.6 and invented by White and Voltmer in 1965 [142], the resonant frequency, f, is dependent upon the periodicity L, and the sound velocity on the piezoelectric wafer, c [81]. Consequently, for a given input frequency, the SAW output is only generated when the periodicity of the IDT satisfies the ability of the electrodes to support the resonance, thus:

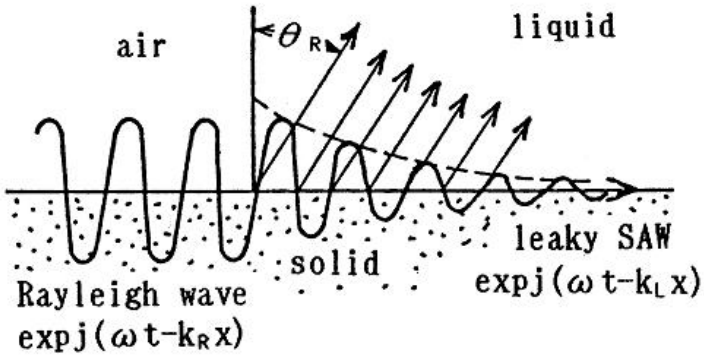

Figure 2.7: Schematic depiction of the interaction between a SAW and a droplet on the surface of a SAW substrate. The acoustic energy is refracted into the uid under an angle θ_R, creating streaming within the droplet. (Shiokawa, 1989)

$$L = \lambda = \frac{c}{f} \tag{2.9}$$

Where λ is the wavelength of the surface acoustic wave. The apperture of the SAW is defined by the width (W) of the fingers as shown in Figure 2.6.

Several different designs of electrodes have been developed in the field of electronic communication and signal processing [82], but only a small number have been used for microfluidics. While the electrode mentioned above is the most widely used, the single phase unidirectional transducer (SPUDT) was used to increase the efficiency, the circular IDT has brought interest for the ability to focus waves in order to increase the energy [154, 121]. In this thesis, the slanted finger IDT is introduced to create tuneable surface acoustic waves to control precisly the position of the SAW beam.

Another widely used technique to generate SAW is by thermal dilatation of a material using pulsed laser. In this case, a wide range of high frequency SAWs (1-500 MHz) are generated. This technique has found application on the determination of Young's modulus of thin films [158, 157] and also in the determination of phononic band gaps [166].

2.3 SAW streaming

When the SAW refracts into a fluid, the energy is rapidly dissipated into the fluid inducing streaming. The acoustic waves are partially dissipated, resulting in a decrease in the mean momentum flux as the waves travel through the fluid. A net force is associated with this decrease in the momentum flux. The equations governing acoustic streaming have already been described by Eckart, Nyborg, Lighthill, as well as others

[28, 88, 70]. In our particular case, the acoustic Reynolds number ($Re_A = \frac{\rho_F \nu_l \lambda_F}{2\pi\mu}$) range from 0.02 to 2, the particle velocity ν_l from 0.01 to 1 m/s and fluid velocity from 0.1 to 10 mm/s. Re_A being smaller than 1 in most of the cases described in this thesis and the particle velocity being much higher than the fluid velocity, here the assumption is made that the streaming is slow and use Nyborgs equations to describe the force arising from the SAW streaming. The streaming force can be written as [122]:

$$F =< \rho_0 \nu \cdot \nabla \nu + \nu \nabla \cdot \rho_0 \nu > \tag{2.10}$$

Where ρ_0 is the constant equilibrium density, ν is the oscillatory particle velocity and the brackets denote the time average.

SAW becomes a leaky SAW when in contact with a fluid as shown in Figure 2.7. Under these conditions the SAW is refracted into the liquid with an attenuation length of the surface wave given by:

$$l_{SAW} = \frac{\rho_{SAW} c_{SAW} \lambda_{SAW}}{\rho_F c_F} \tag{2.11}$$

Where ρ_{SAW} and ρ_F are the substrate and fluid densities, c_{SAW} and c_F are the wave velocities and λ_{SAW} is the wavelength of the SAW. The waves are refracted into the liquid as a longitudinal wave at the Rayleigh angle given by [9]:

$$\theta_{Rayleigh} = \sin^{-1} \frac{c_F}{c_{SAW}} \tag{2.12}$$

In the case of lithium niobate and water, the angle is around 23°.

To calculate the force arising from the SAW streaming, one has to take into account the fact that the propagation constant (or wavenumber) k_R for SAW is a real number, while for leaky SAW, k_L is a complex number. Thus, the particle displacement (u_x, u_z) in the liquid can be expressed in the following form:

$$u_x = A e^{j\omega t} e^{-jtk_L x} e^{-\alpha k_L z} \tag{2.13}$$

$$u_z = -j\alpha A e^{j\omega t} e^{-jtk_L x} e^{-\alpha k_L z} \tag{2.14}$$

where

$$\alpha = 1 - (\frac{c_L}{c_W})^2 \tag{2.15}$$

A is the amplitude of the wave, $\omega = 2\pi f$ is the angular frequency; c_L and c_w are

the leaky and longitudinal wave velocity, respectively.

By deriving from the particle displacement of Equation 2.13 and 2.14 with the particle velocity $\nu = \delta u/\delta t$ and substituting into Equation 2.10, the force F_x and F_z can be obtained. Since the force arising from the SAW streaming is given by $F_{SAW} = \sqrt{F_x^2 + F_z^2}$, it can be expressed as:

$$F_{SAW} = -\rho_0(1 + \alpha_l^2)^{3/2} A^2 \omega^2 k_i e^{2(k_i x + \alpha_l k_i z)} \tag{2.16}$$

Where $\alpha = j\alpha_l, k_L = k_r + jk_i$

This force is directed at the Rayleigh angle [122] and the amplitude change of the decaying longitudinal wave propagating in the fluid can be expressed as:

$$A = A_0 e^{-\beta d} \tag{2.17}$$

where A_0 is the initial amplitude of the wave, d the distance and β is the coefficient of attenuation described by:

$$\beta = \frac{2\eta\omega^2}{3\rho_F c_F^3} \tag{2.18}$$

with η being the viscosity of the fluid.

2.4 Wave propagation in phononic crystals

In a linear-elastic medium, the equations of motion and constitutive equations can be expressed as [23, 152] :

$$\rho(\mathbf{x}) \cdot \ddot{u}_i(\mathbf{x}, t) = \partial_j \sigma_{ij}(\mathbf{x}, t) + \rho f_i \tag{2.19}$$

and

$$\sigma_{ij}(\mathbf{x}, t) = C_{ijmn}(\mathbf{x}) \partial_n u_m(\mathbf{x}, t) \tag{2.20}$$

where $\rho(\mathbf{x})$ is the position-dependent mass density, $u_m(\mathbf{x}, t)$ the displacement vector, $\sigma_{ij}(\mathbf{x}, t)$ the Cauchy stress tensor, f_i the body force, C_{ijmn} the position dependent elastic stiffness tensor and $(\mathbf{x}) = (x, y)$ is the position vector of the reference point.

If we assume that no body force exists, Equations 2.21 and 2.20 can be re-written as:

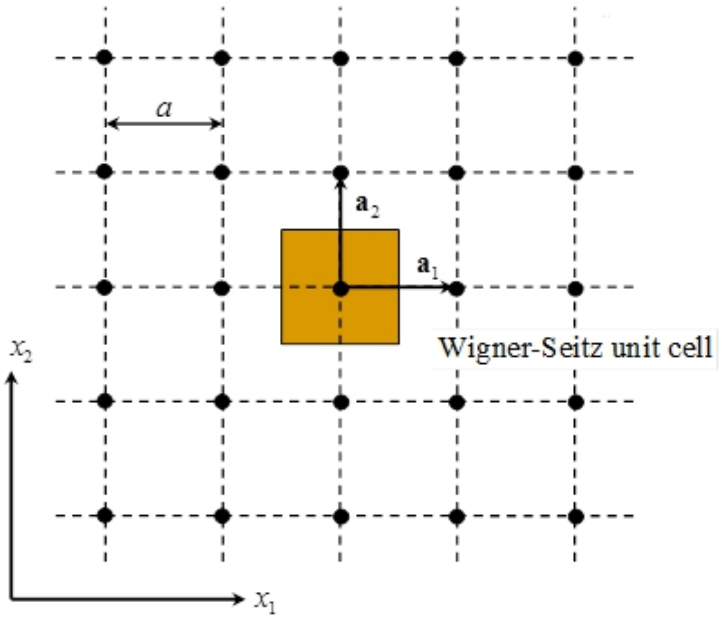

Figure 2.8: Schematic diagram of a primitive Wigner-Seitz unit cell in the Bravais lattice (lattice constant is a).

$$\rho(\mathbf{x}) \cdot \ddot{u}_i(\mathbf{x}, t) = \partial_j [C_{ijmn}(\mathbf{x}) \partial_n u_m(\mathbf{x}, t)] \tag{2.21}$$

The unique property of a crystal is that its atoms are arranged in a regular 3-dimensional array called a lattice. A common method to model and study such a periodic system is the Wigner-Seitz method. A Wigner-Seitz cell is a primitive cell spanning the entire Bravais lattice without overlapping or leaving gaps. A 2-D primitive unit cell of a square lattice chosen by the Wigner-Seitz method is shown in Figure 2.8. The 2-D Wigner-Seitz unit cell can be constructed by drawing lines connecting the point to all nearby lattice points, the smallest area bounded by these perpendicular bisectors is called the Wigner-Seitz unit cell.

The Wigner-Seitz cell in the reciprocal lattice is known as the first Brillouin zone. It is made by drawing planes normal to the lines joining nearest lattice points to a particular lattice point. Considering the primitive lattice vectors $\mathbf{a}_1$, $\mathbf{a}_2$ and $\mathbf{a}_3$, the associated primitive reciprocal lattice vectors $\mathbf{b}_1$, $\mathbf{b}_2$ and $\mathbf{b}_3$ is defined as:

$$\mathbf{b}_1 = 2\pi \frac{\mathbf{a}_2 \times \mathbf{a}_3}{\mathbf{a}_1 \cdot (\mathbf{a}_2 \times \mathbf{a}_3)}, \tag{2.22}$$

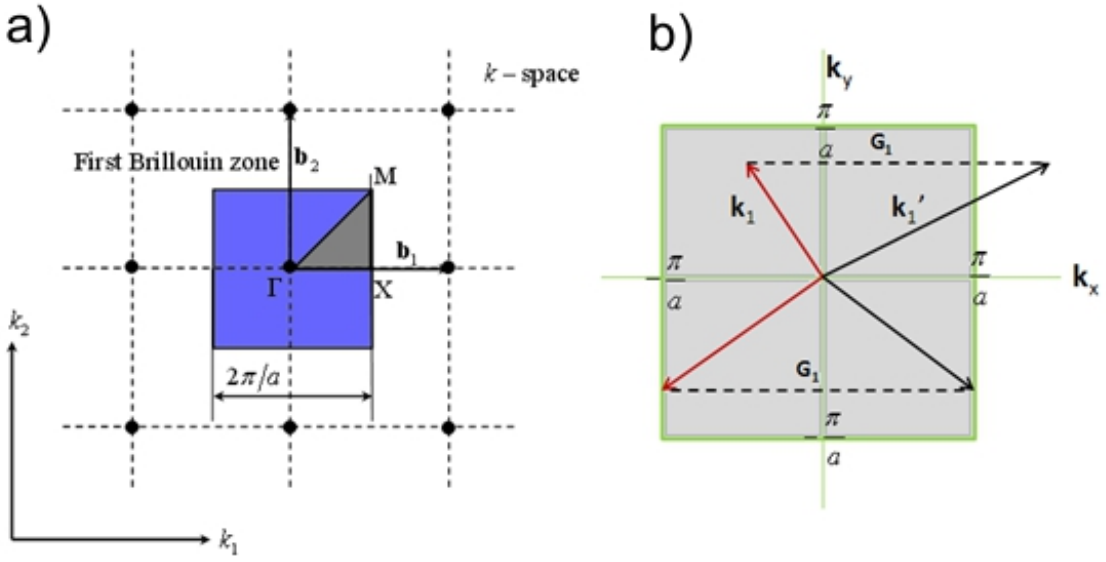

Figure 2.9: (a) Schematic representation of the relative reciprocal lattice corresponding to the primitive square lattice. (b) Diagram showing the wave vector $\mathbf{k}$ outside the first Brillouin zone has a corresponding point inside the first Brillouin zone.

$$\mathbf{b}_2 = 2\pi \frac{\mathbf{a}_3 \times \mathbf{a}_1}{\mathbf{a}_2 \cdot (\mathbf{a}_3 \times \mathbf{a}_1)}, \tag{2.23}$$

$$\mathbf{b}_3 = 2\pi \frac{\mathbf{a}_1 \times \mathbf{a}_2}{\mathbf{a}_3 \cdot (\mathbf{a}_1 \times \mathbf{a}_2)}. \tag{2.24}$$

For a simple cubic primitive cell in the Bravais lattice with a side a, we can rewritte the equations above as:

$$\mathbf{b}_1 = \frac{2\pi}{a}\mathbf{x}, \tag{2.25}$$

$$\mathbf{b}_2 = \frac{2\pi}{a}\mathbf{y}, \tag{2.26}$$

$$\mathbf{b}_3 = \frac{2\pi}{a}\mathbf{z}, \tag{2.27}$$

Figure 2.9 shows a schematic diagram of a relative reciprocal lattice corresponding to a primitive cell.

According to Bloch's theorem, the wave vector $\mathbf{k}$ which locates outside of the first Brillouin zone would have a corresponding point inside the first Brillouin zone as shown in Figure 2.9b [152]. When the wave vectors $\mathbf{k}$ of the square lattice are confined in the first Brillouin zone, the wave vectors k_x and k_y are restricted to $-\frac{\pi}{a} < k_x < \frac{\pi}{a}$ and

$-\frac{\pi}{a} < k_y < \frac{\pi}{a}$.

The irreducible part of the first Brillouin zone in a square lattice is shown in Figure 2.9a, with a triangle region formed by three points Γ, X, and M representing the direction of the wave propagation.

According to the periodicity of phononic crystals, one can use the Bloch's Theorem and express the displacement and stress components as:

$$u_i(\mathbf{x}, t) = e^{i\mathbf{k}\cdot\mathbf{x}} U_i(\mathbf{x}, t) \tag{2.28}$$

$$\sigma_{ij}(\mathbf{x}, t) = e^{i\mathbf{k}\cdot\mathbf{x}} T_{ij}(\mathbf{x}, t) \tag{2.29}$$

where $\mathbf{k} = (k_1, k_2, k_3)$ is the wave vector, $U_i(\mathbf{x}, t)$ $T_ij(\mathbf{x}, t)$ are the periodic functions which satisfying the relations defined as:

$$U_i(\mathbf{x} + \mathbf{a}, t) = U_i(\mathbf{x}, t), \tag{2.30}$$

$$T_ij(\mathbf{x} + \mathbf{a}, t) = T_ij(\mathbf{x}, t), \tag{2.31}$$

To calculate the dispersion of a 2-D phononic crystal, the eigenfrequencies and mechanical displacements can be obtained at a specific wave vector $\mathbf{k}$, and the eigenfrequencies of the given wavevector along the directions of irreducible Brillouin zone can be plotted to obtain the phononic band structure as represented in Figure 2.10

2.4.1 Simulation of a band structure

The analyses of surface waves in phononic crystals (PC) plates made using a finite-element (FE) method.

To calculate the eigenfrequencies and eigenmodes of Lamb waves in PC plates, an FE structural model is constructed (Comsol Multiphysics 3.5a, COMSOL Group) for the PC unit cell and then meshed. By assuming a time-harmonic solution, the wave equations lead to an eigenvalue problem in the FE formulism and yield the eigenfrequencies and eigenvectors (i.e., eigenmodes). The Bloch-Floquet theorem can be applied to treat the periodic boundary conditions (PBCs) for a unit cell of the PC plates to obtain the dispersion relations in the first Brillouin zone. In the calculations, a script (Matlab R2011a, The MathWorks, Inc.) was used to iteratively vary the

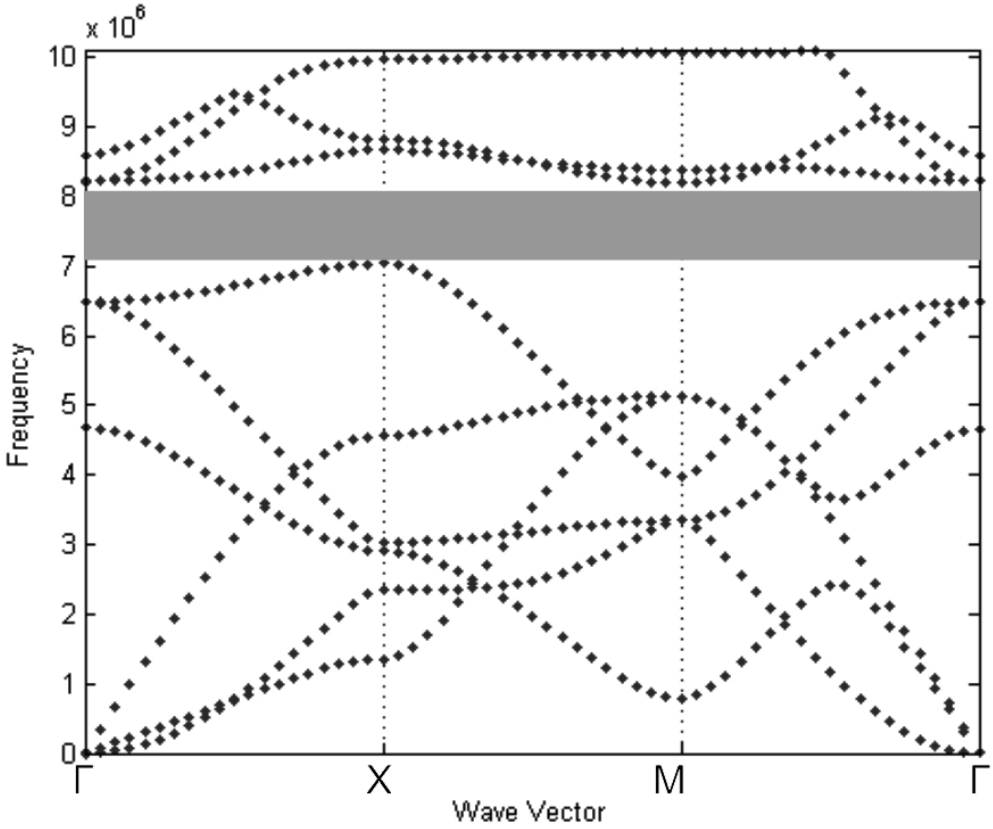

Figure 2.10: Typical band structure of a square lattice phononic crystal. The points are the eigenfrequencies of a given wavevector. The grey area represents a full band gap.

structural dimensions, geometry, and the k-dependent PBCs.

The frequency response analysis of the FE method can also be used to calculate the transmission and reflection in a PC plate structure. Meanwhile, we are able to model the wave propagation in the phononic plate.

Chapter 3

Materials and Methods

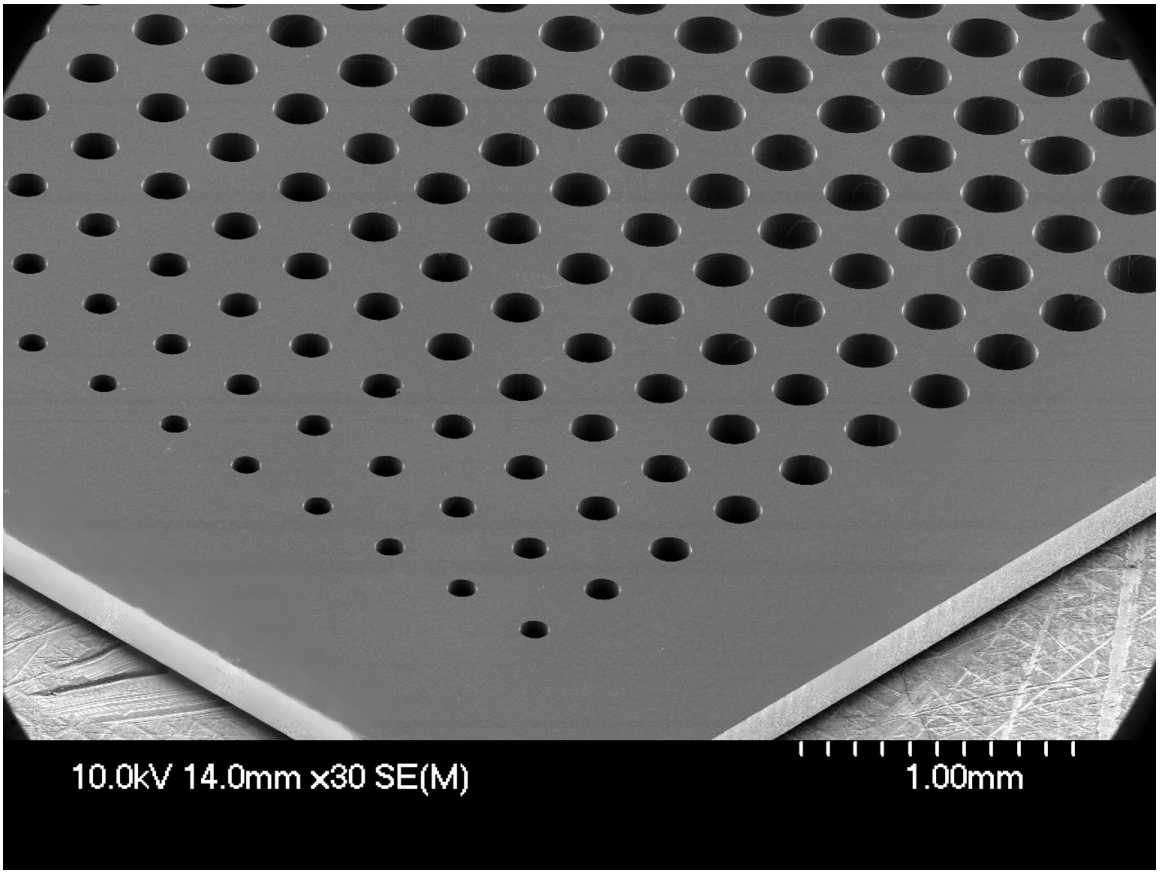

This chapter covers all of the experimental fabrication and characterization methods used throughout the research. It includes the fabrication of SAW devices, phononic structures and the pattern of hydrophobic regions on surfaces as well as the immobilization of antibody on surfaces and the preparation and manipulation of malaria infected cells.

3.1 Microfabrication

In this section, the microfabrication methods for the devices developped during this thesis are described. The three main methods are the fabrication of the SAW device, the fabrication of phononic crystals and the modification of the surface chemistry to create hydrophobic patterns.

3.1.1 Mask

The masks of the IDTs, the phononics and the hydrophobic patterns were designed using the computer aided design (CAD) software L-Edit (Tanner EDA) and acetate masks were obtained from JD Photo-Tools (Photo Data Ltd). This type of mask gives a resolution of 2 μm (http://www.jdphoto.co.uk/).

3.1.2 SAW device

The SAW device comprises an interdigitated electrode on a piezoelectric wafer fabricated using standard photolithography and metalization. The pattern consisted in interdigitated transducers designed either with straight electrodes as shown in Figure 2.6, a tapered IDT or a chirped IDT discussed later.

As shown in Figure 3.1, the piezoelectric wafer ($LiNbO_3$) was first coated by spinning AZ4562 photoresist (30 s at 4000 rpm) for a thickness of 6.2 μm and dried on a hotplate for 2 min at 100 °C. The pattern was transferred by UV exposure for 15 s (MA-6, SUSS Micro Tec AG) and developed using AZ400K (1:4 in deionized (DI) water) for about 3 min. The wafer was then placed in asher for 1 min at 100W to remove the remaining resist. A 20 nm titanium adhesion layer was evaporated prior to deposition of 100 nm of gold and the lift-off was then performed in acetone.

A micrograph of a typical SAW device after the fabrication is shown in Figure 3.2.

3.1.3 Phononic structures

The phononic crystals structures consisted exclusively of an array of holes in silicon. They were fabricated by etching a silicon wafer.

As shown in Figure 3.3, a 4-inch $< 100 >$ silicon wafer with a thickness of either 220 μm or 470 μm was spin-coated with 20 μm thick AZ4562 photoresist (30 s at 500 rpm). The pattern was transferred into the resist layer by UV exposure for 15 s (MA-6, SUSS Micro Tec AG) and development using AZ400K (1:4 in DI water). A post-baking

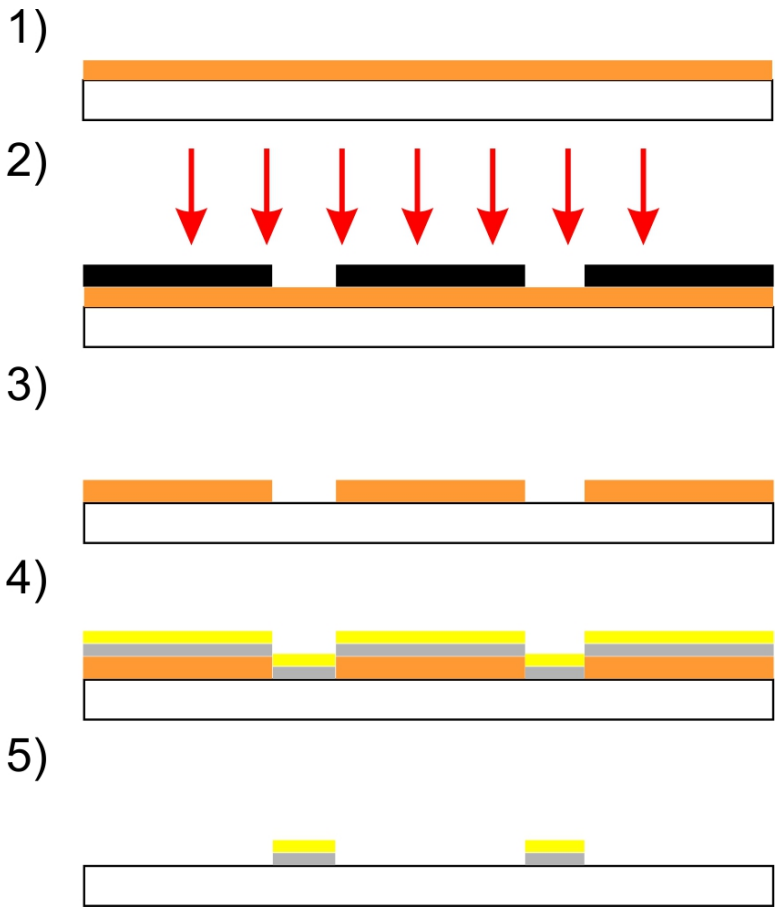

Figure 3.1: Fabrication of the electrodes by (1) spin-coating of photoresist, (2) pattern transfer by UV exposure, (3) development, (4) deposition of 20 nm titanium layer and 100 nm of gold and (5) lift-off.

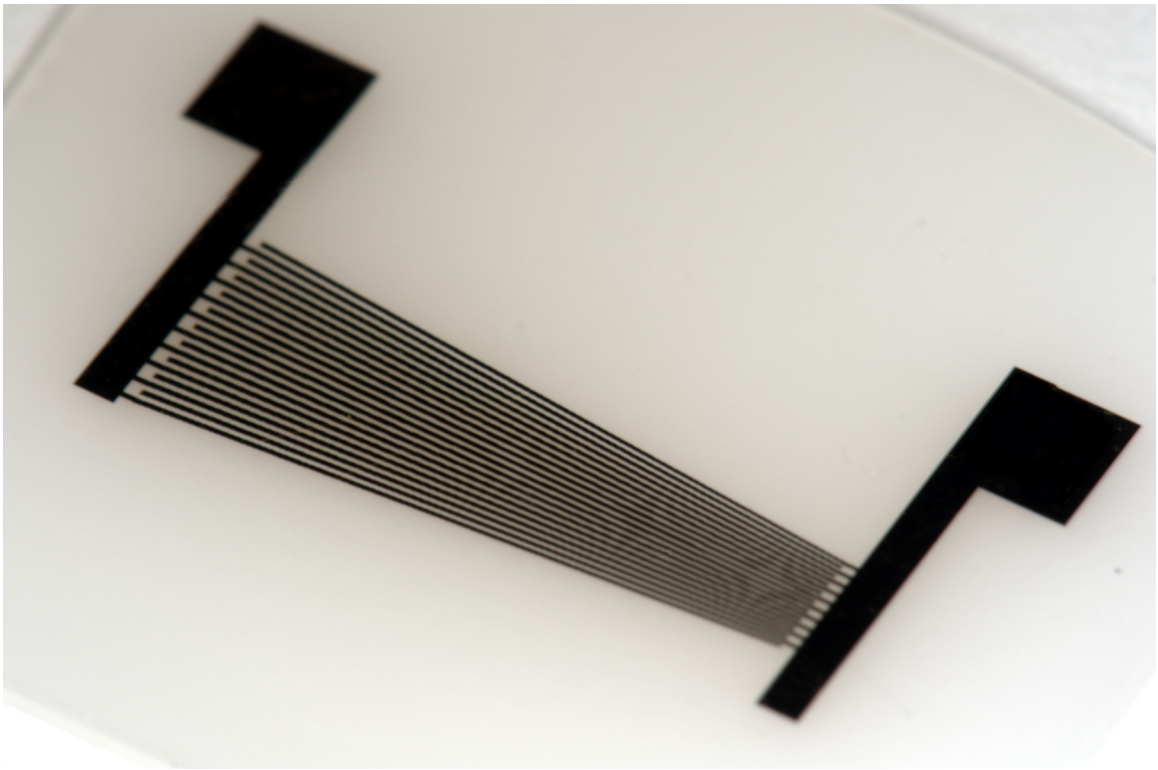

Figure 3.2: Micrograph of a typical SAW device made of gold electrodes on $LiNbO_3$ after the fabrication process.

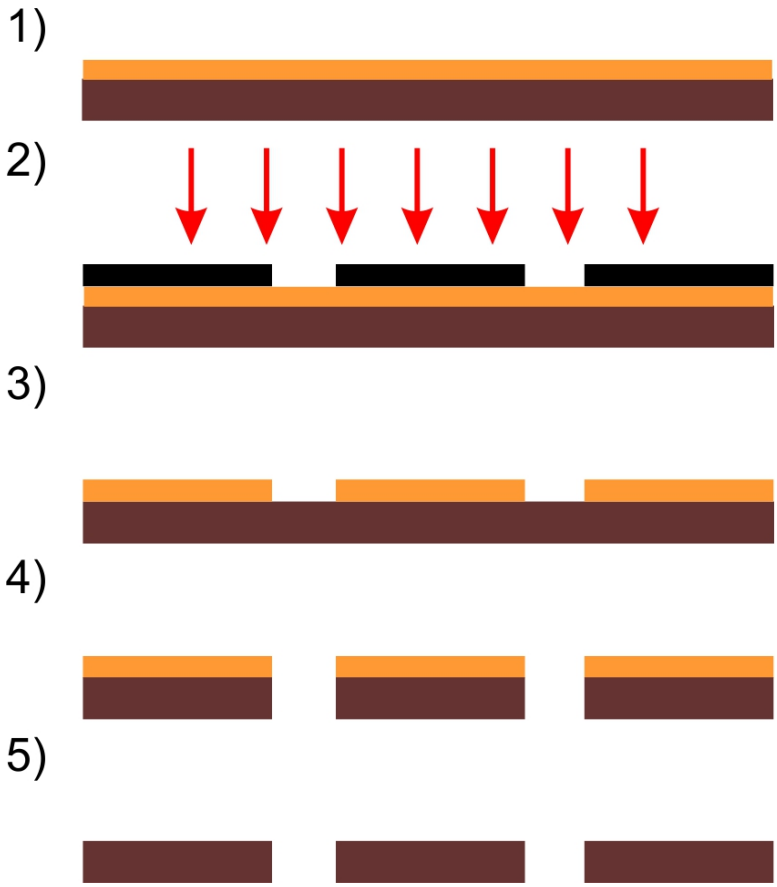

Figure 3.3: Fabrication of the phononic structures by (1) spin-coating of photoresist, (2) pattern transfer by UV exposure, (3) development, (4) deep reactive ion etching and (5) cleaning.

step was made at 120 °C for 30 min in an oven. The pattern was then transferred into the $< 100 >$ silicon using deep reactive ion etching (STS ICP) by alternating steps of SF_6/O_2 etching and C_4F_8 passivation cycles during the required amount of time (75 min to etch completly through the wafer). The structure was aligned to the [011] direction of the silicon wafer in such manner that the propagation direction of the Lamb waves was parallel to the [011] direction. The wafer was cleaned in acetone, then in piranha solution (3:1 concentrated sulfuric acid to 30% hydrogen peroxide solution), and cleaved to provide the individual superstrates.

An scanning electron micrograph (SEM) of a phononic structure obtained after the fabrication process is shown in Figure 3.4.

3.1.4 Hydrophobic patterns

Hydrophobic patterns were used in most of the experiments in order to position reproducibly a droplet in a spot or to move a droplet along a track.

The design of the spots or track were first made using the CAD software L-Edit (Tanner EDA) and an acecate mask was obtained from Scan-Hi Digital Limited.

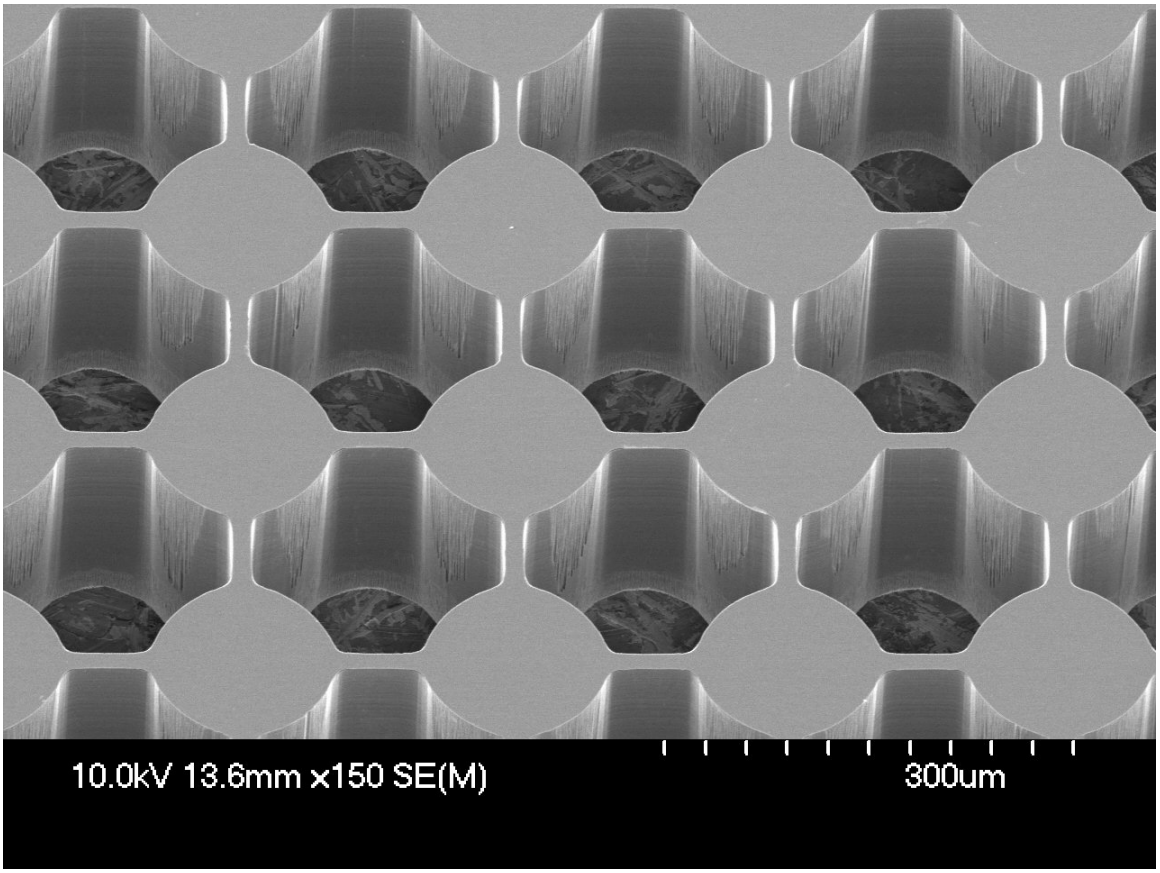

Figure 3.4: SEM of a phononic structure (here a sping-mass lattice) after the fabrication process where holes have been etched thru the silicon.

As shown in Figure 3.5, the surface of the device (etiher $LiNbO_3$, glass, or silicon) was coated with AZ4562 photoresist (30 s at 4000 rpm) for a thickness of 6.2 μm and the pattern was transferred into the photoresist by UV exposure for 15 s (MA-6, SUSS Micro Tec AG) and development using AZ400K (1:4 in DI water). The surface was then treated in asher for 2 min at 100 W before silanisation in a solution of 30 μl of trichloro(1H,1H,2H,2H-perfluorooctyl)silane (Aldrich) in 50 ml of heptane for 10 min. The photoresist was removed in acetone and the glass was rinsed with methanol and blow-dried.

3.2 Characterization

In this section, the principle methods used to characterize the SAW devices and the phononic strucutres are described. The scattering parameters of the SAW devices were characterized using a Network analyzer. The propagation of waves were characterized using either a infrared (IR) camera or a laser doppler vibrometer (LDV) and the temperature of the fluids were controlled using a thermal camera. SEM was used to determine the shape of the phononic structures.

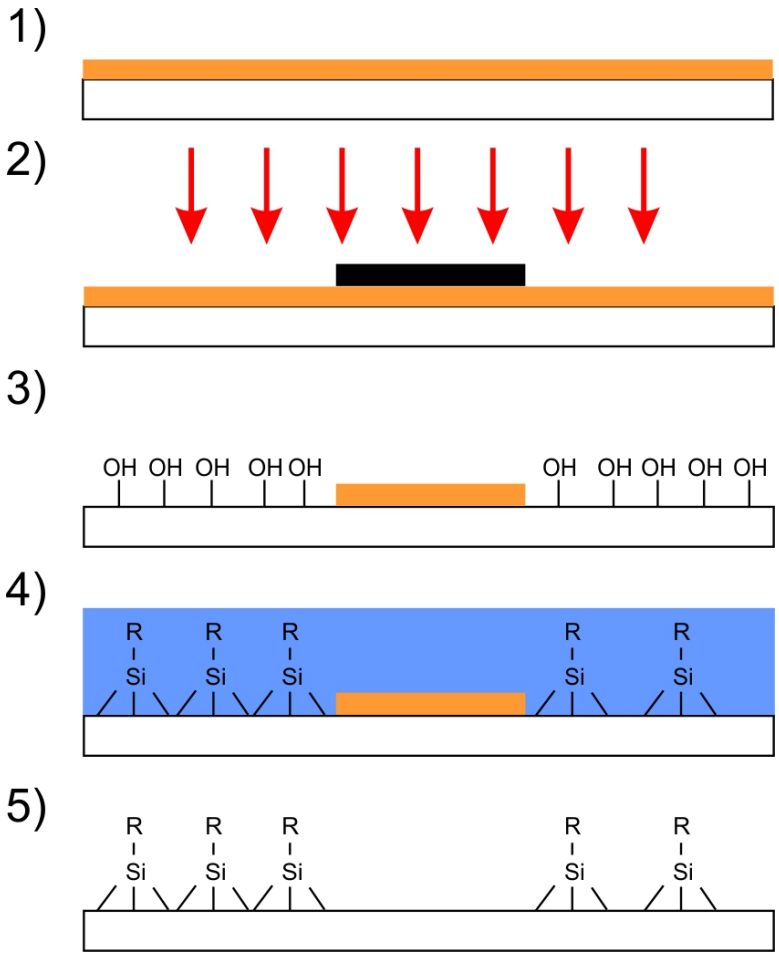

Figure 3.5: Creation of hydrophobic patterns by (1) spin-coating of photoresist, (2) pattern transferr by UV exposure, (3) development and plasma oven, (4) silanisation and (5) cleaning.

3.2.1 Reflection coefficient

A way to determine the reflection coefficient of the SAW devices is to measure their scattering parameters (S-parameters). The S-parameter describes an electrical network as a black box and has information in both the magnitude and phase of the signal. It is influenced by the frequency and the impedance of the load and the source. The S_{11}-parameter gives information on the reflection coefficient while the S_{21}-parameter describes the forward transmission coefficient.

To characterize the reflection coefficient of the interdigitated transducers, the S_{11}-parameter was measured with an Agilent Technologies E5071C ENA series network analyzer. The SAW device was directly connected to the network analyzer and the S_{11}-parameter was recorded.

3.2.2 Wave coupling

The wave coupling from the piezoelectric substrate into the superstrate was characterized by using a SAW device as superstrate and recording the S_{21}-parameter. The waves were generated from the first IDT and propagated along the surface. When arriving at the coupling layer, the waves were transmitted into the superstrate before reaching the second IDT where the electric charges propagating on the surface of the piezoelectric superstrate couple into the electrodes. By measuring the S_{21}-parameter, which describes the forward transmission coefficient, it was possible to investigate the efficiency and the stability of the coupling layer.

3.2.3 Waves propagation

Two methods were used to observe the wave propagation.

Infrared camera

A IR camera (FLIR i60; FLIR Systems) was used to observe the propagation of the waves on the glass coverslip. The thermal diffusion being very low in glass, it was possible to observe the position of the propagation of the waves as they heat the substrate due to internal friction. The position and intensity of the waves were then further analysed using the image processing software ImageJ (http://rsb.info.nih.gov/ij/).

Vibrometer

A laser doppler vibrometer (LDV, Polytec Inc.) was used to quantify the displacement in z-direction of the waves on the surface. A sinusoidal signal was applied to the device in order to generate a SAW and the amplitude of the vibration (in pm or nm) was recorded at the choosen position. The device was mounted on a moving stage and a home made macro (Visual Basic, Microsoft) was used in order to control a moving stage and scan a defined area of the sample.

3.2.4 SEM

In order to verify the shape of the fabricated phononic structures, scanning electron micrograph of the samples were obtained. All scanning electron micrographs were taken using a Hitachi S-4700 SEM operating at 10kV. The samples were first cleaned in piranha solution and blow-dried. As this technique was used only to observe the phononic structures on silicon, further coating was not required.

3.3 Antibody immobilization

In this section, the methods to immobilize antibody on a defined spot on a glass coverslip and on carboxylated beads are described. It also includes the blocking of the different surfaces and their storage.

3.3.1 Glass surface

Monoclonal antibodies were covalently bound onto a defined 3 mm diameter spot on disposable superstrates fabricated using glass coverslips (22x22 mm, 0.17 mm thick, Menzel-Gläser). The superstrates were treated in O_2 Plasma for 2 min at 100 W before silanisation in a solution of 30 μl of trichloro(1H,1H,2H,2H-perfluorooctyl)silane (Aldrich) in 50 ml of heptane (Heptane CHROMASOLV®Plus, Sigma Aldrich) for 10 min. They were then coated with AZ4562 photoresist, patterned using standard photolithography and developed using AZ400K. The pattern comprised a diagonal channel (width 3 mm, length 20 mm, angle 45°). The glass coverslips were treated in O_2 Plasma for 2 min at 100 W before silanisation in a solution of 50 μl of (3-Aminopropyl)triethoxysilane (Aldrich) in 50 ml of heptane for 10 min. The photoresist was removed in acetone. The coverslips were then reacted in glutaraldehyde (1 % w/v in water) (Sigma-Aldrich) for 2 hours, rinsed with water and blow-dried. 2 μl of Human

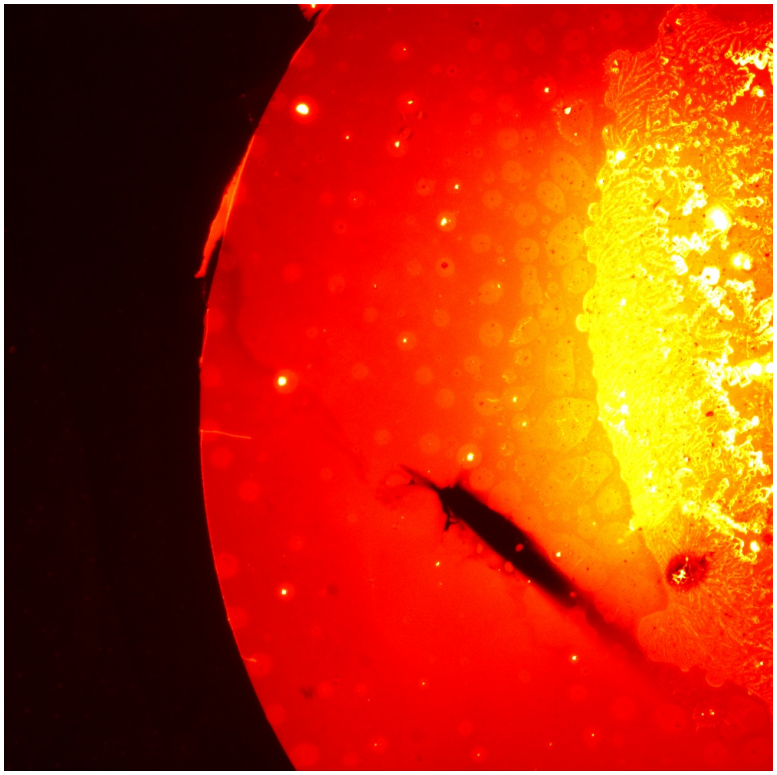

Figure 3.6: Fluorescent microscope observation of the presence of Human IFN-γ MAb attached to the surface of the coverslip using a secondary anti-mouse Ab labeled with TRITC.

IFN-γ MAb (100 μg ml^{-1} in PBS 1X) (Thermo Scientific, M700A) were deposited in the corner of the track and incubated overnight in a humid environment at 4 °C. The coverslips were washed three times with 500 μl of wash buffer (0.05 % w/v Triton X-100 in PBS 1X) and blocked overnight in a humid environment at 4 °C with 20 μl of blocking buffer (0.1 % w/v casein in PBS 1X). The wet superstrates were stored in a humid environment at 4 °C.

The presence of antibody on the surfaces was verified by covering the surface with an anti-mouse Ab labeled with rhodamine (1 mg ml^{-1}) and letting incubate for 2 h. The surfaces were then washed with PBS (1X) and the coverslips were observed under fluorescent microscope (Ex 520 nm, Em 560 nm). A image of the prescence of Ab on the surface is shown in Figure 3.6

3.3.2 Carboxylated beads

Latex beads, 2 μm in diameter, polystyrene carboxylate-modified (the charge density ranged from 30 to 300 $\AA^2$/charge group), fluorescent yellow-green, 2% (Sigma, L4530) were coupled with antibodies using a method similar to the one-step coating procedure described by Molecular Probes (Invitrogen). 150 μl of latex beads were washed twice (centrifugation during 5 min at 10000 rpm) with 150 μl of MES buffer (50 mM, pH 6).

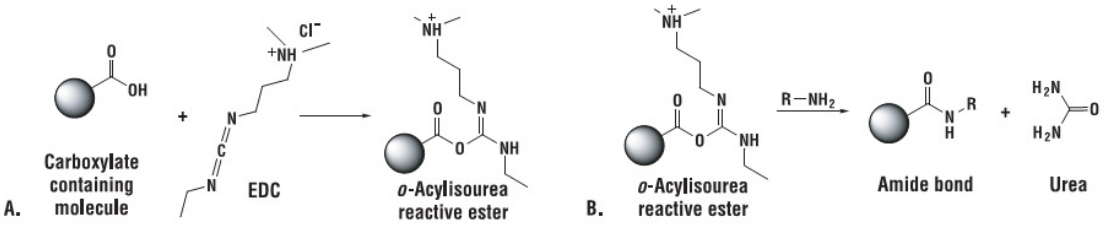

Figure 3.7: EDC coupling reaction scheme. (a) EDC reacts with carboxylic acid group and activates the carboxyl group to form an active *O*-acylisourea intermediate, allowing it to be coupled to the amino group in the reaction mixture. (b) An EDC byproduct is released as a soluble urea derivative after displacement by the nucleophile. (Pierce Biotechnology, Inc., 2005)

150 μg of Human IFN-γ MAb (Thermo Scientific, M701) were added to the beads and mixed. The beads were incubated at room temperature for 30 min. All incubations were performed on a slow tilt rotation table.

N-Ethyl-N-(3-dimethylaminopropyl)carbodiimide hydrochloride (EDC) (Sigma, E6383) was dissolved immediately before use. 30 μl of EDC solution was added to the beads/antibodies solution to activate the carboxyl groups, Figure 3.7, and incubated for 2 hours at 4 °C. 300 μl of Tris-HCL (50 mM, pH 7.4) was added to the solution and incubated for 30 min. The beads were further washed twice with Tris-HCL (50 mM, pH 7.4). Finally, the beads were re-suspended in a storage buffer (BSA 1 % w/v in PBS 1X) and stored at 5 °C.

3.4 Malaria infected blood

In this section, the preparation of the malaria infected red blood cells (iRBCs) and their observation is described.

3.4.1 iRBCs preparation

The iRBCs were provided by the Institute of Infection, Immunity and Inflammation (University of Glasgow). *P. falciparum* clone 3D7 was grown *in vitro* according to standard protocols using human erythrocytes obtained from the Scottish National Blood Transfusion Service. Parasites were tightly synchronised to obtain ring-stage parasites. Parasite samples for SAW analysis were pelleted by centrifugation (400 x g for 5 min) and resuspended in culture medium (RPMI1640 with 10% human serum) at 40% haematocrit, to mimic that seen in human blood. Thin blood smears were prepared and stained with 5% Giemsa's stain for 40 min and examined under 1000x magnification

(oil immersion), with a minimum of 100 parasites counted to obtain an accurate estimate of parasitaemia. Serial dilutions were performed using uninfected human blood in culture medium (RPMI1640 with 10% human serum) as the diluent, from that in the culture (∼2.4%) down to a final parasitaemia of 0.0005%.

3.4.2 Fluorescent microscopy

A MOTIC Inverted phase fluorescence microscope was used as a method to quickly observe the presence of malaria infected red blood cells. 10 μl of acridine orange (stock solution of 0.15 mg ml^{-1}) was added to 1 ml of infected blood before the SAW process and the resulting solution was directly observed under a fluorescent microscope (Ex 480 nm, Em 535 nm).

Chapter 4

Shaping waves

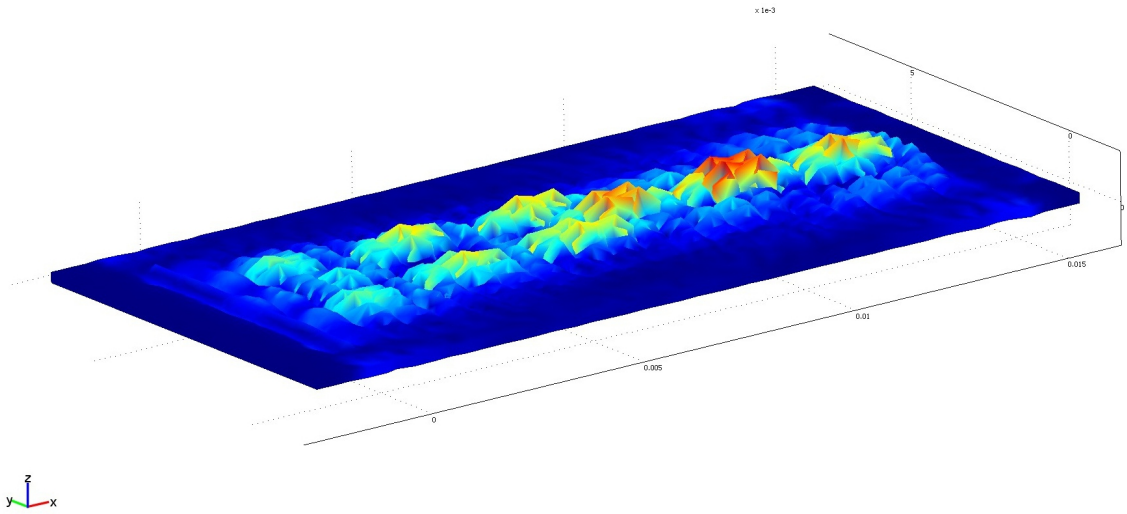

In this chapter, the notion of shaping waves for microfluidics is introduced. While most of the research made so far in the field of SAW microfluidics involve standard straight electrodes and often require multiple eletrodes, the slanted (or tapered) IDT is demonstrated here as a powerful method to control the position of the waves in a tuneable manner, both on the surface of the piezoelectric device and on a superstrate. A gradient-index phononic crystals lens was designed, manufactured and characterized to focus energy and phononic band gap structures were built to create tuneable asymmetric wave propagations.

4.1 Tuneable Surface Acoustic Waves

As introduced in Chapter 1, global rotational motion can be induced in a droplet by breaking the symmetry of the SAW, and the resulting flow pattern concentrates

particles within the liquid due to motions which have similarities to those described as Batchelor flows [6, 105].

The techniques presented in the litterature for particle concentration involve either aligning a drop on the edge of a standard IDT [165], or positioning a gel to partially absorb the SAW reflection (so that only part of the drop lies in the transmission pathway [68]). Alternatively, more complex IDTs can be designed, including those which focus the SAW using circular transducers with a fixed frequency and excitation pathway [121]. These methods necessitate a precise positioning of the droplet and allow only a single function to be performed by the IDT. In order to achieve multiple fluid functions, complex circuits with multiple IDTs would be required. Consequently, this complexity has led to only limited results in the integration of different SAW fluid manipulation techniques, onto a single chip.

In the field of SAW microfluidics, it has also been reported that the Rayleigh wave, which is normally generated in the piezoelectric wafer, can be coupled into a disposable superstrate as a Lamb wave, providing a clear route by which LOC technology can be applied to low-cost, point-of-care diagnostics [51]. In this configuration, the surface acoustic excitation in the piezoelectric wafer is coupled into the superstrate through a thin liquid film interface.

Here, a new concept in SAW microfluidics which combines the use of a disposable glass superstrate with a slanted finger IDT is demonstrated. The technique provides a powerful method by which it is possible to handle droplets and particles in a programmable fashion. For example, droplet movement, merging and centrifugation are demonstrated on the same substrate, by simply changing the SAW excitation frequency to achieve a high degree of functional integration.

Slanted finger IDTs have been used in data terminals as mid-band and wide-band filters [163]. The theory of using slanted electrodes in microfluidics has been described, although practical realization of such devices has not been demonstrated, either on piezoelectric substrates or on disposable superstrates [150].

4.1.1 Experimental

The SAW amplitude excited by a slanted IDT is not uniform and different profiles can be obtained by tuning the input frequency. According to Equation 2.9, the resonant frequency, f, is dependent upon the periodicity of the fingers L, and the sound velocity on the piezoelectric wafer, c. Consequently, for a given input frequency, the SAW

output is only generated when the gap ($D/2 = L$) between the fingers satisfies the ability of the electrodes to support the resonance, Figure 4.1a. The effective aperture Ap_{eff} of the excited SAW beam can be approximated by [162]:

$$Ap_{eff} = \frac{1}{n}\frac{f_c}{f_h - f_l}A_0 \tag{4.1}$$

where n is the number of pairs, f_c, f_h and f_l are the center, highest and lowest frequency, and A_0 is the horizontal length of the IDT. Divergent IDT electrodes were fabricated where both the electrode separation ($D/2$) and their width ($D/2$) varied linearly from 62.5 μm to 125 μm along the aperture. This corresponds to wavelengths of 250 μm to 500 μm and a range of frequencies from 16 MHz to 8 MHz on 128° Y-cut X-propagating 3 inch $LiNbO_3$ wafer, where $c = 3990\, ms^{-1}$. 10 pairs of fingers were used with a horizontal length of 15 mm, which would give an estimated effective apperture of 2.25 mm according to Equation 4.1. The IDTs were patterned using a lift-off process. After pattern transfer into an AZ4562 resist, a 20 nm titanium adhesion layer was evaporated prior to deposition of 100 nm of gold. Lift-off was then performed in acetone (for more details, see chapter 3.1.2). An Agilent Technologies MXG Analog Signal Generator N5181A was used in conjunction with a Mini Circuits ZHL-5W-1, 5500 MHz amplifier and a 3 A, 24 V DC power supply to power the SAW device. The wafer was fixed with thermal paste on a heat sink to avoid overheating.

The S_{11}-parameter was measured to characterize the IDT and showed a stable response for frequencies between 8 MHz and 14 MHz (Figure 4.1b, inset).

Figure 4.1a shows a schematic representation of the slanted IDT with the propagation of the SAW on a $LiNbO_3$ wafer for a selected input frequency of 13 MHz. That part of the IDT that supports the resonance condition is mostly excited, resulting in the propagation of a SAW with a small aperture around 2 mm, which is consistent with the theoretical aperture calculated with Equation 4.1. By tuning the frequency, it is possible to control the lateral position of the excitation wave, as shown theoretically and experimentally in Figure 4.1b. The aperture was characterized for input frequencies from 8 to 16 MHz with steps of 0.1 MHz at a power of 320 mW, by observing under microscope the discrete response of the agitation of an array of 8 droplets of 1 μl arranged in front of the IDT (hydrophilic spot of 1 mm diameter every 2 mm).

The same spatial control of the SAW, using the excitation frequency, can be extended to applications involving the use of a superstrate (Figure 4.1b). In this case, we used an unmodified glass cover slip as the superstrate, and directly compared the

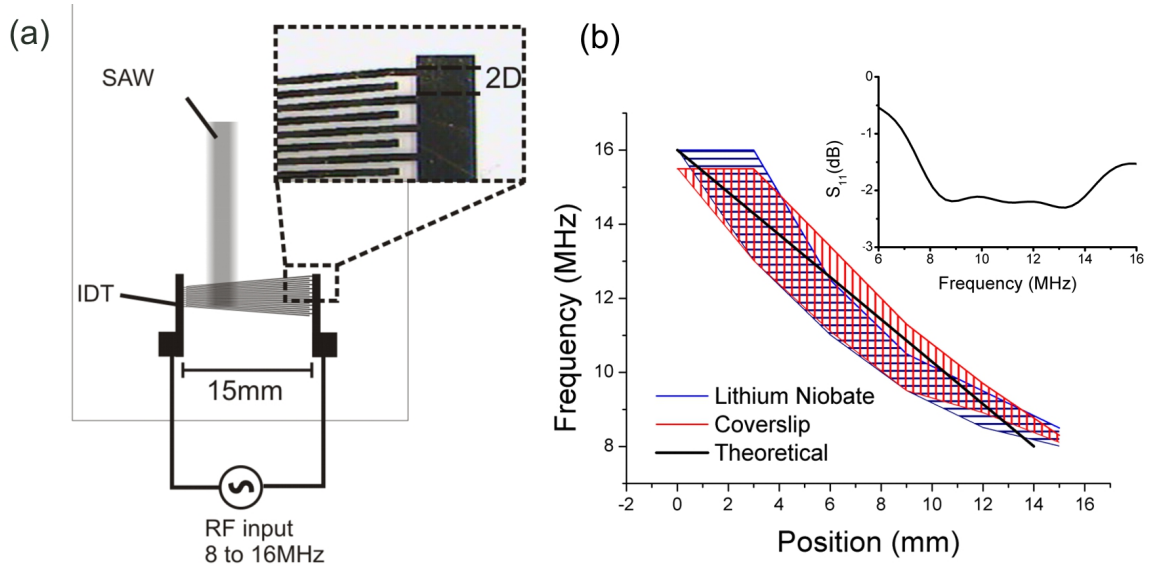

Figure 4.1: (a) A schematic representation of the slanted IDT and the surface acoustic wave. (b) The experimental input frequency needed to actuate a droplet on the surface of the $LiNbO_3$ wafer as well as on a cover slip coupled onto it as a function of the position and the theoretical calculation of the centre of the highest intensity SAW pathway. The aperture was characterized for input frequencies from 8 to 16 MHz with steps of 0.1 MHz at a power of 320 mW, by observing under microscope the discrete response of the agitation of an array of 8 droplets of 1 μl arranged in front of the IDT (hydrophilic spot of 1 mm diameter every 2 mm). The measurment errors are ± 0.05 MHz and ± 0.5 mm and are not shown in the graph for visualisation purpose. The inset shows the magnitude of the S_{11}-parameter obtained with an Agilent Technologies E5071C ENA series network analyzer.

position of the SAW at given frequencies with respect to the native $LiNbO_3$ wafer. We found that the width of the SAW at a given frequency on the superstrate was larger (16 % on average) than that directly on the piezoelectric wafer, due to diffraction of the wave in the process of the coupling.

4.1.2 Results and Discussion

Concentration of beads

The concentration of 10 μm polystyrene beads was achieved in 10 μl water droplets over the IDT width, by simply tuning the frequency as shown in Figure 4.2a and b. The droplet was positioned 9 mm from the left of the IDT. The frequency was chosen using Figure 4.1b as a guide, so that only part of the drop lies in the SAW transmission pathway, thus breaking the symmetry of the acoustic wave. The direction of the stream can be controlled by tuning the frequency. For example, in Figure 4.2b left, the SAW excited with a frequency, f_1, of 9.6 MHz interacted with the right side of the droplet inducing an orbital momentum and creating an anti-clock-wise streaming. In Figure 4.2b right, for a SAW excitation frequency, f_2, of 11 MHz, the flow was clockwise.

In Figure 4.2c, the time needed to concentrate 10 μm polystyrene beads in the centre of a 10 μl droplet positioned at 9 mm from the left of the IDT directly on the $LiNbO_3$ as a function of the input frequency (or the equivalent position of the SAW) is reported. The range of frequencies over which excitation occured was dependent upon the size of the sample. For example, with a drop diameter of 3 mm, using Figure 4.1b, it was possible to estimate that the SAW would interact with the fluid over a range of frequencies between 9 and 11 MHz. This prediction was confirmed by data presented in Figure 4.2b where centrifugation was only observed at frequencies between 9.2 and 11.0 MHz (the shaded areas represent frequencies at which no centrifugation was observed).

For frequencies between 10 MHz and 10.2 MHz, although some vibrations can be seen in the droplet, no rotational motion occurred because the SAW is symmetrically transmitted to either side of the centre of the droplet and, consequently, no angular momentum is generated. Furthermore, the time needed to achieve a complete centrifugation of 10 μm beads decreased as the centre of the generated aperture moved closer to the centre of the drop. This phenomenon can be explained by the fact that the SAW approaches the centre of the drop, the amount of fluid interacting with the acoustic wave increases, resulting in more energy being transmitted into the droplet.

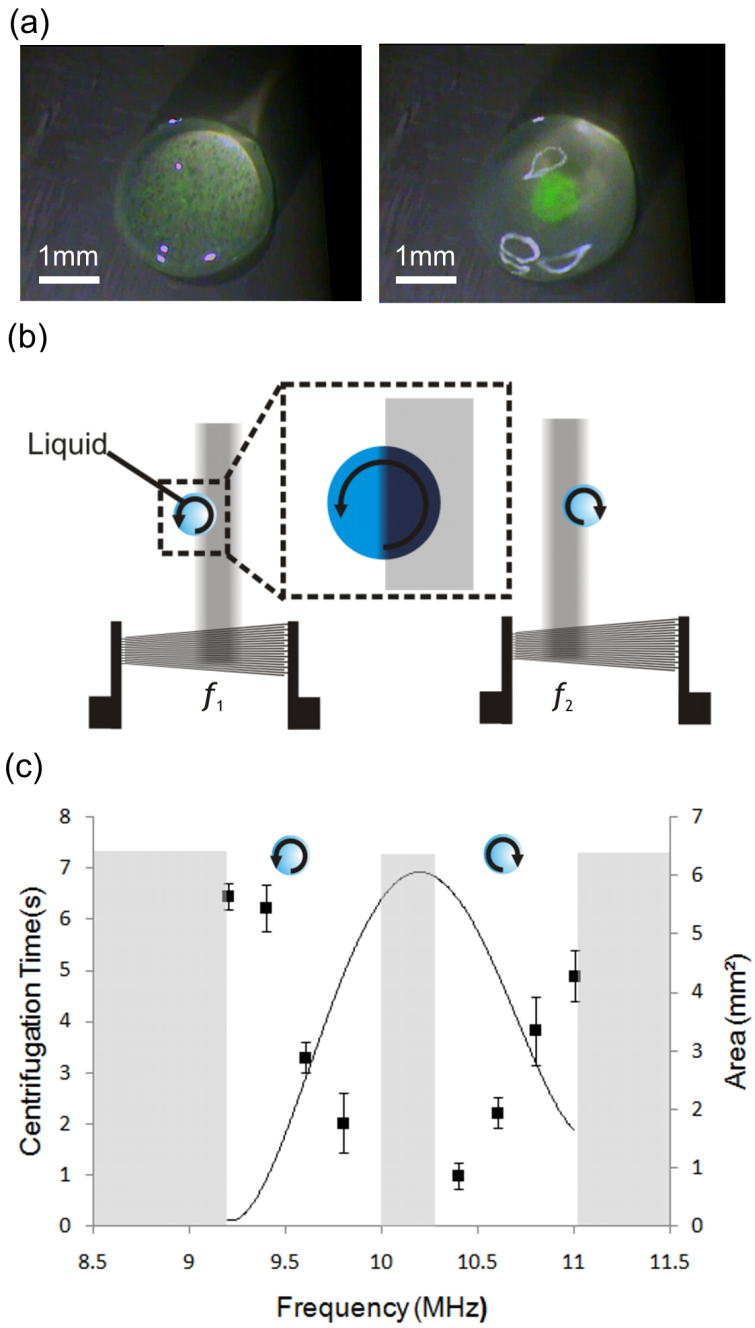

Figure 4.2: (a) A picture of a 10 μl droplet containing 10 μm polystyrene beads on the surface of the $LiNbO_3$ wafer (3.5 x 10^6 beads per ml, Duke Scientific G1000) before (left) and after (right) actuation with the SAW. (b) Schematic showing the anti-clockwise and clockwise streaming induced by SAW for f_1 = 9.6 MHz and f_2 = 11 MHz, respectively. The corresponding streaming direction observed is indicated by arrows. In the left image, the SAW interacts with the right side of the droplet and creates an anti-clockwise streaming, whilst, in the right image, the SAW interacts with the left side of the droplet and creates a clockwise streaming. In the detailed schematic, the darker shaded area represents the surface of the drop interacting with the SAW. (c) A graph of the actuation time needed to concentrate 10 μm beads in the centre of the 10 μl droplet, positioned at 9 mm from the left of the IDT as a function of the input frequency (equivalent to the position of the SAW) at 125 mW. The grey areas shaded on the graph represent frequencies where no concentration is occurring. Three sets of measurements were averaged for frequencies between 9.2 MHz and 11.0 MHz with a step of 0.2 MHz. Error bars are standard deviations. The data were obtained from videos (25 images s^{-1}) analyzed with Time Series Analyzer plug-in in ImageJ software. The curve represents the calculated area of the interface between the wave and the fluid, estimated geometrically.

In this respect, Figure 4.2c shows the calculated area of the interface between the wave and the fluid, extracted from the input frequency and its correspondence to the SAW aperture in Figure 4.1.

Movement, merging and mixing

Far from being limited to particle concentration, the slanted IDT provided the opportunity to programme multiple functions with a single electrode. It was possible to move, merge, mix and centrifuge a droplet on a glass superstrate by tuning the frequency of the input signal. To illustrate the power of this technique, a simple hydrophobic cartridge covered with hydrophilic dots (radius = 80 mm, pitch = 200 mm), defining a track, Figure 4.3 [127] was created.

At the beginning of the procedure, a droplet of 2 μl of hydroxylamine hydrochloride (1.67 mM) and sodium hydroxide (3.33 mM) (pH 9.0) and a droplet of 2 μl of silver nitrate (10 mM) were pipetted onto the chip as shown in Figure 4.3a. By applying the frequency f_3 (11 MHz) at 3.2 W, the left hand droplet (of silver nitrate) was moved towards the centre of the cartridge. Upon switching to the frequency f_4 (9.2 MHz), the right hand droplet (NaOH and hydroxylamine hydrochloride) was moved to the centre (Figure 4.3b), where it merged with the first droplet (starting the reduction of the silver salt to form colloidalsilver). In Figure 4.3c, the frequency f_5 (9.6 MHz) was applied to induce streaming in the droplet, resulting in the mixing of reagents and concentration of the silver colloid formed.

4.2 Stopband

SAWs have shown great potential to perform ultrafast concentration in which particles or cells are collected within a fluid [165]. Such devices work by breaking the symmetry of the propagation of the waves, in order that only part of the droplet interacts with the acoustic energy, generating rotational fluid streaming as described in the previous section. However, when performing such tasks on a disposable superstrate, difficulties arise from the positioning of the chip, which defines the extent of the assymetry in the propagation of the wave, and the energy loss in the process of coupling.

In this section, a method to split the symmetry of the SAW by using a stop band created by phononic crystals is demonstrated [166]. The phononic crystals allowed the manipulation of the waves directly on the superstrate. The band structures of the

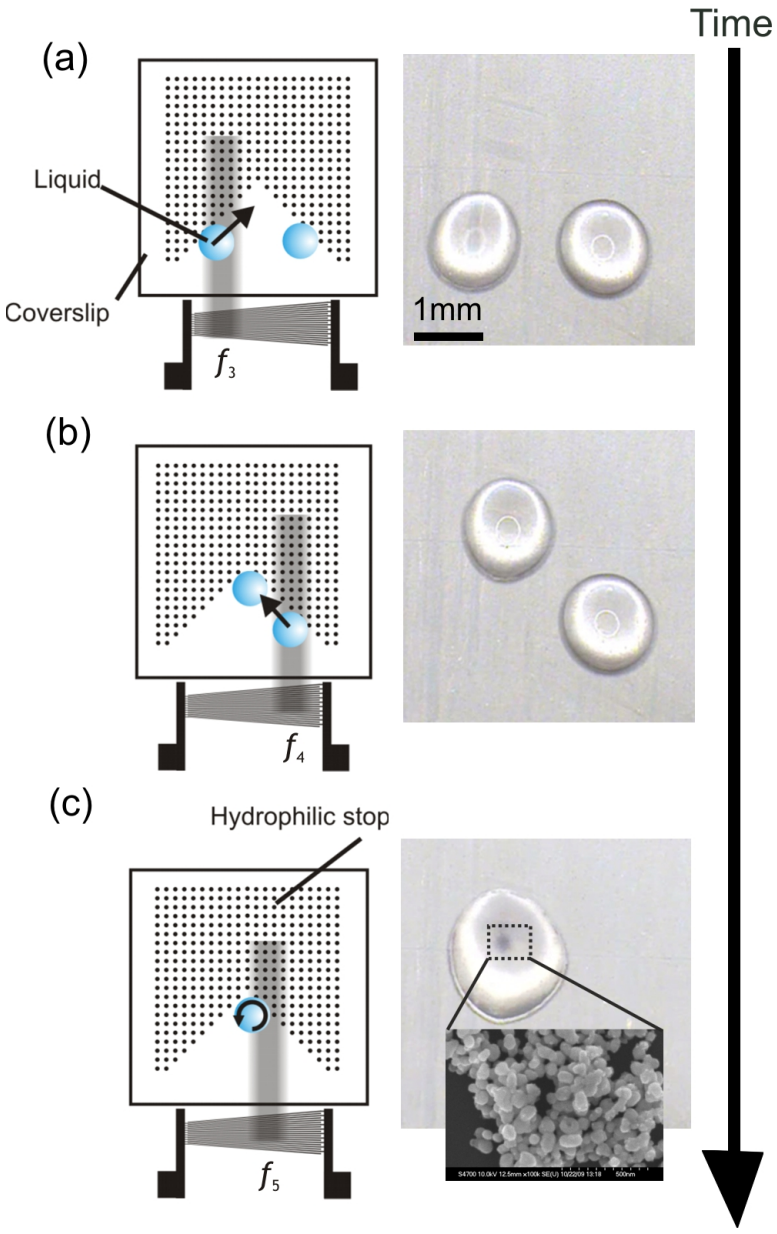

Figure 4.3: (a-c) Schematic representations of the device showing stills from a movie at the different stages during a series of fluid manipulations involving a 2 μl drop of hydroxylamine hydrochloride (1.67 mM) and sodium hydroxide (3.33 mM) and a 2 μl drop of silver nitrate solution (10 mM) being moved, merged, mixed and the reduced silver being concentrated, by centrifugation. The system comprises a slanted IDT coupled to a glass superstrate. The hydrophilic glass superstrate was patterned with a hydrophobic as described in Section 3.1.4 to produce an area of hydrophilic dots (r = 80 μm). Three different frequencies were used to navigate between each manipulation. f_3 (11 MHz) moves the left hand droplet to the centre, f_4 (9.2 MHz) moves the right hand droplet to merge it and f_5 (9.6 MHz) mixes and concentrates the reduced silver colloids in the centre of the droplet. The inset shows a SEM of the reduced colloids.

different lattice designs, including the square lattice [166], hexagonal [80] and mass-spring [62], were first investigated. Full 3D models were created and compared to experimental results.

4.2.1 Experimental

The phononic crystals stopband consisted of a thin perforated silicon plate, shown in Figure 4.4, 4.5 and 4.5. An array of holes forming a square covering half of the total width of the plate was etched through a 220 μm thick silicon wafer to create the filters using photolithography, pattern transfer and dry etching as described in Chapter 3.1.3. An SEM of the fabricated phononic lattices are shown in Figure 4.4a, 4.5a and 4.5a.

As shown in Figure 4.7c, SAWs were generated by applying a sinusoidal voltage on a chirped IDT [25] patterned on a lithium niobate wafer (the IDT fabrication is described in 3.1.2). The chirped IDT consisted in a transducer made of straight electrodes with a periodicty varying from 2000 μm to 200 μm, which allowed the generation of a wide range of frequencies from 2 to 20 MHz. Acoustic waves were coupled into the silicon phononic plate, surrounded by polydimethylsiloxane (PDMS) to absorb the waves and avoid reflections. To investigate the behaviour of the waves, a vibrometer (Polytec) was used to quantify the displacement in z-direction of the waves on the surface in the region of the phononic lattice.

4.2.2 Simulation

To design the phononic crystals band gap, the band structures of the square (Figure 4.4b), hexagonal (Figure 4.5b) and mass-spring lattices (Figure 4.6b) were calculated by the finite element method (COMSOL MULTIPHYSICS) along the boundary of the first irreducible Brillouin zone. A complete band-gap, shown by the grey area, was obtained for the square, hexagonal and mass-spring lattice for a 220 μm thick plate. The thickness of the plate has been choosen in order to reach the condition of band gap without compromising the solidity of the plate when it would be used as a disposable chip for diagnostics and the space required for microfluidic function which is in the milimeter scale.

Arrays of phononic structures were designed to form a square covering half of the width of the plate either with square, hexagonal or mass-spring lattice. The dimensions of the square, hexagonal and mass-spring lattice were designed such that the PCs exhibit a full bandgap and thus filter the waves as shown in Figure 4.4c, 4.5c and 4.5c,

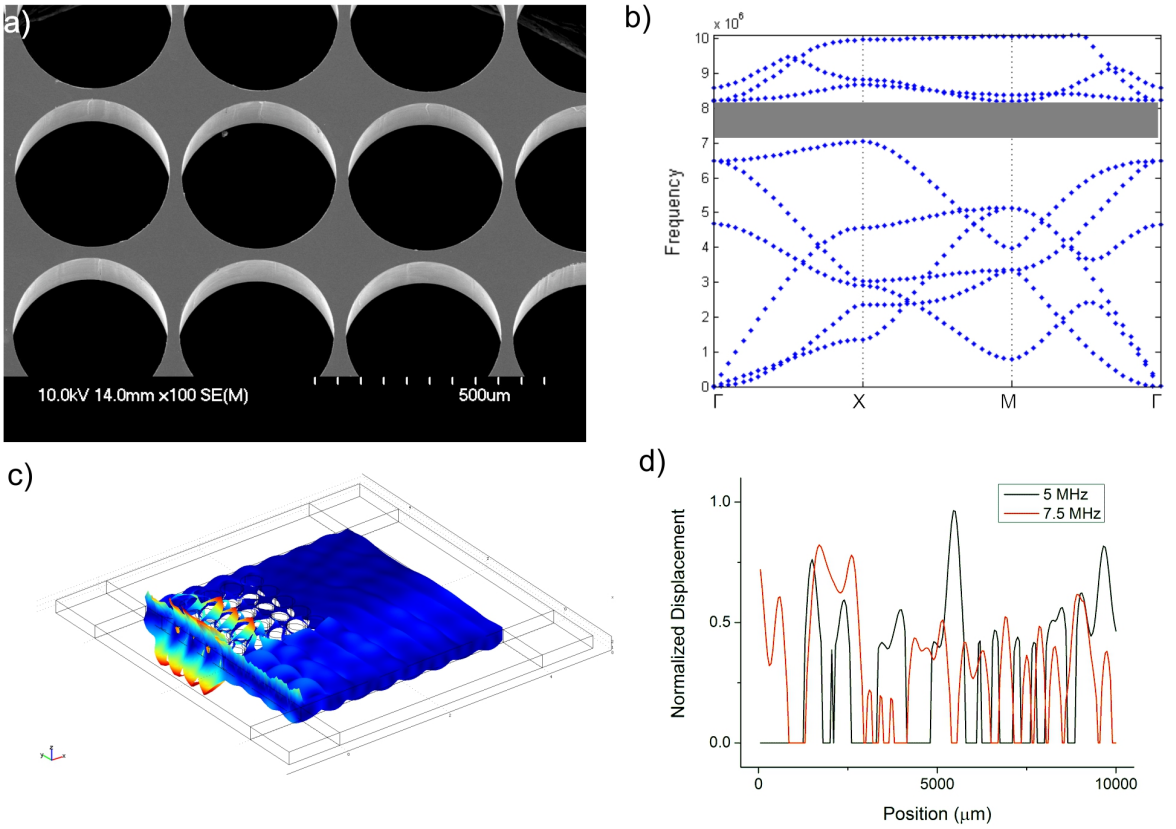

Figure 4.4: (a) SEM of the phononic structures of a square lattice; (b) band structure of the square lattice; (c) 3D simulation of the wave propagation in the plate comprising a filter region made with phononic structure; (d) experimental result showing the vibration on the surface across the structure.

Table 4.1: Dimensions and bandgap for the square, hexagonal and mass-spring lattice. (a is the lattice constant, r the radius of the disk, s the width of the spring.)

Lattice	Dimensions	Plate thickness (μm)	Bandgap (MHz)
Square	a = 400 μm, r= 184 μm	220	7-8
Hexagonal	a = 200 μm, r = 84 μm	220	8-10
Mass-spring	a = 200 μm, r = 70 μm, s = 15 μm	220	9-11, 15-16, 17-19

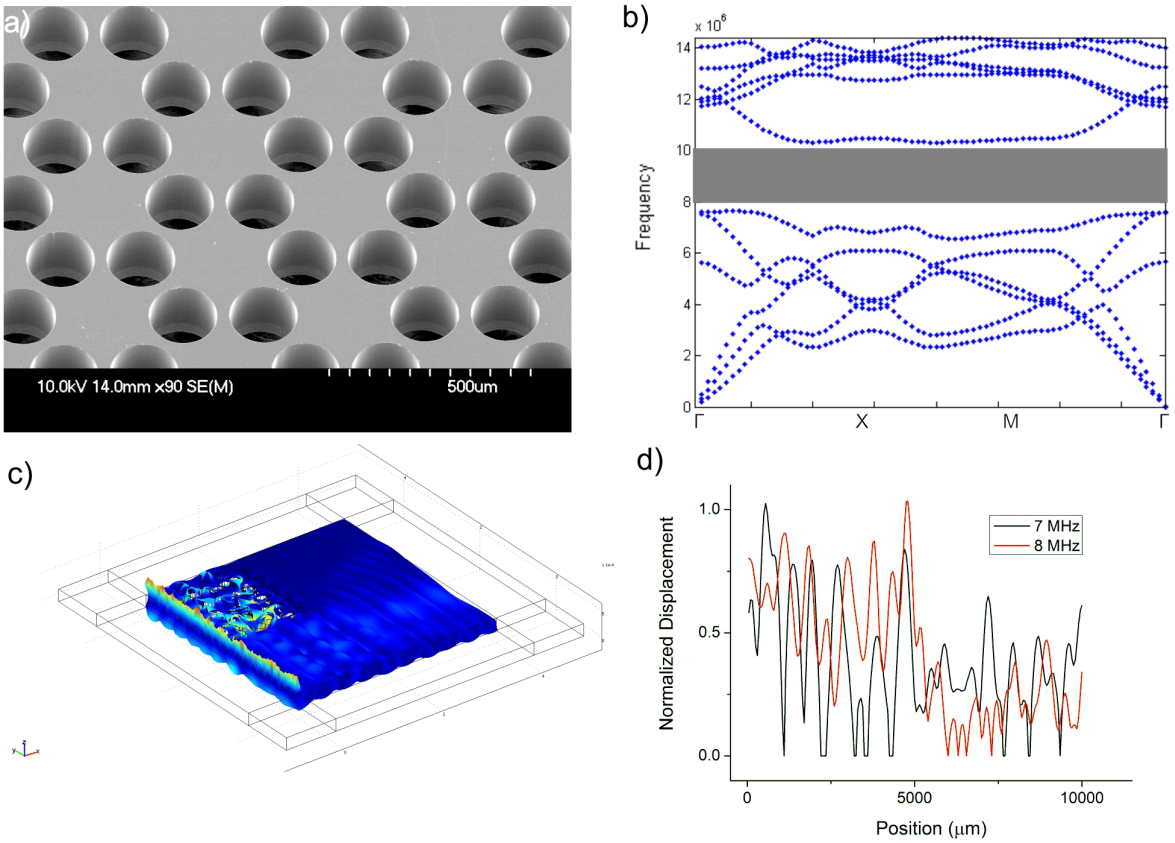

Figure 4.5: (a) SEM of the phononic structures of a hexagonal lattice; (b) band structure of the hexagonal lattice; (c) 3D simulation of the wave propagation in the plate comprising a filter region made with phononic structure; (d) experimental result showing the vibration on the surface across the structure.

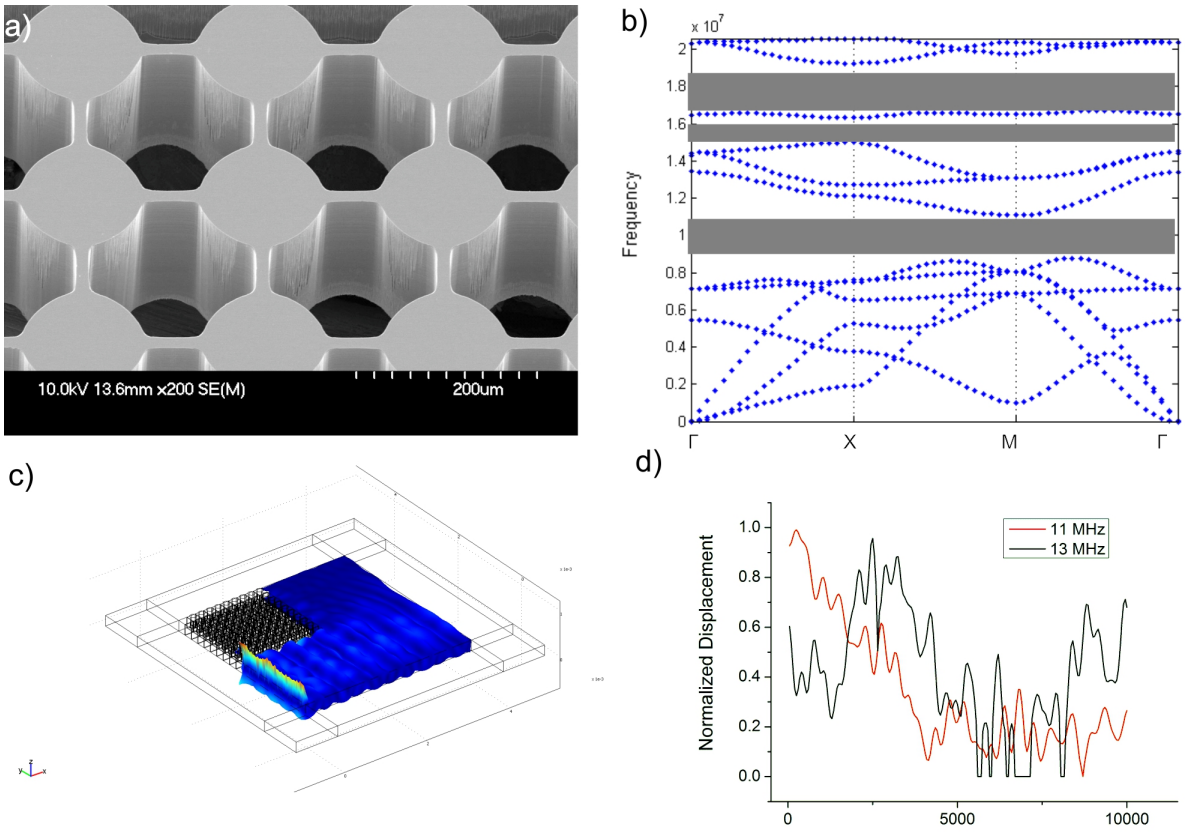

Figure 4.6: (a) SEM of the phononic structures of a mass-spring lattice (right); (b) band structure of themass-spring lattice; (c) 3D simulation of the wave propagation in the plate comprising a filter region made with phononic structure; (d) experimental result showing the vibration on the surface across the structure.

with frequency band gap between 7-8 MHz, 8-10MHz and 9-11 MHz respectively. The dimensions of each structures are showed in Table 4.1.

4.2.3 Results and Discussion

To understand the ability of the structures to filter the waves, numerical simulations of the full plates were conducted. The results in Figure 4.4c, 4.5c and 4.5c show a complete filtering of the waves for each lattice as expected. Nevertheless, it is also possible to observe the diffraction of the waves in the plate.

The phononic structures were then tested by observing the displacement of the surface using a vibrometer. Figure 4.4d, 4.5d and 4.5d shows the displacement as a function of the position on the substrate for a frequency inside (in red) and outside (in black) the band gap. The hexagonal structure gave the best contrast in the filtering between frequency inside and outside the band gap. The square lattice showed low filtering capabilities and almost no difference between frequency inside and outside the band gap. The mass-spring lattice showed a higher filtering for both frequencies.

As the interest is in the tuneabilty of the structures, the hexagonal structure was the most appropriate design. However, other constraints could lead to the choice of another design. For example, although the square lattice performed poorly, it created sufficient assymmetry of the waves on the surface to generate a rotational motion within a droplet [147].

In the case of the mass-spring lattice, it is interesting to notice that three bandgaps were found. It could be of interest notably for separating particles upon size where specific frequencies have to be used [113].

4.3 GRIN Lens

The focussing of elastic waves, and more particularly surface waves, has always been of great interest [131]. A focussing behaviour has been observed as the waves were directed into the slowest propagation group velocity from a surface wave excited by a pulse, depending on the angular dispersion of the spatial group velocity [69, 140]. Following on from this observation, attempts to focus surface waves have exploited the geometry of the transducers [78, 155, 66], but phononic lenses have not been practically demonstrated. These methods are limited by their reliance on actuators resulting in application specific devices. The gradient-index phononic crystal (GRIN-PC), by analogy

to the photonic gradient-index lens, has also been simulated in order to demonstrate the potential for focusing of acoustic waves [72, 151]. Although numerical models have demonstrated that a GRIN-PC allows acoustic wave focusing, making it suitable for applications such as flat acoustic lenses and acoustic wave couplers for both micro-electronic and microfluidics systems, it has not been experimentally demonstrated for surface waves.

Here, the focusing of surface waves by a GRIN-PC lens at the micrometre scale and megahertz frequencies is now experimentally and numerically demonstrate.

4.3.1 Experimental

The GRIN PC consisted of a thin perforated silicon plate, shown in Figure 4.7a. An array of 40 holes with a lattice constant, a = 400 μm, and a radius, r, varying from 60 to 160 μm, were etched into a 220 μm thick silicon plate. The holes were etched completely through the silicon wafer using photolithography, pattern transfer and etching, as described in Chapter 3.1.3. An SEM of the lens is shown in Figure 4.7b.

As shown in Figure 4.7c, SAWs were generated by applying a sinusoidal voltage on a chirped IDT patterned on a lithium niobate wafer (the IDT fabrication is described in Chapter 3.1.2). Acoustic waves were coupled into a silicon phononic thin plate, surrounded by PDMS to absorb the waves and avoid reflections. To investigate the behaviour of the waves, a vibrometer (Polytec) was used to quantify the displacement in z-direction of the surface.

4.3.2 Simulation

The band structure of the square lattice was calculated by the finite element method (COMSOL MULTIPHYSICS) along the boundary of the first irreducible Brillouin zone. It has previously been shown that the first antisymmetric (A_0) mode in thin silicon plates is weakly anisotropic, which makes designing the GRIN-PC plate practical [151]. Figure 4.8a shows the band structures of the A_0 mode with different filling fractions (ff) in the ΓM direction. The group velocity of the A_0 mode, which can be calculated by differentiating the curve, decreases with increasing ff. The refractive index, n, of the A_0 mode is approximated by the refractive index along the ΓM direction as

$$n = \frac{\nu}{\nu_{\Gamma M}} = \frac{\nu}{d\omega/dk_{\Gamma M}} \tag{4.2}$$

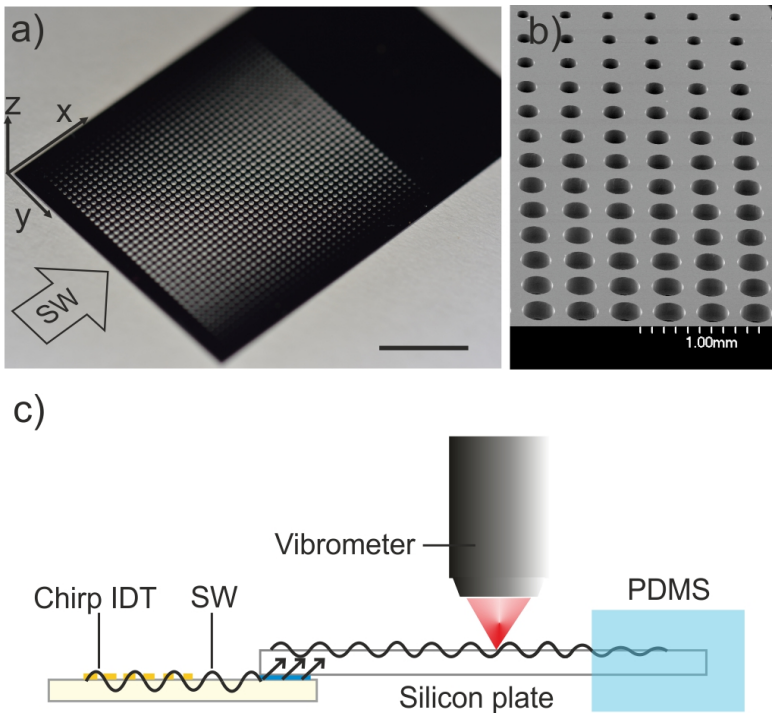

Figure 4.7: (a) Micrograph of the GRIN-PC lens. Scale is 5 mm. (b) SEM image of the holes etched completely through the silicon. (c) Schematic representation of the experiment (side view). The surface waves (SW) are generated by applying a sinusoidal voltage on a chirped IDT on a lithium niobate wafer. The waves are transmitted into the thin silicon plate through a layer of gel. The thin silicon plate was surrounded by a thick layer of PDMS to absorb waves and avoid reflections. A vibrometer was used to observe the displacement of the waves.

Where ν is the group velocity in a homogenous plate, $\nu_{\Gamma M}$ is the group velocity in ΓM direction of the phononic structure. For focusing the A_0 in a GRIN-PC, a refractive index profile was designed in the form of a hyperbolic secant:

$$n(y) = n_0 sech(\alpha y) \tag{4.3}$$

Where n_0 is the refractive index along the x-axis and α is the gradient coefficient.

The gradient coefficient was α = 6.65 x 105 μm^{-1} leading to the curve shown in Figure 4.8b. The radii of the holes were designed to make the effective refractive index distribution satisfy the hyperbolic secant curve for a frequency of 4 MHz. According to Figure 4.8b, the refractive index varies from 1.024 to 1.158, corresponding to a filling factor of 0.07 at the boundary and 0.503 at the centre respectively. To verify the focusing of the lowest antisymmetric Lamb wave (A_0) in the designed GRIN-PC lens, numerical simulations of the full plate were conducted. The result in Figure 4.8c shows focusing of the wave beam along the propagation direction.

4.3.3 Results and Discussion

To investigate the behaviour of the GRIN-PC lens, a series of chips were fabricated with an array of x=20a, 30a, 40a, 50a, 60a, enabling us to scan a cross-section directly next to the phononic crystals for the different sizes of array (which itself would not be possible within the lens due to the extremely small features). At a frequency of 4.5 MHz, the focusing behaviour was close to the simulation. As shown in Figure 4.9a, the normalized displacement across the chip shows a maximum displacement at the position y=0. This peak increases when increasing the array size until reaching a maximum between 50a and 60a, suggesting that the focal point is situated in this area. This was lower than the numerical model where the maximum amplitude appeared at x =62a for 4.5 MHz and the calculated focal distance by the ideal lens formula, $\pi/2\alpha$, giving x = 59a. The full half width maximum (FHWM) of the focused beam was of the order of 2a. The maximum amplitude observed with the GRIN-PC lens was 3 fold the amplitude observed in an unmodified silicon substrate, which was, again, in close agreement with the simulations.

It was also possible to observe a symmetry in the profile with respect to the centre at $y = 0$, showing the high quality of the fabricated lens. The wavy nature of the profile was observed both on the experimental and numerical results and could be explained by the scattering of the waves by the large holes (as the waves only propagate in the

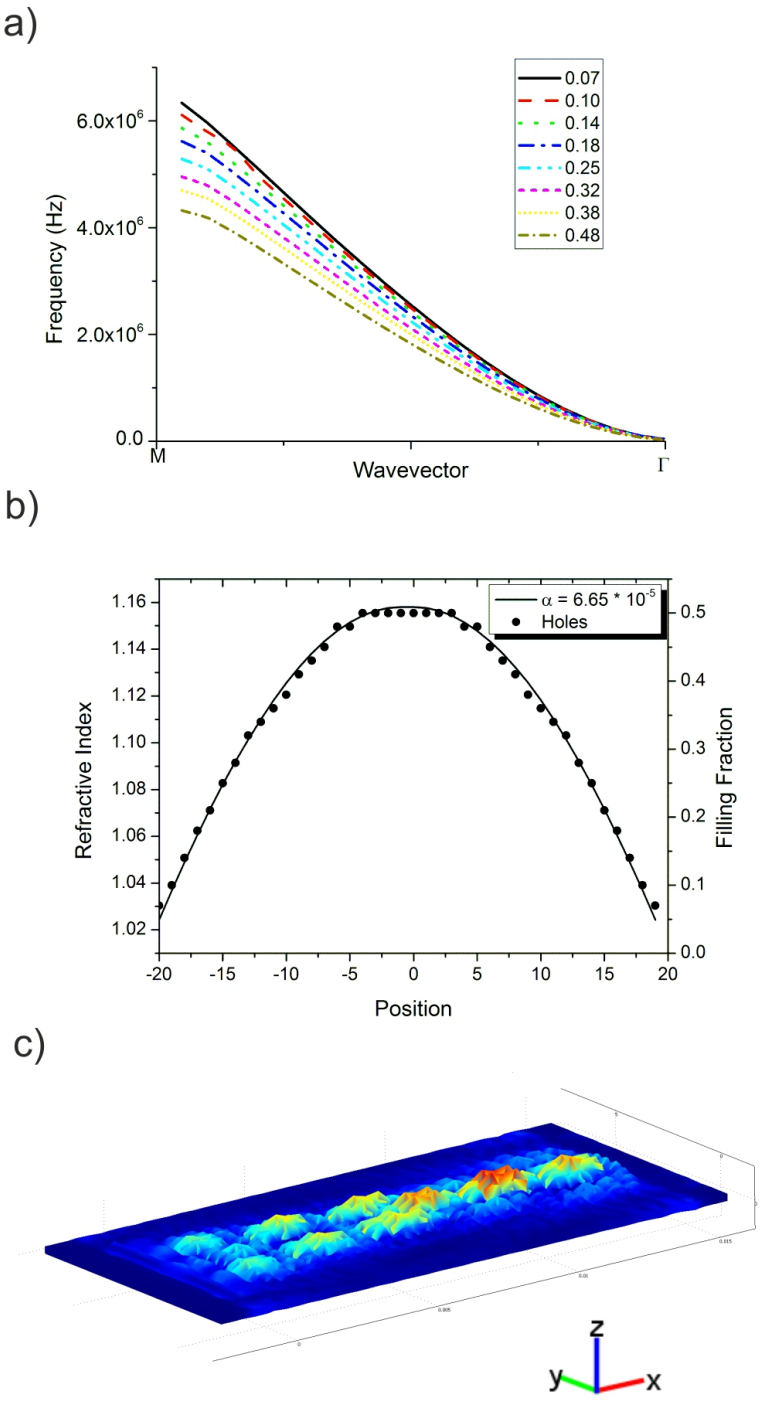

Figure 4.8: (a) Band structure of the A_0 mode of the phononic plate with different filling fractions. (b) Representation of the hyperbolic secant curve for $\alpha = 6.65 \times 10^{-5} \mu m^{-1}$ and the filling fraction of each phononic holes at its respective position. (c) 3D model of the propagation of the wave in the GRIN plate in x direction at 4 MHz.

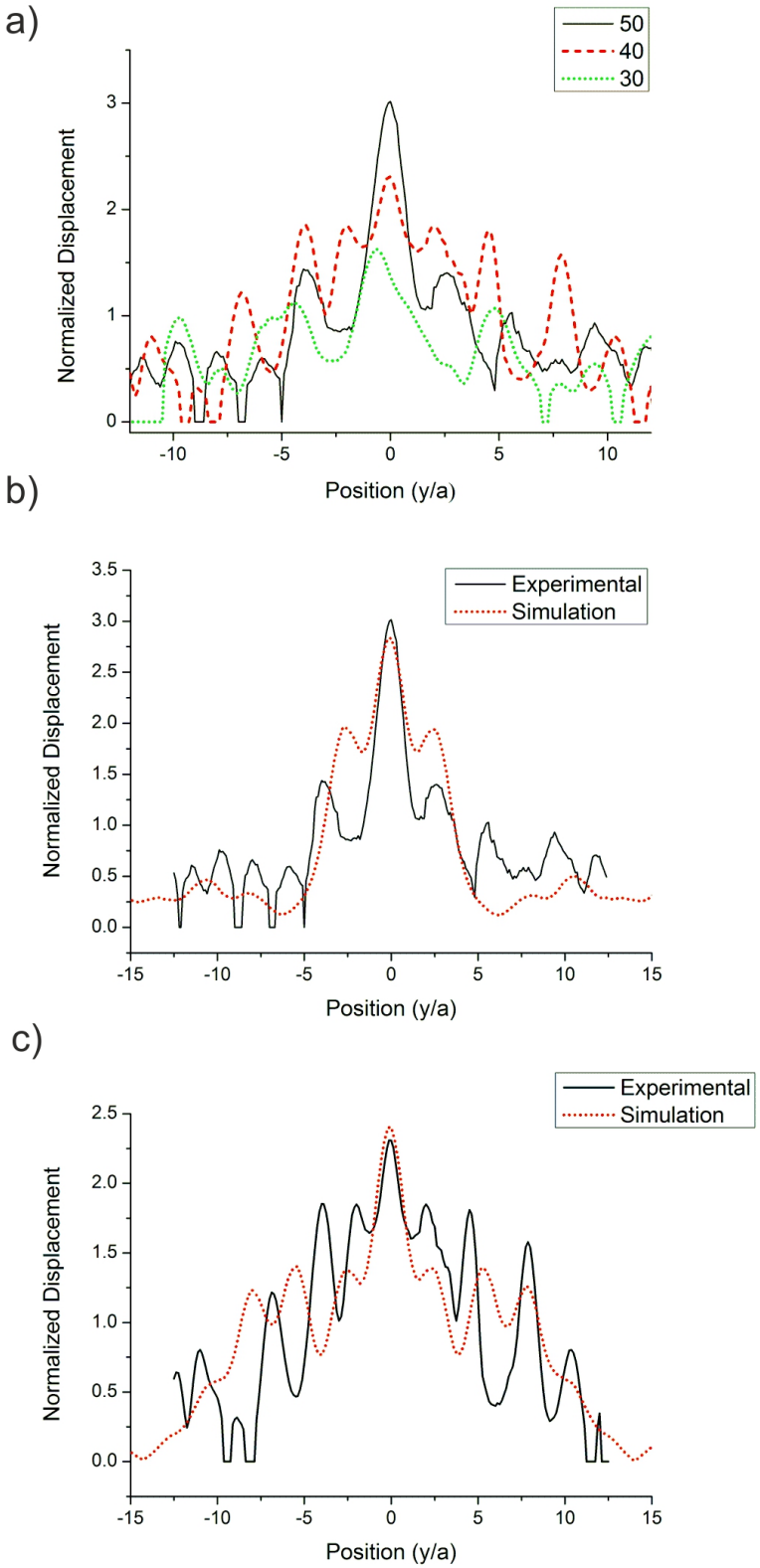

Figure 4.9: (a) Normalized displacement at position 30a, 40a and 50a for 4.5 MHz. (b) Comparision between experimental measurement and simulation at position 50a. (c) Comparison between experimental measurement and simulation at position 40a.

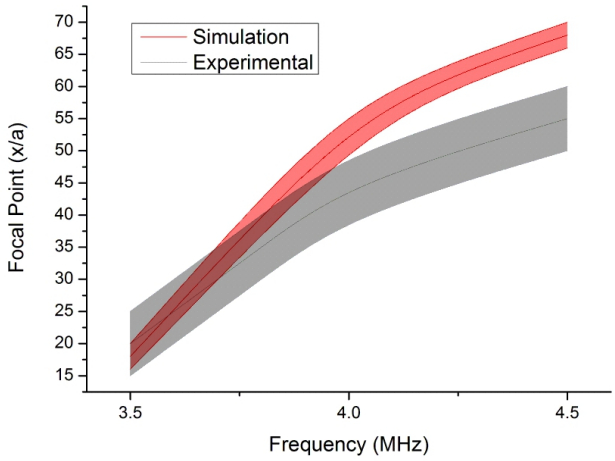

Figure 4.10: Focal distance as a function of the frequency for the experimental and numerical results.

solid material). The fabrication of phononic structures with a contrast in two solid materials could minimize this type of effect.

As the refractive index of the phononic crystal is dependent on the frequency used, the GRIN-PC lens was tested with a broader range of frequencies. As shown in Figure 4.10, the lens still showed focussing behaviour between 3.5 to 4.5 MHz. Both in experiments and simulations, a major effect observed is a shift in the focal length. As the acoustic frequency decreased, the focal length decreased (and vice versa, until reaching a threshold above 5 MHz where no focusing is observed). Looking at this band structure, it was possible to observe that, at this frequency range, the first antisymmetric mode cannot propagate anymore. The experimental and simulated results were in close agreement, although the focal length was shorter in the experimental results (it is possible that differences in the Youngs modulus and the quality of the meshing in the simulation could lead to such differences).

4.4 Conclusion

In this Chapter, the notion of shaping waves for microfluidics was introduced. This was performed by using specific designs of electrodes like the slanted IDT and by designing phononic structures in order to control the position of propagation of the waves or to focus energy. These techniques give an advantage over the use of standard IDTs as it is possible to program microfluidic functions in a frequency dependent manner. Moreover, it was shown that these techniques could be achieved also on a superstrate opening a clear road towards low-cost POC diagnostics.

A number of applications arised from this technique and are described in the following chapters. Here, a more specific conclusion is made for each technique.

4.4.1 Tuneable Surface Acoustic Waves

The use of a slanted IDT, in which the position of the excited SAW is dependent upon the input frequency, provides a method to design complex fluidic functions directly into a chip. The potential of this powerful tool to manipulate droplets and particles within them was demonstrated.

In contrast to other techniques, a clear advantage of this flexible method lies in its ability to induce streaming in a droplet in a chosen direction and at any position. Whilst other techniques are also restricted to the input power to control the concentration of particles, it was possible to perform this simply by shifting the position of the SAW, and hence its region of interaction with the droplet. More complex tasks were also performed, which were programmed sequentially into a single IDT device, where two droplets were moved, merged, mixed and centrifuged on a disposable superstrate. The aforementioned example shows the flexibility of the platform for basic fluidic operations needed in lab-on-a-chip technologies.

4.4.2 Stopband

Stopbands were successfully created on a disposable superstrate. This technique allows the manipulation of particle within a droplet in a tuneable manner and could achieve similar functions as described with the slanted IDT. It has advantages, especially in the field of POC diagnostics, as it gives a more versatile control directly on a dispoable chip and it is not constrained by the precise positioning of the disposable chip required in the slanted IDT method.

The results shown here have been used as a basis to build a device to sequentialy perform cell lysis and PCR using SAW for the diagnostics of malaria and has been published in PNAS [109].

4.4.3 GRIN Lens

The existence of focussing of surface waves in a GRIN-PC lens was demonstrated for the first time. The experimental results were in close agreement with the simulations and show that the GRIN lens can compress the acoustic waves with a focal length tuneable

by the frequency. This technique will find application in the field of acoustofluidics like the development of a SAW-based PCR where heat is generated by the high amplitude the SAW [109].

Chapter 5

Jetting and Swimming

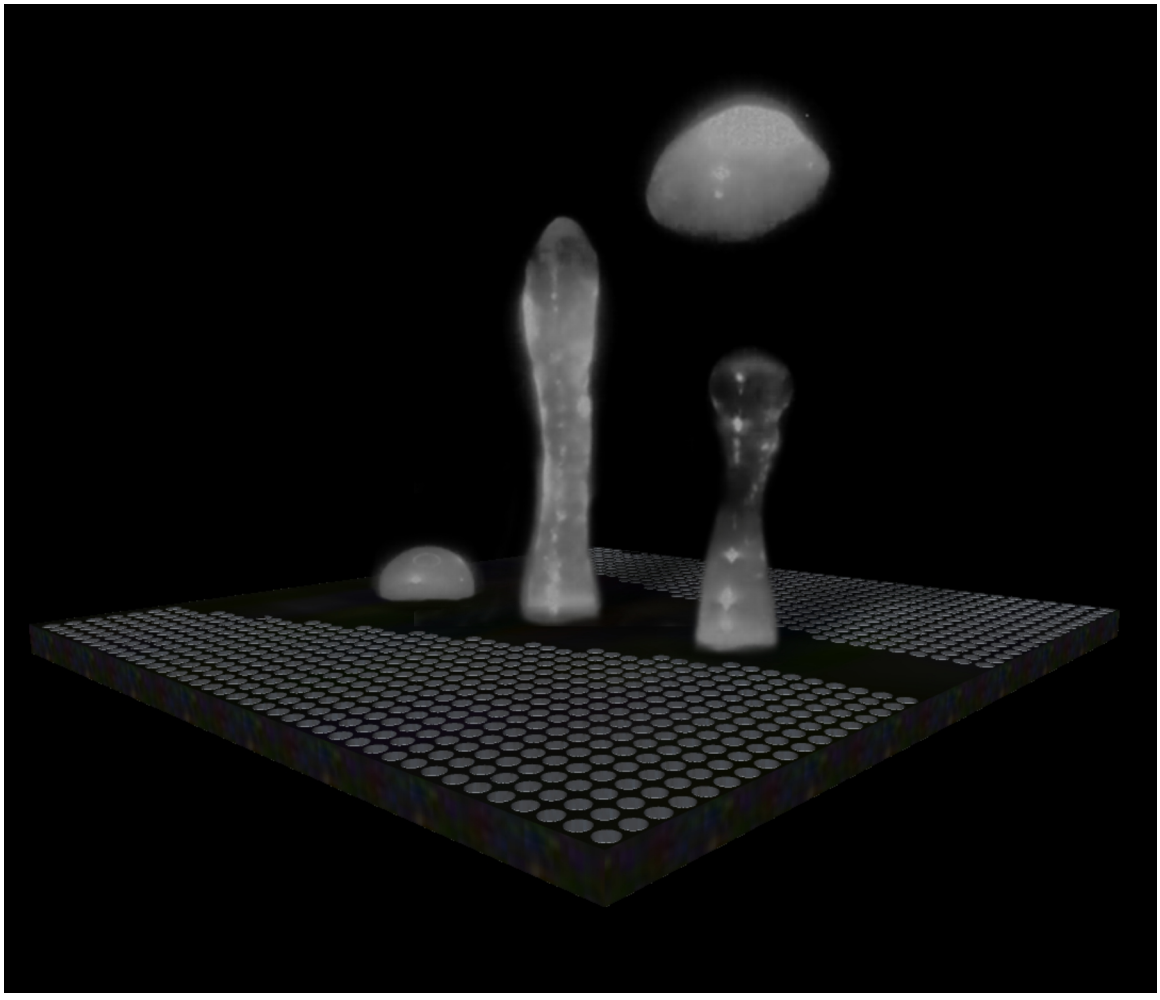

In this chapter, two applications arising from the ability to shape the acoustic waves are demonstrated. First, the surface waves are shaped in a phononic horn structure to control the direction and amplitude of a jet of water from a sessile drop. Then, a new method of propulsion using surface waves is demonstrated, where the direction of a vehicle is controlled by tuneable surface acoustic waves.

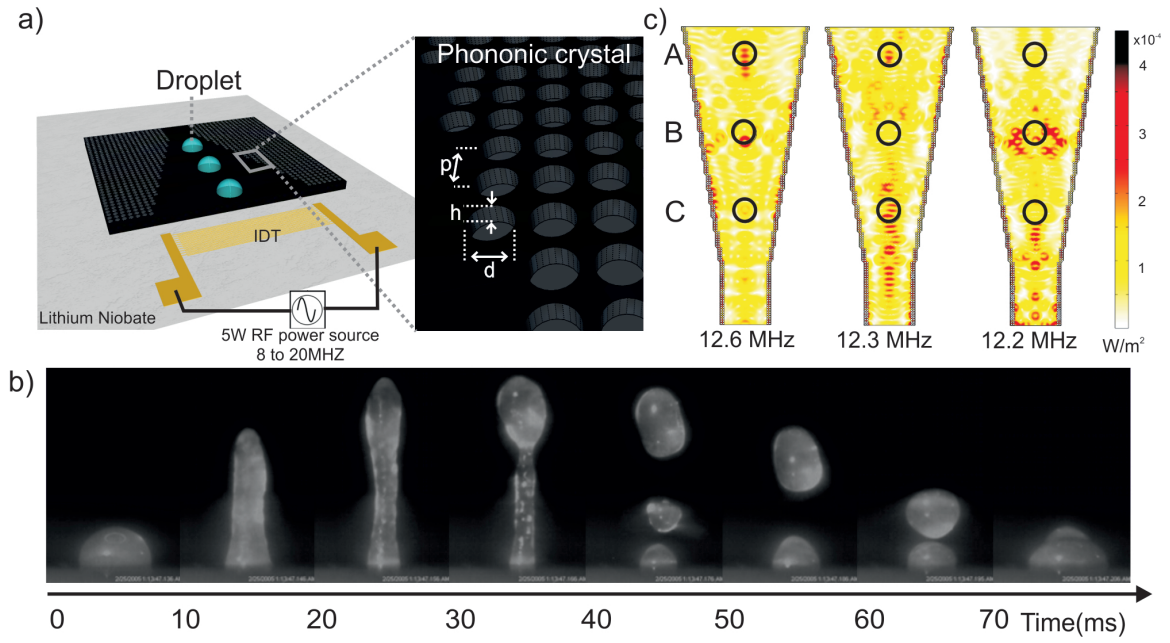

Figure 5.1: (a) Schematic of the device comprising an IDT on a $LiNbO_3$ wafer, the phononic crystal superstrate with the design of a conic structure, and three water droplets positioned on top of the non-piezoelectric superstrate. The expanded view on the right illustrates the phononic lattice etched in silicon where p is the pitch (200 μm), d the diameter (160 μm), and h the depth of the hole (235 μm). (b) Images captured from a movie taken at 1000 fps showing the jetting phenomenon induced by the acoustic waves on a phononic crystal superstrate for a droplet of 10 μL (2 W input power). The drop elongates to form a column of water and breaks up into multiple droplets. (c) Simulations of the conic structure at three different input frequencies. The waves are focused at different positions depending on the frequencies. The circles illustrate the positions of the droplets in the cone.

5.1 Jetting

In the previous chapter, it has been shown that by designing an appropriate phononic crystal lattice, stop-bands (or band gaps) can be engineered on non-piezoelectric materials, called superstrates, placed in contact with the piezoelectric substrate. It is now described how a cone shaped phononic crystal provides acoustic cavities, by focusing the energy at particular locations, Figure 5.1a, whose positions are determined by the frequency of the acoustic excitation and the intensity by the phononic crystal lattice. These parameters can be used to control and enhance locally the acoustic field.

Although, it has previously been reported that focused SAW can produce the interfacial jetting phenomenon on a piezoelectric wafer [135], here a phononic crystal is used to controllably direct jetting and eject droplets in a number of directions from a non-piezoelectric surface. With sufficient acoustic energy, the surface tension is overcome by inertia, leading to the pinch off of one or several smaller droplets (Figure 5.1b) due to the Rayleigh-Plateau instability [101, 107, 29].

5.1.1 Experimental

SAW device

The SAW device was fabricated on a 128° Y-cut X-propagating 3 inch $LiNbO_3$ wafer ($c_R = 3996$ ms^{-1}) using the method described in Chapter 3.1.2. It consisted of 20 pairs of 160±7.5 μm width electrodes with a pitch of D = 320 μm and a 10 mm aperture. According to Equation 2.9, the SAW could be generated for frequencies f = 6.25±0.3 MHz or f = 12.5±0.6 MHz using a harmonic mode.

An Agilent Technologies MXG Analog Signal Generator N5181A was used in conjunction with a Mini Circuits ZHL-5W-1, 5-500 MHz amplifier and a 3 A, ±24 V DC power supply to control the SAW device. The SAWs, generated on the $LiNbO_3$ wafer, were coupled into a superstrate placed on its surface, exciting Lamb waves.

Phononic crystal

The phononic crystal was fabricated using a <100>silicon wafer with a thickness of 470 μm. The pattern (designed by Dr. Rab Wilson, Division of Biomedical Engineering, University of Glasgow) comprised of a square array of disks of diameter d = 160 μm and with a pitch p = 200 μm, to provide a fill fraction, ff, ($\pi r^2/p^2$) of ∼0.5. The aperture for the cone was 10 mm to coincide with the aperture of the IDT and the apex was approximately 3 mm wide. The pattern was transferred into a 4 inch <100>silicon using dry etch (STS ICP) to a depth of half the thickness of the wafer (235 μm) using the method described in Chapter 3.1.3. The wafer was cleaned in acetone and cleaved to provide the individual superstrates (20 mm by 30 mm). The chips were then silanized in order to create a hydrophobic surface using the method described in Chapter 3.1.4 for a contact angle of 101°.

Jetting measurement

A 10 μl volume of DI water was placed between the superstrate and the substrate, to provide a layer approximately 10 μm thick, to promote acoustic coupling. The jetting phenomenon was recorded using a Photron XLR fast camera at 1000 fps. The images were then analyzed with ImageJ software.

Simulation

The modeling software, COMSOL Multiphysics v3.5a ®based on the Finite Element (FE) method, was used to analyze the spatial acoustic intensity of the 2D silicon

phononic crystal with circular holes. The software provides equation-based multi-physics modeling that allowed the simulation of the acoustic-structure interactions of the 2D phononic crystal. In the numerical simulation, the density of single-crystalline silicon was set to 2.33 x 10^3 kgm^{-3}, and the phase velocity for the lowest order modes of Lamb waves (A_o) in silicon was 4560 m s^{-1} [147]; while, the density of air at 20 °C was 1.25 kg m^{-3}, and the longitudinal velocity of sound in air was 343 m s^{-1}. The lattice parameter of the phononic array matched the design of the superstrate (p = 200 μm, d = 160 μm). A plane wave was generated into the 2D phononic crystal (radiation boundary condition).

5.1.2 Results and Discussion

Simulations (Figure 5.1c) confirmed that the spatial variation in acoustic intensities (shown in W m^{-2}) differs when the acoustic waves were generated at different frequencies (12.6 MHz, 12.3 MHz or 12.2 MHz, here). When considering three droplets placed on positions A-C on the superstrate, it can be seen that the maximum intensity for 12.6 MHz occurs at the position of the droplet A, while for 12.2 MHz it is at position B.

For a droplet of DI water, the Rayleigh angle (Equation 2.12) was $\theta_{Rayleigh} \approx 19°$ on the silicon superstrate (c_s= 4560 ms^{-1}). The resulting leaky acoustic waves generated acoustic streaming within the droplet. The difference in acoustic impedance between water (Z_1=1.483 x 10^6 Nsm^{-3}) and air (Z_2 = 410 Nsm^{-3}) made the wall of the droplet reflective (with a reflection coefficient $R = \frac{Z_1 - Z_2}{Z_1 + Z_2} = 0.99$).

In these experiments, the droplets with a radius, R_d, of 1 to 5 mm, were much larger than the acoustic wavelength, 320 μm. When a low power wave was produced, weak streaming occured and the Reynolds number, Re, can be estimated as Re<1, where $Re = \rho U_s R_d/\mu$ in which U_s is the streaming velocity, ρ the liquid density and μ its viscosity. For higher powers, $Re \sim 10^3$, the capillary stresses acting on the interface of the liquid meniscus were overcome by inertia and the droplet deformed into a column of water, as seen in Figure 5.1b.

Figure 5.2a shows that, for a jet from a sessile drop on a silicon superstrate using Lamb waves, the jet length, defined as the maximum height that the droplet achieves before pinching off, is proportional to the input power. The jet length increased linearly, up to 1 cm for a 10 μl drop, until reaching a threshold where the column pinches off into one or several droplets. This breaking phenomenon is characterized by the Weber

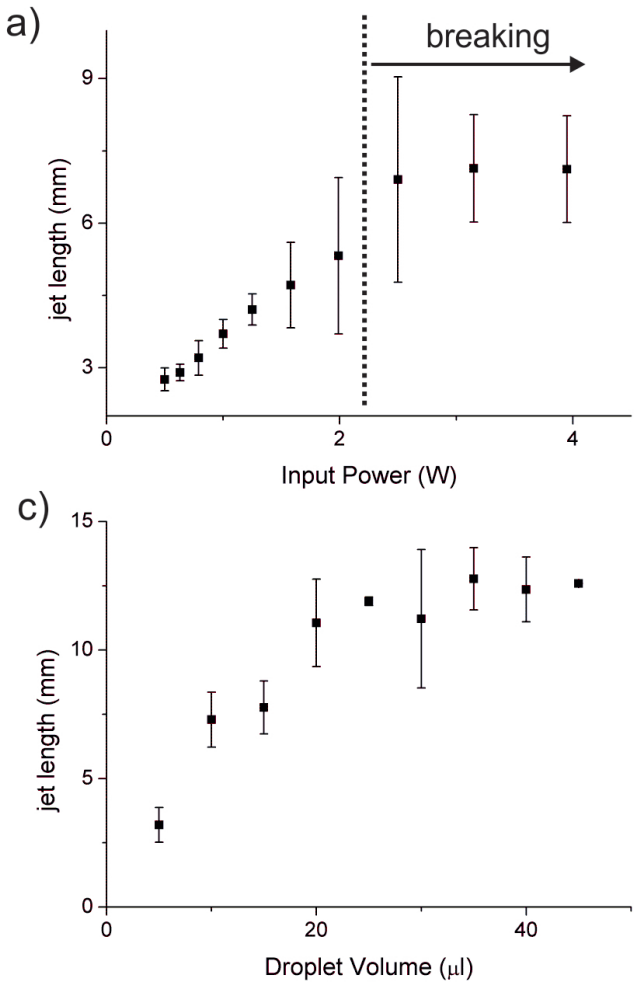

Figure 5.2: (a) Jet length (before breaking up) as a function of the input power for a 10 μl droplet of DI water; (b) Jet length as a function of the droplet volume for a fixed input power (2 W).

number

$$We = \frac{\rho U_j^2 R_j}{\gamma}, \tag{5.1}$$

where U_j is the velocity of the jet, R_j the radius of the jet and γ the surface tension [135].

The jetting phenomenon itself is characterized by the interplay between acoustically-driven inertia, the force due to the surface tension and gravity. Figure 5.2b shows that for a fixed input power, the jet length increased with droplet volume, until reaching a maximum. This plateau can be explained by the fact that the increase in acoustic energy, coming from the increased surface of contact when the volume increases, was not sufficient to overcome the increase in surface tension and the gravity.

The ability to focus the acoustic energy to shape the fluid lies within the design of the phononic crystal horn structure, which creates regions of enhanced acoustic field intensity. Energy localization and intensity can be tuned by the input frequency with respect to the geometry of the phononic crystal (Figure 5.1c). Three droplets positioned on three different locations in the horn were subjected to different field intensities. As predicted, Figure 3a shows that the jet length of a 10 μl droplet was highly dependent upon its position on the chip. For example, for an input frequency of 12.1 MHz, the jet was higher for the droplet at position B, which was the point with the highest intensity. Consequently, the placement of the droplet within the local wavefield, formed by the phononic crystal structure enabled the control of the way the energy was imparted to the drop, and subsequently, its jetting behavior.

In contrast, for a plain (non-phononic) superstrate, the jet length remained equal at any position of the droplet, as the intensity of the acoustic field was homogeneously distributed on the surface. Thus, when using the simulations to compare the differences between the acoustic fields within the phononic lattice and the plain silicon superstrate, the maximum intensity within the phononic horn can be predicted to be $\sim$6x the intensity on an unmodified superstrate, for a fixed input power (Figure 5.3b). The ability to focus energy at a particular position on the phononic superstrate was confirmed experimentally, with a similar ratio ($\sim$5x) for a droplet at position B, as shown in Figure 3a. Lower jet lengths on the phononic superstrate compared to the bare superstrate were also observed and suggested that regions of low intensities can also be designed using these phononic crystals.

The model also showed that the spatial distribution of the acoustic field intensity

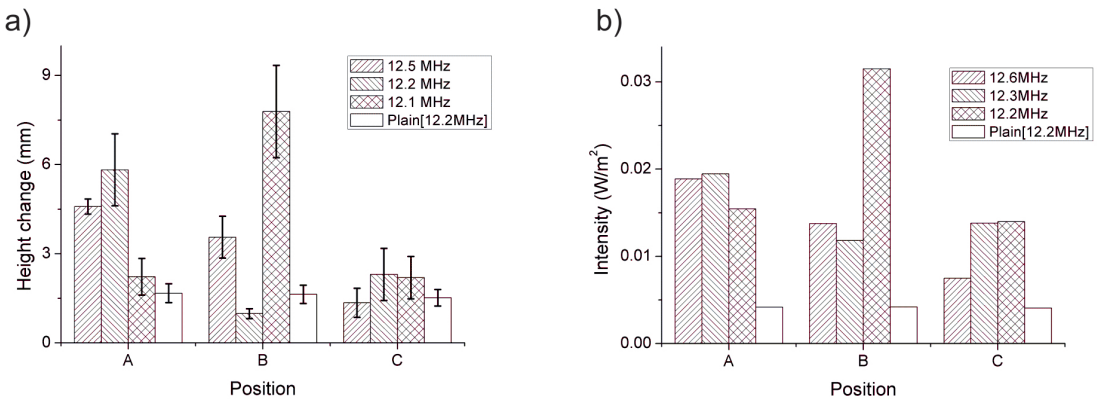

Figure 5.3: Spatial control of jetting by the phononic lattice. (a) Experimental height change as a function of the position of the 10 μL droplets in the cavities of the phononic crystal superstrate (as described in Figure 5.1) for three input frequencies and on a plain (non-phononic) superstrate. (b) Acoustic intensity (Wm^{-2}) extracted from the model as a function of the position of the droplets in the horn structure (as described in Figure 5.1) for three input frequencies and on a plain (non-phononic) structure. The differences between the modeled and the actual operating frequencies were linked to tolerances in fabrication of the phononic superstrate.

changes when the input frequency was tuned. Experimentally, this can be seen in Figure 5.3, where, for an input frequency of 12.5 MHz, the highest jet length was observed at position C, while it was at position B when the frequency was switched to 12.1 MHz.

The spatial control of the acoustic field was further used to control the direction of the jetting. Unlike the jet formation occurring when applying a propagating wave, where the angle of the jet was equal to the Rayleigh angle, here the angle is a result of the propagating and scattered or reflected waves from the phononic lattice. The direction of the jetting was dictated by the resultant force associated with the acoustic waves $\vec{F}_{AW}$ and gravity $\vec{F}_g$.

It was observed that, depending on its position, the drop could either jet perpendicularly from the surface, Figure 5.1a, in the same direction as the wave propagating away from the source, Figure 4a-b, or in the opposite direction, Figure 4c. In the specific design of the horn, acoustic waves were scattered or reflected back, and focused by the phononic lattice. Consequently, the intensity profile of the acoustic field varied depending on the position in the cone structure and the frequency of the waves. Using a Huygens principle-like approach [35], the acoustic waves can be considered as a source of secondary wavelets propagating in the fluid in all directions. As the force arising from the propagation of the wave in the fluid is proportional to the amplitude of the wave, each wavelet will create forces proportional to its amplitude. By summing the forces of each wavelet, the resulting force $\vec{F}_{AW}$ has a direction and amplitude that will

depend on the intensity profile of the acoustic wave.

Figure 5.4 shows simulations of the propagation of the acoustic wave in the fluid, based on such a decomposition. When the drop was symmetrically positioned on a region of high acoustic intensities, the resulting force $\vec{F}_{AW}$ was directed perpendicular to the surface and the droplet jets in a direction perpendicular to the surface (Figure 5.1a). When the drop was asymmetrically positioned on a region of high acoustic intensities, the resulting force $\vec{F}_{AW}$ was oriented with an angle different from the Rayleigh angle. For a jet perpendicular to the surface, the gravity was directed in the opposite direction of the resulting acoustic force and had no impact on the direction. For a non-symmetrical position, the gravity can contribute to increase the angle as the center of mass was displaced. Thus, it was possible to control the direction of the resulting force $\vec{F}_R$ and consequently jet the drop with a chosen angle in a direction similar to the propagation of the SAW (Figure 5.5 a-b) or even in a direction opposite to the SAW propagation, as shown in Figure 5.5c.

5.2 Swimming

Recent interest in microactuation of free standing objects in fluids arises from their potential applications in the military, aeronautic and biomedical fields. For example, small exploratory aquatic vehicles may be used for exploration, whilst swimming microrobots have been proposed for minimally invasive surgery and endoscopy [141]. Such propulsion technologies generally use rotary propellers actuated using either electrostatic [132], electromagnetic [53], piezoelectric [141], osmostic [128] or thermal [124] driving forces. In such cases the miniaturization of the propulsion system is complex and technologically challenging, especially when there is a requirement for precise control of power and direction. Further physical scaling laws, associated with friction, heat generation and dissipation also hinder the design of micromachines, an issue which is compounded by the dominance of the fluid viscosity at low Reynolds numbers (characteristic of microflows). These issues, when combined with other constraining issues, including biofouling and entanglement of debris, have restricted the practical application of these motors.

A SAW propulsion system with no moving parts, based upon acoustic streaming is demonstrated here for the first time. This new, low cost SAW device differs from ultrasonic thrusters (UST) in its high efficiency in operation and its ease of fabrication

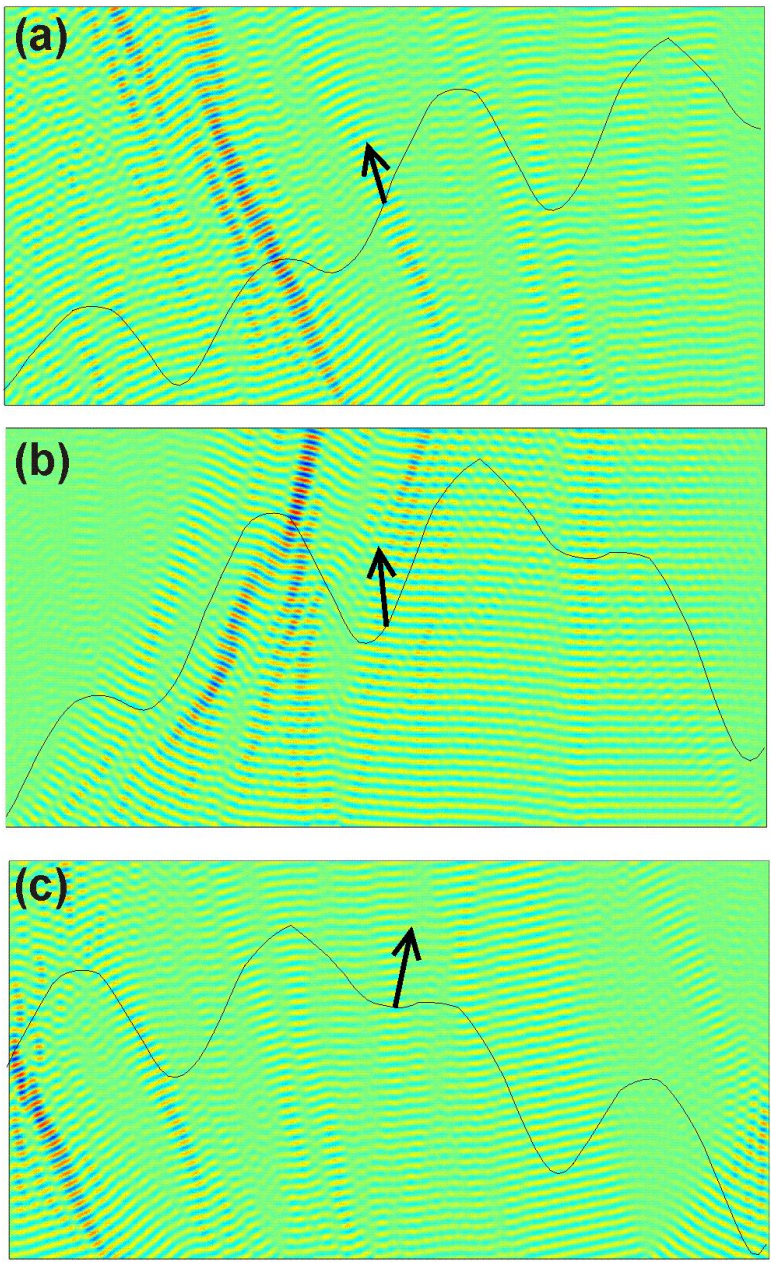

Figure 5.4: The modeling software (COMSOL Multiphysics v3.5a ®) based on the FE method, was used to analyse the spatial acoustic intensity in the fluid. The data of the acoustic field intensity profile (represented as a line) on the phononic superstrate were extracted from the simulation in Figure 5.1 c and were added in this model as a series of points propagating waves in all directions. For the left and right walls, acoustic hard boundary conditions were used, while, for the top, a radiation condition was used. The direction of the resulting force is represented by the arrow.

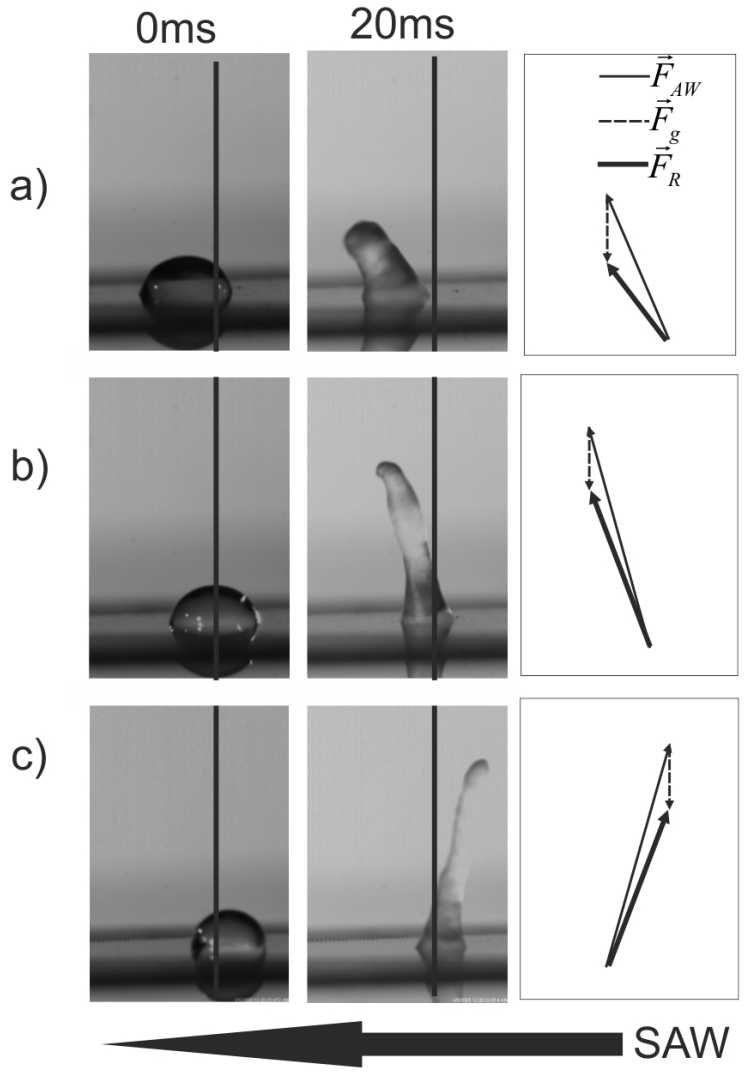

Figure 5.5: (a) Experimental image of the jetting of a droplet of 15 μl in the same direction as the propagation of SAW, shown as a black arrow at the bottom of the figure. The right images are schematics, illustrating the direction and amplitude of the forces encountered and the resulting forces for each droplet position; (b) The same droplet shifted on the right. The jetting was still in the same direction as the SAW propagation, but the amplitude is larger and the angle smaller; (c) The same droplet shifted further to the right. The jetting was in the opposite direction to the SAW propagation. The vertical black line serves as a visual aid.

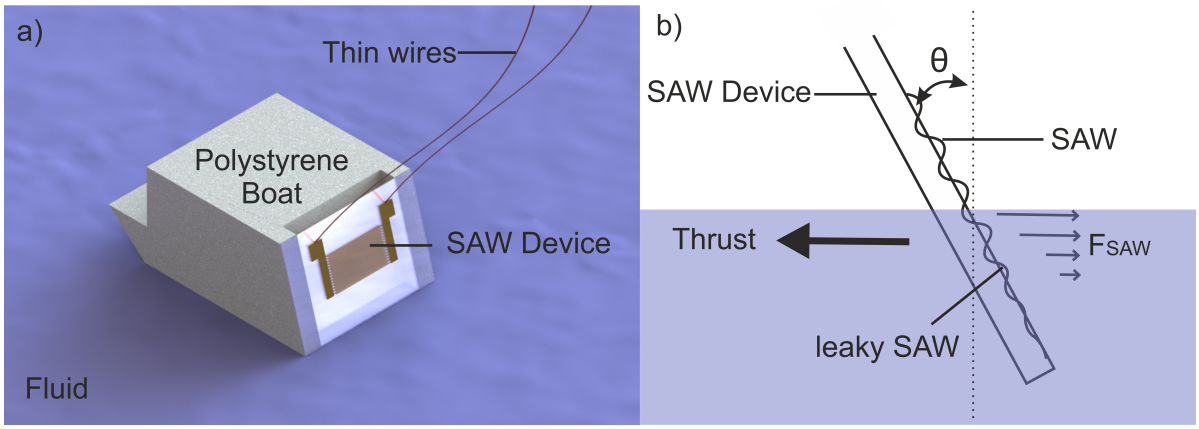

Figure 5.6: (a) Illustration of the vehicle, the SAW device is positioned at the back. (b) Schematic of the physical principle. The SAW propagates along the surface and refracts into the water producing a force (F_{SAW}) and a thrust in the opposite direction.

[52, 2, 133]. The application of this technique was demonstrated by propelling a millimetre scale vessel illustrated in Figure 5.6a. The high frequency ultrasonic wave was attenuated in the liquid providing silent propulsion. A frequency dependent control of the direction of travel was achieved using a tuneable surface acoustic waves device [11]. The SAW device with its active surface also had an intrinsic ability to reduce biofouling which would be a major advantage compared to rotary propellers [116, 12].

5.2.1 Theory

The motor was immersed into a liquid and an acoustic wave was generated which propagates into the fluid. The acoustic waves were partially absorbed, resulting in a decrease in the mean momentum flux as the waves travel through the fluid. A net force is associated with this decrease in the momentum flux.

The equations governing surface acoustic streaming have already been explored in Section 2.3. In this particular case, the acoustic Reynolds number ($Re_A = \rho_F \nu_1 \lambda_F / 2\pi\mu$), where ρ_F, ν_1, λ_F, μ, are respectively the fluid density, particle velocity, wavelength in the fluid and dynamic viscosity) range from 0.02 to 2, the particle velocity v_1 from 0.01 to 1 m s^{-1} and fluid velocity from 0.1 to 10 mm s^{-1}. Re_A being smaller than 1 in most of the cases and the particle velocity being much higher than the fluid velocity, here the assumption was made that the streaming is slow and use Nyborg's equations to describe the force arising from the SAW streaming. The equations in the theory Section 2.3 are used.

SAW becomes a leaky SAW when in contact with a fluid as shown in Figure 5.6b. Under these conditions the SAW is refracted into the liquid with an attenuation length

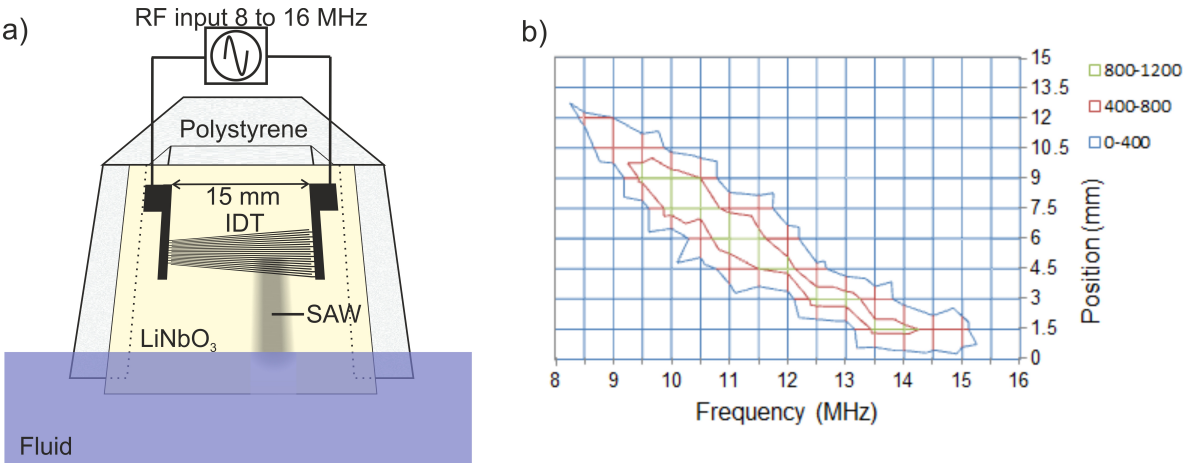

Figure 5.7: (a) Schematic of the vehicle (back view). A sinusoidal electric signal was applied to the IDT on a piezoelectric substrate to generate the surface waves, which propagate along the surface into the fluid. The SAW device was in contact with the polystyrene structure on a rail. (b) View of the surface displacement of the acoustic waves on the $LiNbO_3$ wafer as a function of the input frequency and the position along the fingers for a slanted IDT, shown in Figure 2(a). The legend is the displacement in pm. The effective aperture of the wave beam was consistently around 2 mm. Additional sidebands expected for a tapered interdigitated transducer are not visible as their amplitudes are lower than 400 pm.

of the surface wave, given by Equation 2.11, of 4 mm (F = 11.83 MHz).

The waves are refracted into the liquid as a longitudinal wave at the Rayleigh angle (Equation 2.12) of 23°.

The force arising from the SAW streaming is described by (Equation 2.16) [122]:

$$F_{SAW} = -\rho_0(1+\alpha_l^2)^{3/2}A^2\omega^2 k_i e^{2(k_i x+\alpha_l k_i z)} \tag{5.2}$$

Where $\alpha = j\alpha_l, k_L = k_r + jk_i$

This force is directed at the Rayleigh angle [122] and can be used to drive a vehicle in water.

5.2.2 Experimental

The vehicle consisted of a floating craft made in expanded polystyrene (length = 50 mm, width = 35 mm, height = 30 mm, weight = 4.3×10^{-3} kg) as shown in Figure 5.6 or a rubber duck (length = 55 mm, width = 50 mm, height = 40 mm, weight = 16.3×10^{-3} kg). The SAW device was fixed at the back for propulsion. Two different designs of IDT were used, including a standard IDT (Figure 5.6) and a slanted (or tapered) IDT (Figure 5.7). The SAW device was produced using methods described in Section 3.1.2.

The SAW device was fixed to the craft with an angle of 23° with respect to the vertical in order that the waves refracting into the fluid at the Rayleigh angle of 23° propagate parallel to the surface of the fluid. The immersion of the device was 4 mm, which was the calculated length attenuation, to provide a maximal thrust efficiency as shown in Figure 5.6a-b and 5.7a.

Videos were collected and analysed using ImageJ to extract information concerning the velocity and the ability to control direction. The velocity profiles were further analysed to calculate the drag force and the thrust of the boat. The thrust was measured as a function of the acoustic power for the standard IDT oriented at 23° and is shown in Figure 5.8. The power of the SAW was determined by calculating the transmission coefficients of the IDT and the acoustic wave along its path. The voltage standing wave ratio (VSWR) of the IDT at 11.83 MHz was 2.228 VSWR, leading to a mismatch loss of 0.72 dB. However, the SAW was excited in two directions on the substrate, leading to an additional reduction of the actuating power by -3 dB, since only one was transmitted into the water. Thus the acoustic power can be calculated as the electric power attenuated by 3.72 dB, since the SAW is then completely refracted into the liquid with an attenuation length of the surface wave of 4 mm according to Equation 2.11 for a frequency of 11.83 MHz.

5.2.3 Results and Discussion

The force was obtained by estimating the drag coefficient of the vessel and measuring the maximal speed as a function of input power. Since the thrust and the drag force are equal when the speed remains constant, by measuring the drag force, the thrust can be calculated. As shown in Figure 5.8a, the force was linear with the acoustic power, generating 8 mN for an input power of 1.7 W, which is 10 times more efficient than plane waves ultrasonic thrusters [2, 133].

The orientation of the SAW device had an impact on the thrust. From the theory, it is known that the SAW refracts at the Rayleigh angle and thus the force arising from the SAW is directed at this angle. To verify this, the vessels was propelled by orienting the SAW device with different angles, θ with respect to the vertical (30°, 23°, 0° and -30°). As expected, at 23° orientation, the vessel accelerated at the highest rate, to the highest velocity (confirming that the Rayleigh angle is the most efficient coupling, notwithstanding the difference of drag force due to the variation in the design).

As stated previously, the SAW was transmitted into the fluid with an attenuation

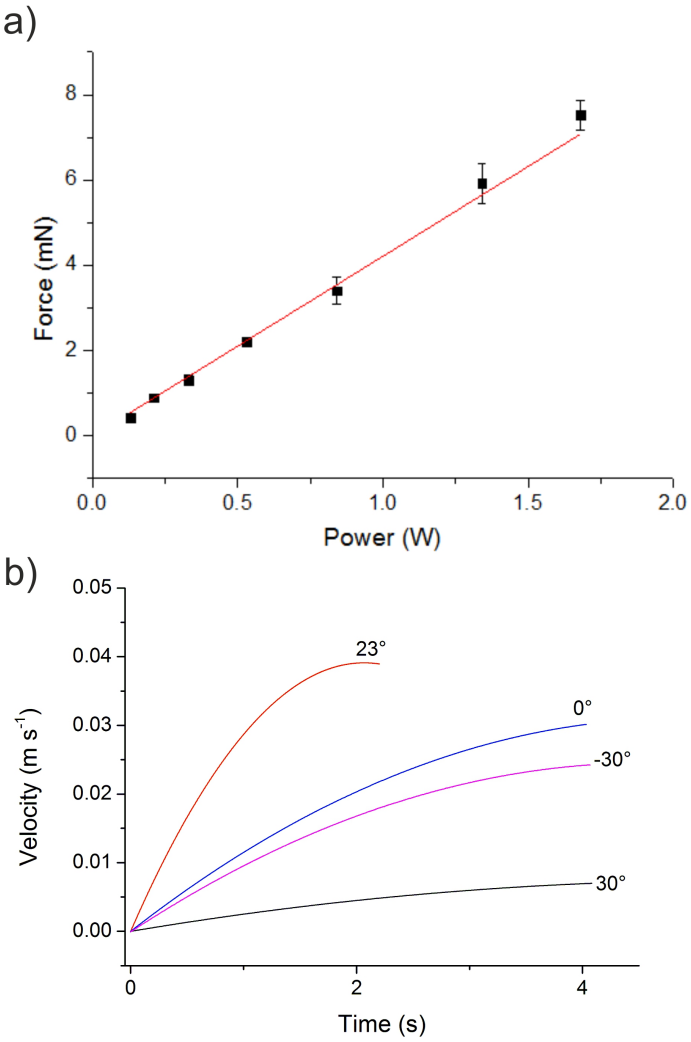

Figure 5.8: (a) Thrust force produced as a function of the acoustic power. (F = 11.83 MHz). Error bars are standard deviations (n=5). (b) Velocity profile of the vessel during acceleration from stationary to its maximum velocity with the SAW device oriented at different angles (F = 11.83 MHz, power = 1.4 W). The maximum velocity was reached by the device at 23°.

length of 4 mm, thus the immersion depth of the device above this length had an insignificant effect on the thrust. However a minimal immersion depth is preferred to reduce the drag force as much as possible. This could be achieved by increasing the frequency. Several immersion depths were tested and it was found that it was possible to propel the boat with depth lower than 1 mm. Due to the design of the boat, no significant differences in the maximum speed were found between depths from 1 mm to 4 mm. Above 4 mm, the maximum speed started to decrease due to the increase of the drag force.

To illustrate the control of direction using the tuneable acoustic wave technique, the SAW device was placed in the vessel. The directional control relied on the ability of the tapered IDT to generate the wave at different positions along the aperture, with the

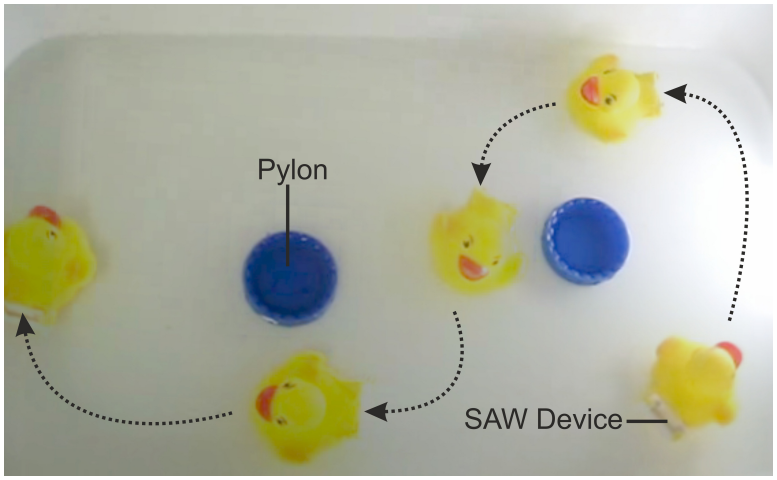

Figure 5.9: Direction control using tuneable surface acoustic waves. The image is a superposition of still from a movie every 3 s. A frequency of 13.2 MHz is used to turn right and 9.2 MHz to turn left. A duck is used here for aesthetic purposes.

force propagating from the SAW being generated on the side of the device and creating a torque. As shown in Figure 5.9, both left turn and right turn were performed using frequencies of 9.2 MHz and 13.2 MHz, respectively. The torque (θ) was measured by first estimating the moment of inertia (I) of the rubber duck by considering it as an ellipsoid ($I = m(a^2 + b^2)/5$) and measured the angular acceleration (α) from the videos. As $\theta = I\alpha$, it was possible to estimate that torque in the order of 10 nNm for a frequency of 13.2 MHz and power of 1.4 W.

Finally, the heating of the device was investigated using a thermal camera. The vessel was maintained immobile in the water while images of the device were recorded with a thermal camera for different input powers. The temperature of the piezoelectric material increased only by 3 °C on the side of the device in contact with the water for an electrical input power of 4 W, while it increased by ∼15 °C on the upper side, as shown in Figure 5.10. This can be explained by the fact that the energy was fully transmitted into the fluid on the lower side. To overcome the heating on the upper side, a single phase unidirectional transducer (SPUDT) could be used, which, in turn, could also increase the efficiency of the device.

Previously, it has been proposed that the single cell micro-organism cyanobacteria are using waves travelling along its outer cell membrane as a surface wave, thereby providing a method of propulsion without flagella [31]. As the waves propagate along the cell membrane, they induce a streaming in the surrounding liquid and generate a force [30]. Although these waves probably move at a slower speed and have a larger z-displacement than the piezoelectric SAW, the mechanism of a propulsion system based upon generating acoustic streaming, is an interesting analogy.

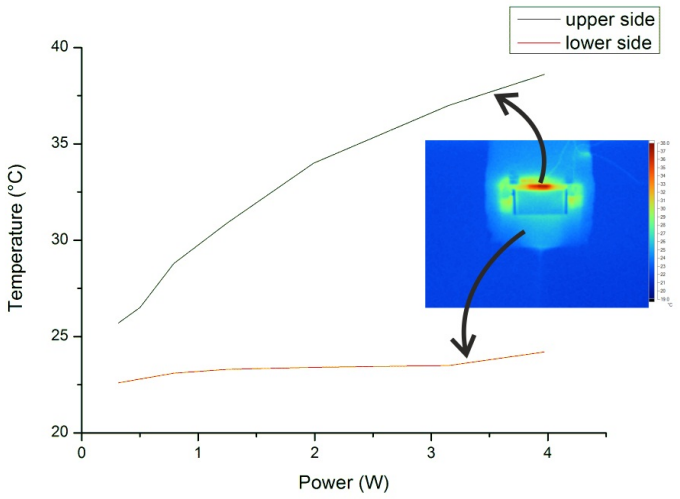

Figure 5.10: Temperature of the SAW Device after 1 minute as a function of the input electrical power.

5.3 Conclusion

In this Chapter, the ability of shaping the waves using tuneable SAW or phononic crystals to manipulate fluidic systems was demonstrated. It allowed jetting and the propulsion of a craft with control on the direction. Although these two applications are not likely to be used in the field of diagnostics, they show the power and the potential of such techniques. More specific conclusions are made below.

5.3.1 Jetting

Phononic crystal structures were engineered to control the location and enhance the intensity of the acoustic energy in a tunable manner on a non-piezoelectric substrate, enabling the development of advanced microfluidic functions. The enhancement of the acoustic intensity was such that it provided the ability to create interfacial jetting of a sessile drop of high amplitudes on a non-piezoelectric superstrate using only a single interdigitated transducer. The particular profile of the acoustic field also enabled us to shape the elongated jet in directions independent of the Rayleigh angle, in a manner that has the potential to enable directional non-contact droplet dispensing.

5.3.2 Swimming

A propulsion system based on SAW streaming is demonstrated for the first time. This technique is low cost and easy to fabricate, allowing for propulsion without any moving parts. Control of direction is inherent to the design of the device, if a slanted IDT is

used. Moreover, the SAW device could be scalable from millimetre size down to micrometre by scaling the electrode spacing down to 2 μm for example, and increasing the frequency to 2 GHz, using state of the art of fabrication techniques. This new technique will not only find applications in biomedical and aeronautic fields but should also find interest in fundamental biophysical research on the propulsion of microorganisms.

Chapter 6

Integrated Immunoassay

In this Chapter, an immunoassay based on the manipulation of beads using tuneable SAW and lensfree detection for the diagnostics of TB is demonstrated. After a short introduction, the principle of the tuneable SAW immunoassay is described and results for both microscope-based and lensfree detection are presented.

6.1 Introduction

In the previous Chapter, a new technique based upon a tuneable SAW on a slanted (or tapered) IDT was reported [11]. Using this particular type of IDT, it was possible to control the position and the acoustic aperture of the generated SAW in a frequency dependent manner, thereby achieving combinations of droplet movement, merging, mixing and particle concentration, using a single IDT. These functions were advantageously performed on a disposable superstrate[11, 51].

Other techniques that have been demonstrated using SAW include overcoming diffusion limitation and enhancing mass transfer rates by SAW-induced convective streaming [38]. It has also been shown that SAW can not only mitigate against non-specific binding of proteins on the piezoelectric surface[24, 116, 117] but can also be combined with enhanced mass transfer in the same device. [110] One potential drawback of SAW, however, is that it can create analytical noise through the injection of heat into the fluid.

Here, an integrated immunoassay on a disposable chip using tuneable SAWs was developed. The immunoassay was based on the manipulation and detection of beads in a microlitre droplet on a planar surface for the analysis of interferon-γ, a biomarker used in the diagnosis of tuberculosis [96]. The control of particles using SAW allowed full integration of all the immunoassay process steps, enhancing the overall speed of the assay and reducing the non-specific binding of the carrier beads. A lensfree technique allowing the detection of single beads near the surface of a charged-coupled device (CCD) or a complementary metal- oxide-semiconductor (CMOS) camera of a standard mobile phone was used as a detection method [84, 94, 119, 137] and was compared to a microscopy method.

6.2 Experimental

6.2.1 Tuneable SAW immunoassay

The experimental set-up comprised a slanted IDT on a lithium niobate wafer (Figure 6.1a-b), where the position of the generated waves was controlled by the input frequency. The acoustic waves were coupled into a disposable chip, called a superstrate, through a thin layer of 2 μl KY jelly (Johnson & Johnson). Only a small part of the chip was in contact with the substrate, the free space under the coverslip allowing optical detection (Figure 6.1a-b).

SAW device

The SAW device was fabricated on a 128° Y-cut X-propagating 3 inch $LiNbO_3$ wafer and consisted of 10 pairs of tapered electrodes to form an interdigitated transducer (IDT). The pitch and the width of the electrodes varied linearly from 62.5 μm to 125 μm along the aperture. The SAW device was fabricated according to the method reported in Section 3.1.2. The wafer was fixed on a heat sink to avoid heating of the

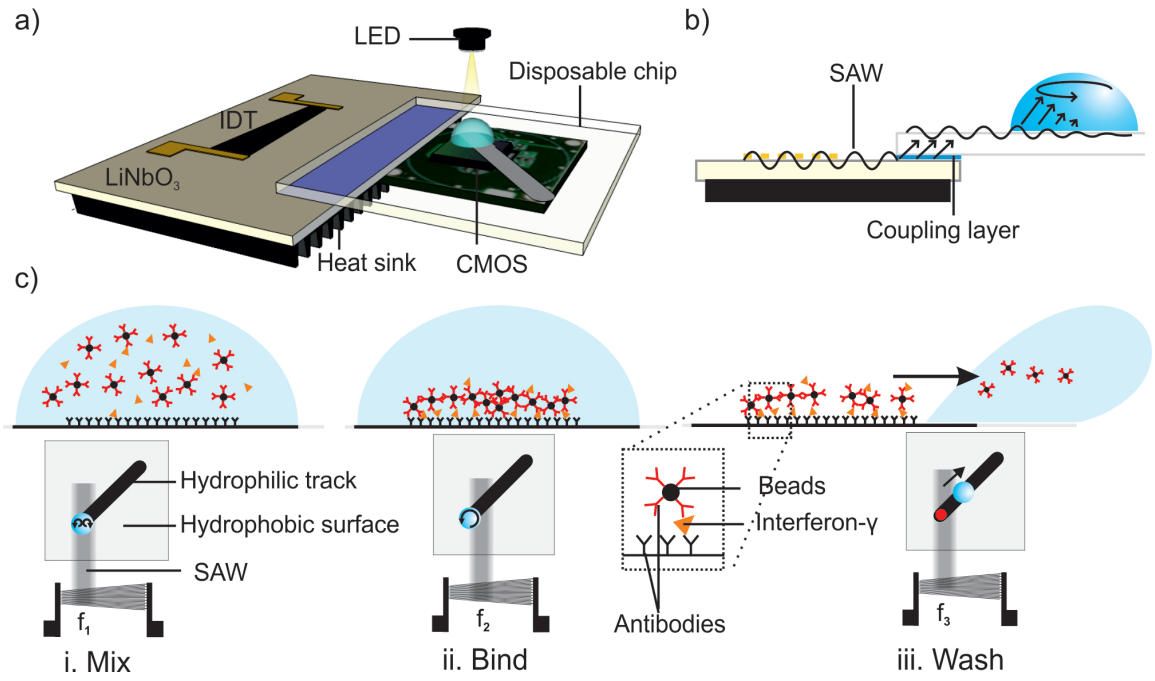

Figure 6.1: (a) Schematic of the device comprising an IDT on lithium niobate ($LiNbO_3$), a disposable chip and a CMOS camera. (b) The SAWs were generated by the electrodes and propagated on the piezoelectric surface; the waves were coupled into the chip through a thin layer of water-based gel and refracted into the droplet resulting in fluid movement. c) Representation of the different steps of the immunoassay starting with (i) capture of the antigen by the beads with frequency f_1, where the acoustic waves interacted with the drop in a symmetrical manner, leading to mixing flows; (ii) binding of the beads on the surface with frequency f_2, for which the acoustic waves interacted only with the right-hand side of the drop, creating an angular momentum which results in particle concentration in the centre of the drop, near the surface; and (iii) the SAW wash with frequency f_3 before detection, where the acoustic power was such that the drop moves with the unbound beads preferentially on the hydrophilic track provided.

device. An Agilent Technologies MXG Analog Signal Generator N5181A was used in conjunction with a Mini Circuits ZHL-5W-1, 5500 MHz amplifier and a 3 A, ±24 V DC power supply to power the SAW device.

The performance of the slanted IDT was characterized using a Network Analyzer (Agilent Technologies E5071C ENA series) and the position of the aperture with the frequency was calibrated using a TiS Thermal Imaging Scanner (Fluke), (Figure 6.2a).

Coupling

Water has previously been used as a coupling solution between the superstrate and substrate [11], although, in this case, it is not suitable as it evaporates rapidly, leading to uncertainties in the extent of coupling over time.

To investigate the efficacy, stability and reproducibility of the coupling, the amplitude of the signal transmitted into a superstrate of lithium niobate with an IDT was measured. The S_{21}-parameter was measured over several minutes for 10 repetitions, Figure 6.2b. In order to achieve a reproducible coupling, a defined amount of coupling agent was deposited on the substrate before positioning the superstrate on a delimited place marked on the lithium niobate. The measurements showed that KY jelly, which is a water-based gel, was the most appropriate coupling agent as it was stable over at least 25 min with coefficients of variation under 5% during the first 10 min. The coupling with water provided more power in the first 5 min, but it showed a decrease in efficiency of about 75% after only 8 min, which would not sustain the assay, lasting 10 min, and the coefficients of variation are up to 15% which would not allow reproducible measurments.

The temperature of the droplet containing the buffer solution was measured throughout the assay. As shown in Figure 6.2c, the temperature was stable during the whole assay and remained under 28 °C.

Disposable chip

The chip contained a hydrophilic track surrounded by a hydrophobic surface (Figure 6.1c). Monoclonal antibodies were covalently bound onto a defined 3 mm diameter spot at the end of the track (Figure 6.1a). The disposable superstrate was fabricated using glass coverslips (22 x 22 mm, 0.17 mm thick, Menzel-Gläser). A pattern comprising a diagonal channel (width 3 mm, length 20 mm, angle 45°) was made using the technique described in Section 3.1.4

Antibodies were immobilized on the coverslip at one side of the hydrophilic track using the method described in Section 3.3.1. It consisted in the silanization of the surface, covalently bounding the antibodies using glutaraldehyde and blocking the surface.

Beads

Latex beads, 2 μm in diameter, polystyrene carboxylate-modified, were coupled with antibodies using a method similar to the one-step coating procedure described by Molecular Probes (Invitrogen), as described in Section 3.3.2. In brief, EDC reacts with carboxylic acid group, allowing it to be coupled to the amino groups on the antibodies.

Sandwich immunoassay

A sandwich immunoassay was designed in which all of the assay steps were controlled by the ability of the tuneable SAW to manipulate the fluid and particles therein. A sample containing the analyte, human interferon-γ (Sigma Aldrich, I3265), was deposited on the spot of antibodies on surface of the superstrate (Fig.ure 6.1c). Using SAW streaming (f_1 = 13.2 MHz, 320 mW, 30 s), the functionalized beads were rapidly mixed. In the second step, the input frequency was adjusted so as to create an angular momentum in the droplet (f_2 = 12.12 MHz, 320 mW, 570 s), which led to the concentration of the beads near the surface towards the centre of the droplet, where the glass was covered by the second antibody, enhancing the binding of beads on the surface. Finally, a SAW wash, using a third frequency excited at a higher power (f_3 = 13.4 MHz, 500 mW, 10 s), enabled us to move the fluid with the non-bound beads away, along a hydrophilic track. The remaining beads, bound to the surface through an anti-interferon-interferon ligand binding, were then detected optically and counted.

6.2.2 Microscope detection

In a microscope configuration, the objective was positioned directly under the superstrate, as shown in Figure 6.3a. Single beads can be easily detected as shown in Figure 6.3b (Ex 475 nm, Em 535 nm). The results of the counts, calculated using ImageJ software, was sensitive down to the detection of a single bead. It has a major advantage compared to conventional fluorescent techniques where the intensity is detected because it is not affected by variation of pH or instrumental noise. This technique is however not suited to a low cost diagnostic device as the instrumentation required is

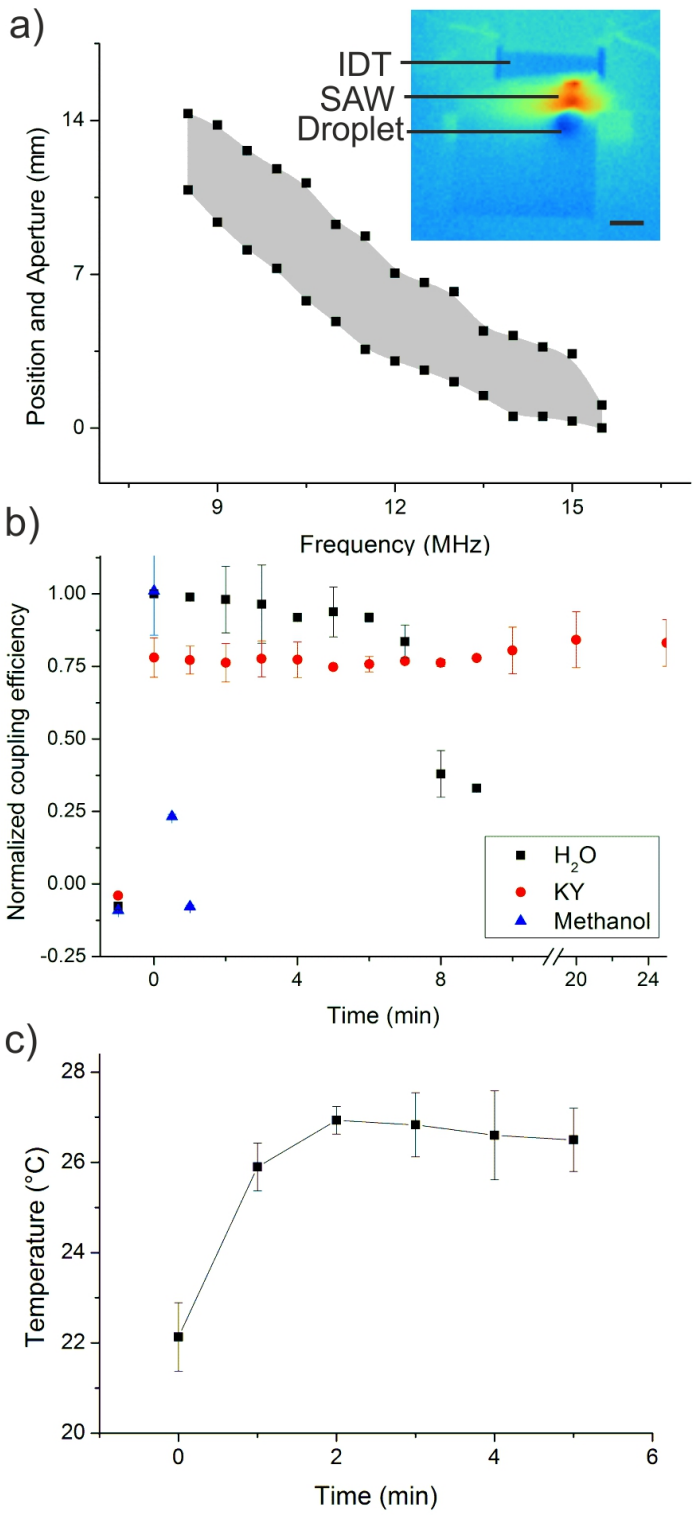

Figure 6.2: (a) Aperture and position of the signal as a function of the input frequency and image of the setup taken with an infrared camera. The position and the aperture of the SAW are visible due to the heating of the gel between the piezoelectric substrate and the chip. The aperture was measured by taking the FWHM of the heated surface. Scale bar is 5 mm. (b) Coupling efficiency as a function of the time for different coupling agent (normalized on H_2O). The results are obtained by measuring the S_{21} -parameter of the signal generated by the device and transmitted into a superstrate of lithium niobate with a receiver IDT. c) Temperature control of the droplet during the assay.

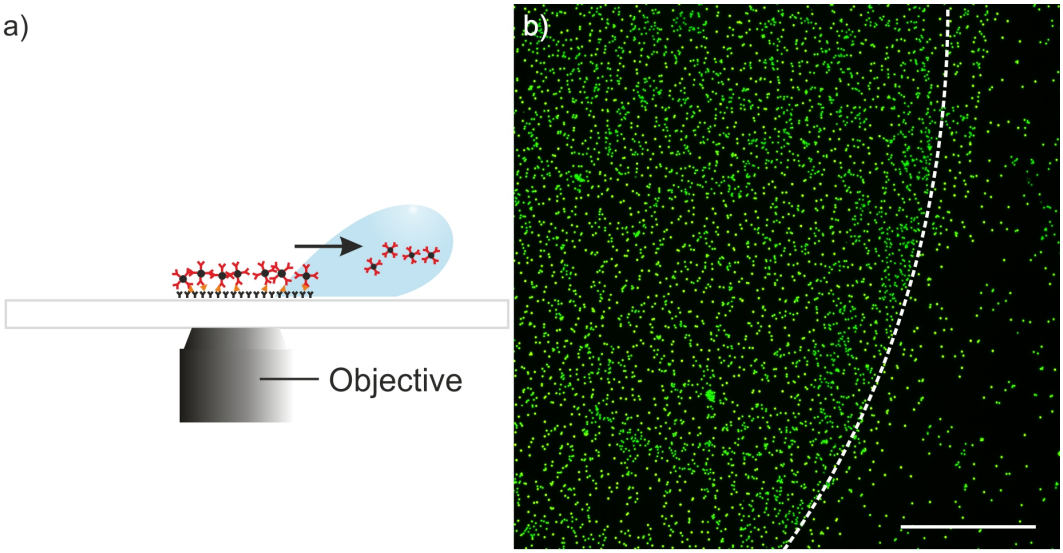

Figure 6.3: (a) Schematic of the detection technique using fluorescent microscopy. (b) Image obtained with the fluorescent microscopy showing the spot of the specifically bound beads on the left side and non-specificaly bound beads on the right side. The dashed line shows the limit of the spot. The scale bar is 100 μm.

expensive.

6.2.3 Lensfree detection

In the lensfree configuration (Figure 6.1a), we used a CMOS camera with a resolution of 640 x 480 pixels (surface = 2.3 mm x 3 mm, pixel size = 4.7 μm) positioned directly under the superstrate, as shown in Figure 6.4a. The LED of a mobile phone was used to illuminate the sample. This technique is suited to a low cost diagnostic device as the instrumentation required is inexpensive and available in many mobile phones. Single beads can be detected as shown in Figure 6.4b and results of the counts, calculated using ImageJ software, correlated linearly with standard fluorescent microscopy (Figure 6.4c). The 2 μm beads appear approximately 10 times larger than their actual size on the CMOS detector for a distance of 200 μm between the sensing surface and the CMOS. It can be calculated that the image would be fully covered for a concentration of beads of 0.32 beads/100 μm^2, as the distance between beads on the surface was smaller than their virtual diameter. Experimentally, single beads could not be resolved for concentrations higher than 0.37 beads/100 μm^2.

6.2.4 Beads counting

An automatic method was used to count the beads on the surface using ImageJ. The lensfree or fluorescent microscopy images were first converted into a grayscale image

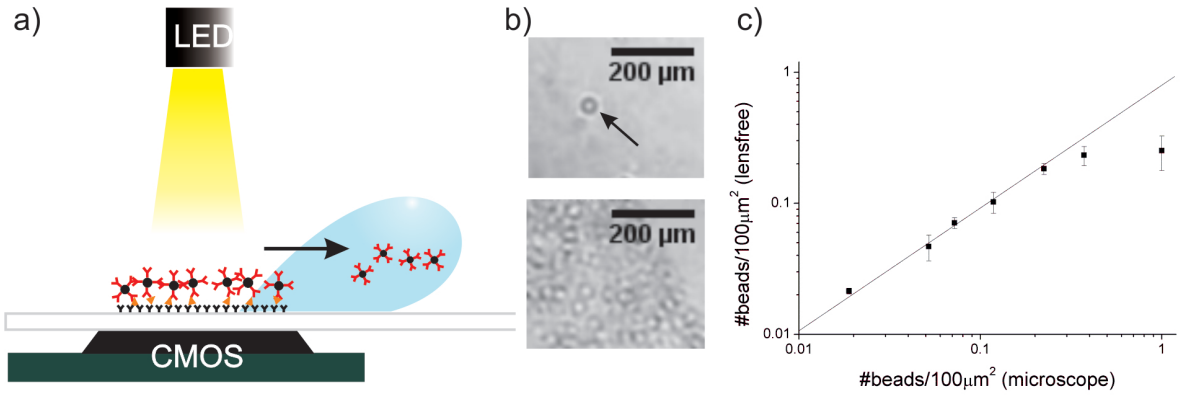

Figure 6.4: (a) Schematic of the detection technique. Light was emitted from the LED towards the chip. The beads bound to the surface scattered the light and a shadow image was recorded with the CMOS camera. (b) The top picture shows a typical image of a low number of 2 μm beads recorded with the CMOS demonstrating the ability to detect a single bead, while the bottom picture is representative of a high number of beads at saturation. (c) Correlation between the lensfree detection and fluorescence microscopy, represented by the number of beads counted with the lensfree detection against the number of beads on the surface counted using fluorescence microscopy. The line (y = x) represented a perfect correlation and is drawn to help visualisation. The relationship is linear until a density of 0.37 beads/100 μm^2, above which less beads were detected with the lensfree technique than with the fluorescence microscope. Error bars are standard deviation.

(8 bits) and the region of interest selected. A threshold was applied to transform the beads into black dots. In the case of the lensfree image, the function "fill holes" was used after the threshold as the image of the bead could be a ring. The watershed function was applied to create a separation between the beads too close to each other. The function "analyse particles" was used to count the number of black dots in the image.

6.3 Results and Discussion

The effect of the actuation of beads using SAW in our assay was investigated. Figure 6.5a shows a comparison between an assay using SAW and an assay without SAW (where beads were sedimented on the surface). In both cases, after 5 min, a washing step was performed by manually rinsing the cartridges in PBS. For 50 pM of interferon-γ, the signal was significantly higher when SAW actuation was used. As the SAW interacted only partially with the droplet at the frequency, f_2 (12.12 MHz), an angular momentum was induced in the fluid resulting in the concentration of the beads near the surface, increasing the efficacy of binding. In addition, streaming increased mixing, whilst the large surface area, afforded by the beads, made the capture kinetics of

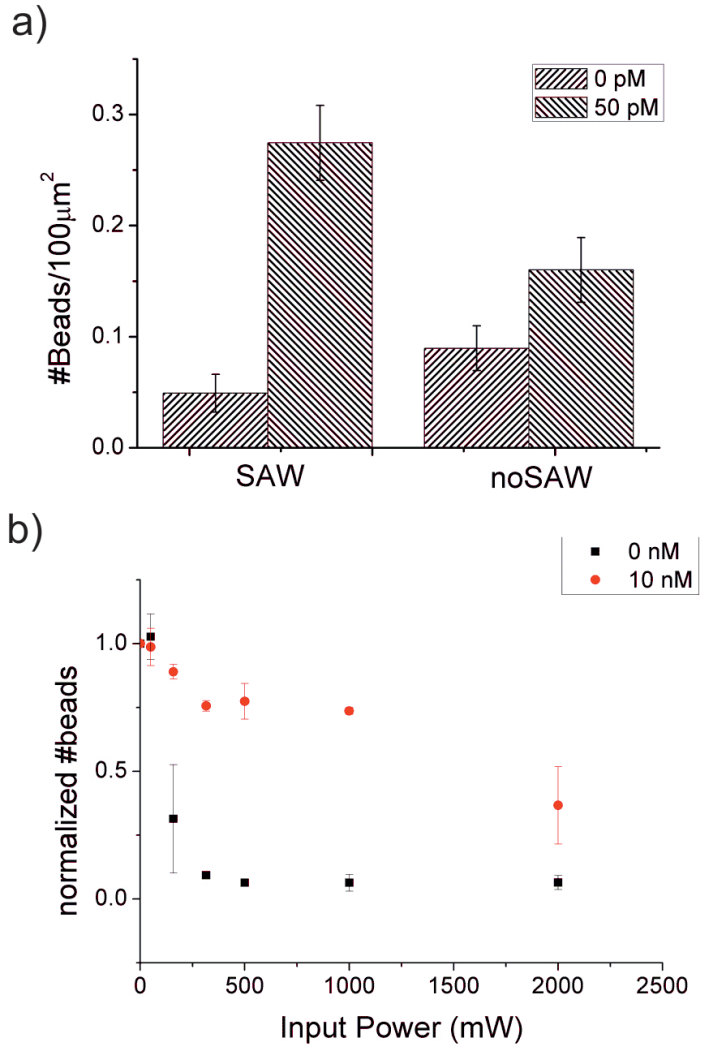

Figure 6.5: (a) Concentration of beads on the surface with SAW or without SAW actuation for 0 pM of interferon-γ (non-specific binding) and for 50 pM interferon-γ. The sample containing wet beads and analytes was deposited on the cartridge and the SAW excited for 5 min before rinsing with PBS 1X (frequency f_2, 12.12 MHz, 320 mW). The use of SAW increased the binding kinetics and lowered non-specific binding. (b) Number of beads on surface (normalized to 0 mW) as a function of the input power. Cartridges were incubated with wet beads and analytes for 2 h to allow binding. A quick (10 s) washing step was performed with SAW at different input powers (cartridges were further manually rinsed in PBS 1X). For 0 nM (non-specific binding), the beads were removed from the surface at an input power of ~320 mW. For 10 nM, only some of the beads were removed at 320 mW, while most of the beads were removed at 2000 mW. Error bars are standard deviation.

the analyte more favourable. When no analyte was present (0 pM, only non-specific binding), the number of beads bound on the surface after washing was significantly lower with SAW than when the beads were sedimenting (only).

In order to further explore the nature of the non-specific binding, an assay in which beads and analyte (0 nM or 10 nM) were incubated on the cartridge for 2 h (Figure 6.5b) was performed. The samples were then actuated with SAW for 10 s using different input powers (each cartridge was further manually rinsed in PBS 1X as the drops did not move away for powers below 400 mW) and the concentration of beads on the surface counted. For 0 nM, ∼90% of the beads were removed from the surface using an input power above 320 mW. For 10 nM, only ∼30% of the beads were removed for input powers between 320 mW and 1 W, whilst more than ∼50% were removed when raising the input power to 2 W. This shows that the SAW was able to remove non-specific binding at low powers, whilst specific binding is only compromised at higher power. The ratio of specifically bound beads to the total number of beads on the surface was 0.98 for input power between 320 mW and 1 W, while it was 0.80 without using SAW.

The reduction of the non-specific binding is mostly due to the force acting on the particles due to the shear flow induced by the SAW streaming. When a stream of fluid flows overa surface, a drag force and a lift force are generated which act to remove a particle from the surface. For micron-size particles in a laminar flow, a modified Stokes law can be used to express the drag force [17]:

$$F_d = 1.7009 * 3\pi\mu d V_p \tag{6.1}$$

where μ is the fluid viscosity, d the diameter of the particle and V_p is the fluid velocity at the center of the particle. The constant 1.7009 accounts for the effect of the wall on the drag force. The lift force is described by [17]:

$$F_l = 1.615\mu d^2 (\frac{\rho}{\mu}\frac{\mathrm{d}u}{\mathrm{d}z})^{1/2} V_p \tag{6.2}$$

where ρ is the fluid density, u the fluid velocity parallel to the surface and z the direction normal to the surface.

This reduction in non-specific binding is a major advantage of the SAW technique and was critical to enable the use of a lens-free detection technique, which saturates at a low threshold (Figure 6.4c).

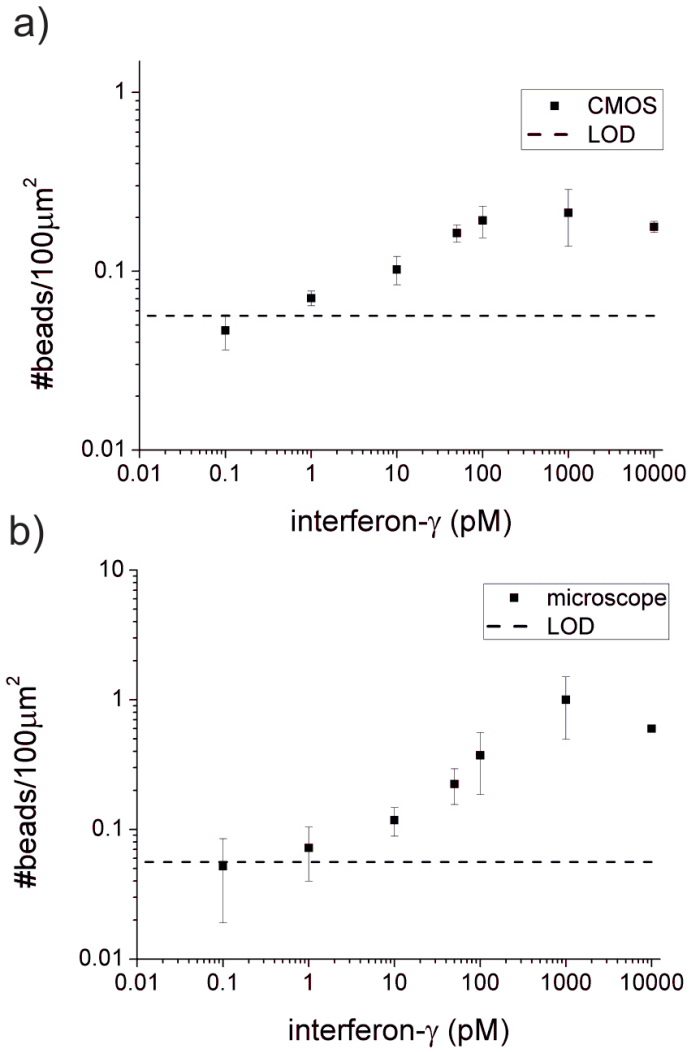

Figure 6.6: (a-b) Sensitivity of the immunoassay on a lensfree detection platform and under fluorescent microscope. Results show the mean of at least 3 repetitions. Error bars are the standard deviation. The limit of detection (LOD) is the background (0 pM) with 3 times the standard deviation. The assay time was 610 s including mixing (f_1 = 13.2 MHz, 320 mW, 30 s), binding (f_2 = 12.12 MHz, 320 mW, 570 s), removing (f_3 = 13.4 MHz, 500 mW, 10 s)

A dose-response curve for interferon-γ is shown in Figure 6.6. The assay was performed using the tuneable SAW technique (total assay time of 610 s). The input power used during the SAW actuation was selected to take advantage of the SAW to reduce non-specific binding without compromising the specific binding during the washing step. The limit of detection, determined as the minimum signal above three-times the standard deviation of the mean background signal, was situated, for both the lensfree and microscope techniques, at 1 pM of interferon-γ, which is the limit required to diagnose tuberculosis in an interferon-γ release assay [83]. In future, this performance could be increased by further reducing the remaining non-specific binding through additional surface chemistries. The measurement range before saturation (1-1000 pM) is through three orders of magnitude of analyte concentration, a figure which is comparable to other bead-based techniques. The error bars, which are the standard deviations of 3 repetitions, demonstrate the reproducibility of the whole assay, from the coupling, the immobilization of antibodies and actuation. The coefficients of variation, which are the ratio between the standard deviation and the mean, are below 15%. It is likely that a major part of it is due to the coupling as the power transmitted can vary by 5%, which would in turn increase or decrease the mixing. The reproducibility of the system could be improved by setting the thickness of the coupling layer (e.g. using microbeads) and by calculating the amount of energy reflected and transmitted and correcting the input power accordingly.

6.4 Conclusion

An integrated biosensor using technologies commonly found in mobile phones such as surface acoustic wave transducers, a CMOS camera and a LED was developed. The use of SAW enhanced the binding kinetics while reducing non-specific binding. This technique showed a high sensitivity with good reproducibility on a low cost disposable chip. The ability of the tuneable SAW to drive complex fluidic functions has the potential to allow the development of more complex assay such as the interferon-γ release assay used in the diagnostics of tuberculosis.

Chapter 7

Enrichment of malaria iRBCs

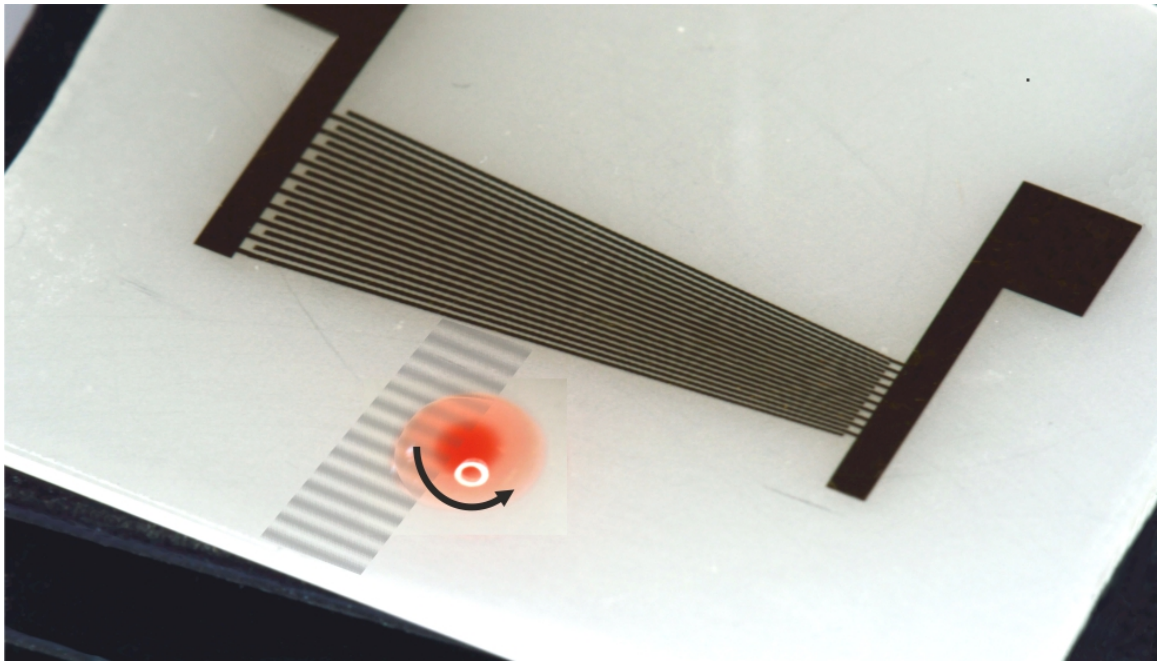

In this Chapter, a method to enrich malaria infected RBCs using tuneable SAW and isopycnic gradient density is demonstrated. After a short introduction, the principle of the technique is described and results showing the enrichment of malaria infected RBCs are presented.

7.1 Introduction

Malaria continues to kill many hundreds of thousands of people each year and is a significant burden on the socio economic development of many countries [115, 145]. *Plasmodium falciparum* is the most deadly of the five species of Plasmodium known to infect man. After many years of international policy aimed at containing the disease, it has recently become an explicit aim to move towards the elimination of malaria [32]. However, if this

is to occur it will be important to have diagnostic tools to ensure infected individuals are found and treated [7].

The gold standard for the diagnosis of malaria remains the direct microscopic observation of the parasites in a Giemsa stained blood sample. This approach requires a laboratory setting, specialized technicians and is time consuming (>1 hour). The limit of detection using a thin blood smear is around 100 parasites μl^{-1} and for a thick blood film this improves to 5-20 parasites μl^{-1} [89]. Rapid diagnostic tests based upon antigen capture have proven useful in endemic settings where microscopy is not available, but such techniques are not sufficiently reliably able to detect low parasitaemias (below 200 parasites μl^{-1})[79, 1]. A large number of patients with low parasitemia are therefore not diagnosed or treated properly.

Microfluidics and lab-on-a-chip (LOC) devices have the potential to bring diagnostic assays from centralized laboratory settings to POC and could enable rapid implementation into resource-limited settings in developing countries [160, 159, 21].

It is well established that *Plasmodium falciparum* changes the physical properties of iRBCs, altering their surface biochemistry, elasticity, volume and density [120, 87, 130], causing the majority of iRBCs to be sequestered in deeper tissues, where it is unavailable for POC testing using a fingerprick. The ring stage does however circulate in the iRBC and it is only this stage that can be detected in a blood sample [120, 87, 130]. The first efforts to exploit these properties in diagnostic devices have been reported using microfluidic channels and dielectrophoresis [54, 39], but only the quantitative buffy coat (QBC) test has been commercialized (albeit with little success in the field due to the relatively cost of implementing this technique) [130].

In this Chapter, the development of a microseparation technique based on a SAW actuated microchip (Figure 7.1a) for the enrichment of *P. falciparum*-iRBCs is reported. The technique is based on the unique flow patterns that can be generated by SAWs, in a microdroplet, which when coupled with an isopycnic density gradient result in the separation of iRBCs from RBCs (Figure 7.1b-c). Only 10 μl of blood (equivalent to that sampled by a fingerprick) are required without the need for tubes, pumps or classical centrifuge devices.

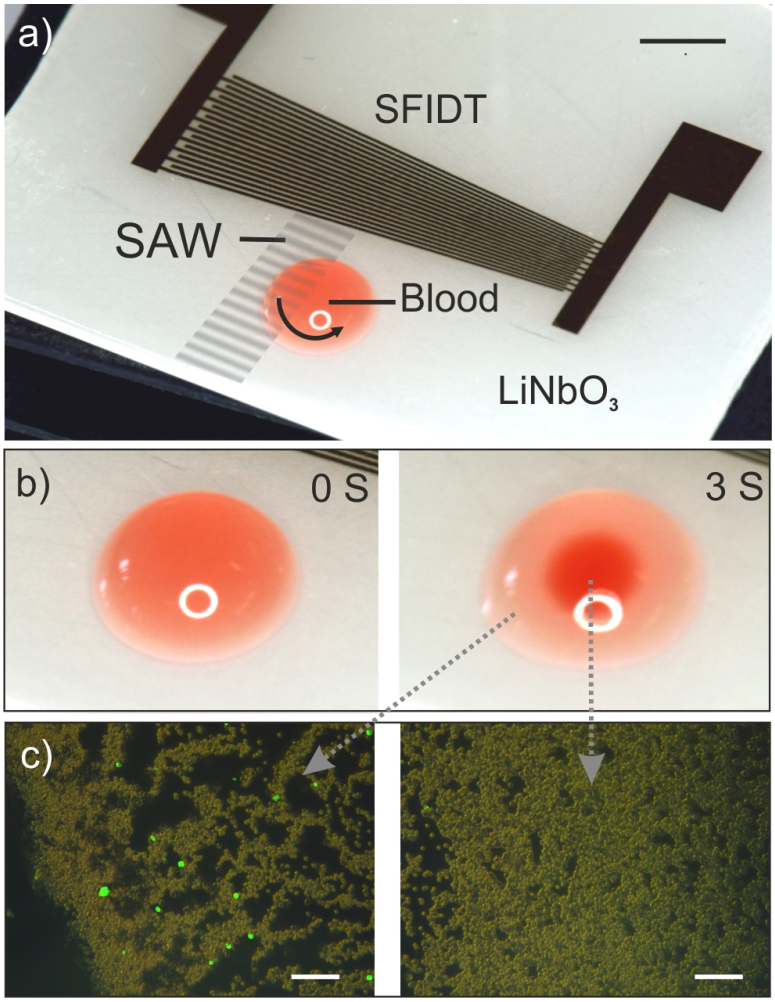

Figure 7.1: (a) Picture of the device comprising a SFIDT on $LiNbO_3$. The SAW was generated at a defined position asymmetrically with respect to the drop of blood, so that only part of the drop is in the acoustic pathway, thereby inducing a rotational motion within it. Scale bar is 3 mm.(b) Pictures of the concentration of RBCs before (left) and after (right) actuation with SAW. RBCs are concentrated in the middle of the drop, while infected iRBCs are enriched at the periphery. (c) Fluorescent images of the enriched iRBCs at the periphery (left) and concentration of RBCs in the center of the drop (right). To obtain these images, the blood was diluted (1:100 in RMPI), acridine orange (1.5 μg ml^{-1}) was added to the solution to stain the parasites and the droplet dried after the SAW actuation. Scale bars are 100 μm.

7.2 Experimental

The SAW isopycnic microseparation

The technology relies on optimising the flow patterns in the context of the density of the medium. The particular flow pattern was generated by the use of surface acoustic wave streaming in a droplet lying on the surface of the piezoelectric substrate. By asymmetrically actuating the droplet with the SAW (Figure 7.1a), a circular streaming motion was generated within the droplet as discussed in Chapter 4.1. This circular motion induced a secondary flow, illustrated in Figure 7.2, traveling inward along the bottom surface and bringing the particles or RBCs to the centre of the droplet. Under normal circumstances, the drag force is not strong enough to lift up the particles. The centripetal effect obtained here was counter-intuitively different from centrifugation expected in a rotational motion. Moreover, separation of particles with different densities, commonly achieved in a centrifuge, has not been demonstrated with SAW streaming.

The separation of particles of different density does not occur spontaneously within the fluid itself. Gradient index products are commonly used in biology to separate different cell types by classical centrifugation. Here, an isopycnic gradient approach was adapted, although the mechanism of generating the gradient was new. As particles collect at the centre of the drop, the drag force generated by the secondary flow was too weak to lift the particles as described in Figure 7.2. Increasing the power would lead to cell lysis [109]. By adjusting the density of the solution such that it was higher than the density of the particle, the buoyancy becomes sufficiently strong to invert the resultant force, allowing an isopycnic separation, as described in Figure 7.2. In order to separate malaria iRBCs, the density of the solution was tuned to be higher than that of the iRBCs but lower than that of the RBCs; the resultant force was strong enough to lift the iRBCs, but not the RBCs. The RBCs were thus concentrated in the middle of the droplet while the iRBCs were enriched at the periphery. The enriched material can be easily isolated for further analysis.

SAW device

The SAW device was fabricated on a 128° Y-cut X-propagating 3 inch $LiNbO_3$ wafer. It consisted of 10 pairs of fingers to form a slanted finger interdigitated transducer (SFIDT). The width of the tapered fingers and the space between them varied linearly from 62.5 μm to 125 μm along the aperture. The SAW device was fabricated using

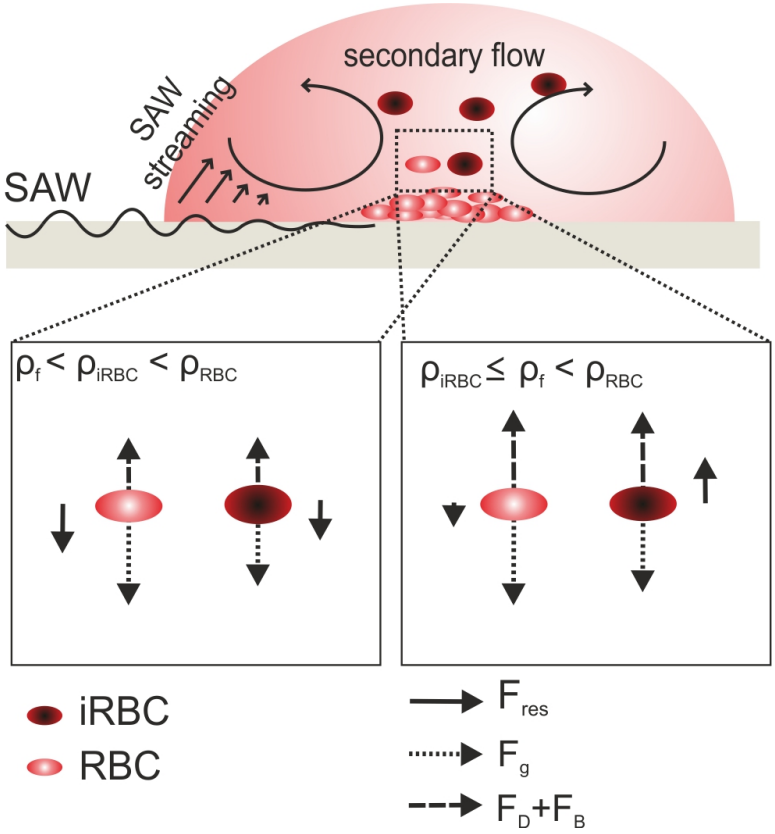

Figure 7.2: Schematic representation of the flow pattern in the droplet. The SAW induced streaming in the drop and a secondary flow brings the particles at the centre of the drop. The two lower schematics show the forces acting on the RBCs and iRBCs for different value of ρ_f. When $\rho_{iRBC} \leq \rho_f < \rho_{RBC}$, the resultant force F_{res} is strong enough to lift the iRBCs but not the RBCs.

Table 7.1: Density value for concentrations of Histodenz™and Optiprep™.

Product	Concentration (%)	Density (g cm^{-3})
Histodenz™in RPMI	0	1.006
	10	1.057
	15	1.083
	20	1.108
Optiprep™in DI water	30	1.160

the method described in Section 3.1.2. For the observation of fluorescent beads and parasites stained with acridine orange, the electrodes where patterned on a transparent double side polished $LiNbO_3$ wafer.

A hydrophilic spot (r = 1.5 mm) was created in front of the IDT to reproducibly position the blood using the method described in Section 3.1.4. The SAW device was finally positioned on a heat sink.

The SAW device was characterized using a Network Analyzer (Agilent Technologies E5071C ENA series) and a vibrometer (Polytec). The SFIDT was connected to a TGR1040-1GHz Synthesised RF Generator (Thurlby Thandar Instruments) in conjunction with a Mini Circuits ZHL-5W-1, 5 - 500 MHz amplifier and a 3A, 24V DC power supply to generate the SAW.

Density solutions

The gradient solutions used were Optiprep™(Sigma-Aldrich) and Histodenz™(Sigma-Aldrich). For experiments with beads, Optiprep was mixed with deionized water to a concentration of 30% leading to a density of 1.160 g cm^{-3}. For the experiments with infected red blood cells, Histodenz™was diluted in deionized water to a concentration of 30% in order to have a high density solution with osmolarity of 300 mOsm. This solution was then further diluted in the culture medium. The density of the solution was measured using DA-510 (Kyoto Electronics Manufacturing) and the osmolarity was determined using The Advanced Micro Osmometer Model no. 3300 (Advanced Instruments Inc). The density for Optiprep 30% was 1.160 g cm^{-3}, while Histodenz 0%, 10%, 15%, 20% in RPMI were 1.006, 1.057, 1.083, 1.108 g cm^{-3} respectively as shown in Table 7.1.

iRBCs preparation and enrichment

P. falciparum clone were prepared according to the method reported in Section 3.4. Parasites were tightly synchronised to obtain ring-stage parasites. Thin blood smears

were prepared and stained with 5% Giemsa's stain for 40 minutes and examined under 1000x magnification (oil immersion), with a minimum of 100 parasites counted to obtain an accurate estimate of parasitaemia. Serial dilutions were performed using uninfected human blood in culture medium (RPMI1640 with 10% human serum) as the diluent, from that in the culture (2.4%) down to a final parasitaemia of 0.0005%.

The infected blood was mixed with the density gradient solutions to a final percentage of RBCs of 2% in each experiment. The blood (10 μl) was then pipetted on to the SAW device. The SAW was turned on for 3 seconds for the separation and the outer part of the droplet was pipetted out. A thin smear was then created from this solution and stained using 5% Giemsa staining for 40 min. The number of parasites was counted under microscope as above. For the experiments with fluorescence, 10 μl of acridine orange (stock solution of 0.15 mg ml^{-1}) was added to 1 ml of infected blood before the SAW process and the resulting solution was directly observed under a fluorescent microscope (Ex 480, Em 535).

7.3 Results and Discussion

Beads separation

To verify the general working principle and have a visual insight of the behaviour of the particles, 5 μm silica red fluorescent beads (ρ = 2 g cm^{-3}) and 5 μm polystyrene green fluorescent beads (ρ= 1.05 g cm^{-3}) were mixed together and the density of the solution was tuned to ρ = 1 g cm^{-3} (H_2O) and ρ = 1.160 g cm^{-3} (30% Optiprep^{TM}). As shown in Figure 7.3a, both types of bead were collected in the center of the drop for ρ = 1 g cm^{-3}, while in Figure 7.3b, for ρ = 1.160 g cm^{-3}, the silica beads were collected in the middle and the polystyrene beads were dispersed at the periphery.

Enrichment of *P. falciparum*-infected erythrocytes

The enrichment of *P. falciparum*-iRBCs was first characterized by using infected blood containing all asexual stages of the parasite. A study of the optimal density was made by varying the concentration of gradient solution. The densities of *P. falciparum* iRBCs (1.077 - 1.080 g cm^{-3}) are lower than those of the RBCs (1.080 - 1.110 g cm^{-3}) [44]. Common isopycnic gradient generating agents exist including Percoll^{TM}, Ficoll^{TM}, Optiprep^{TM}and Histodenz^{TM}. Histodenz^{TM}was preferred here against Optiprep^{TM}for its low viscosity, non-toxicity and relatively low osmolarity. A maximum of 30 %

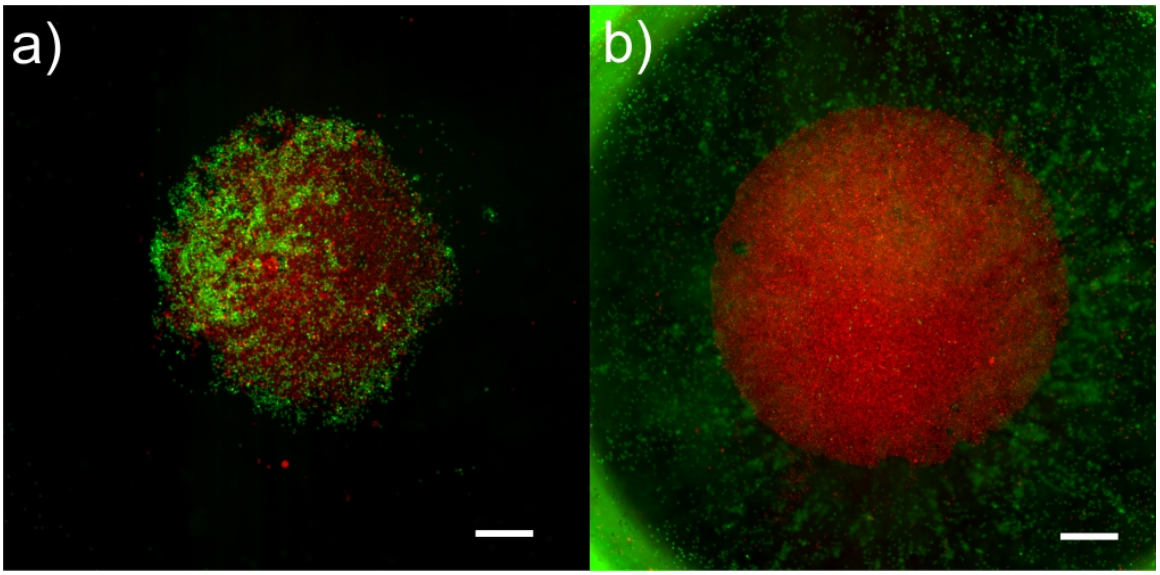

Figure 7.3: Fluorescent picture of 5 μm silica (red) and 5 μm polystyrene (green) particles after SAW actuation for (a) $\rho = 1$ g cm^{-3} and (b) $\rho = 1.160$ g cm^{-3}. In (a), both particles were collected in the middle, while in (b) the polystyrene beads were spread at the periphery. Scale bars are 300 μm.

Histodenz^{TM}maintained osmolarity at around 300 mOsm and solutions with densities between 1.05 - 1.11 g cm^{-3} were prepared with the osmolarity set at 300 mOsm.

Results of separations are shown in Figure 7.4a, where densities between 1.05 and 1.11 g cm^{-3} were tested for frequencies of 10 and 33 MHz. For densities above 1.08 g cm^{-3}, a clear enrichment of parasite-iRBCs was obtained, consistent with the minimal density of a healthy RBC being around 1.08 g cm^{-3}, with iRBCs being less dense. Intriguingly, the enrichment of iRBCs still occurred at higher densities, when it would be expected that both RBCs and iRBCs would be dispersed to the periphery above a certain threshold. This is probably due to the fact that the density of RBCs increases progressively with age and there is a constraint to use transfusion blood of up to 7 days post-bleed. This threshold was not reached as the density of the solution was limited to keep the osmolarity around 300 mOsm. There are no significant differences between the two frequencies. Only at a density of 1.05 g cm^{-3}, enrichment can be observed for 33 MHz but not for 10 MHz, which may just be due to a stronger streaming within the droplet due to the faster dissipation of energy at higher frequency.

In order to optimise separation of iRBC from RBCs, the effect of the power rating was then investigated as shown in Figure 7.4b. Enrichment increased proportionally to power until it reached a maximum around 125 mW. The increase in power affected the streaming velocity of the fluid within the droplet with a critical velocity required to create sufficient drag force to lift the iRBCs. Stronger streams, generated at power outputs of >250 mW were sufficient to lift healthy RBCs as well as iRBC, which

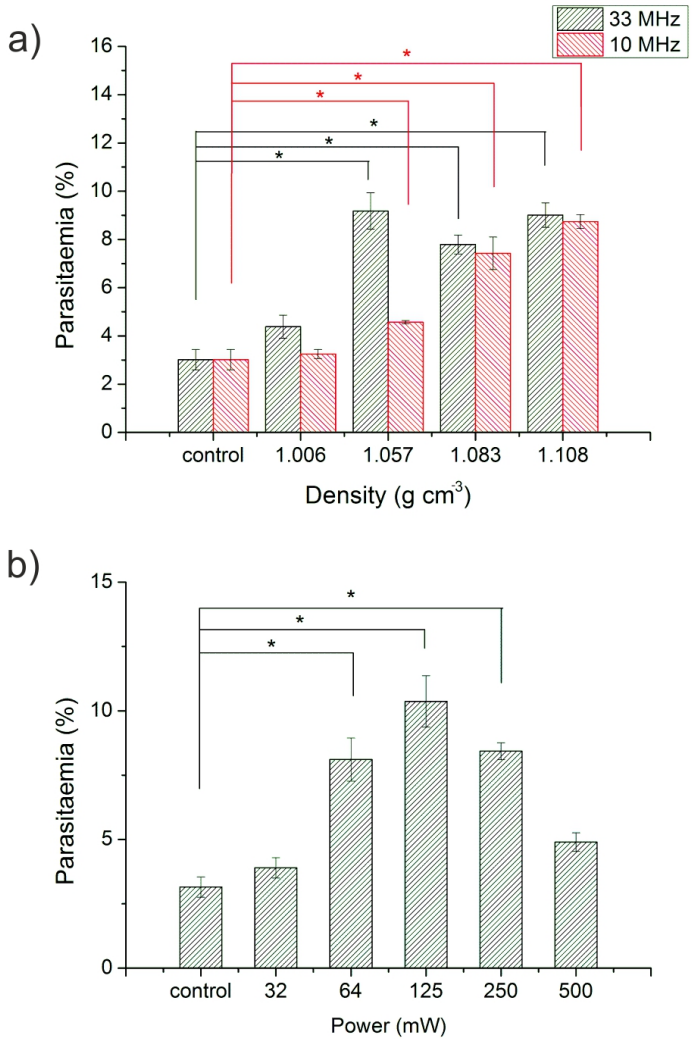

Figure 7.4: (a) The concentration effect of SAW microseparation on *P. falciparum* parasites suspended in Histodenz as a function of the density of the solution (SAW input frequency of 10 MHz and 33 MHz, power of 100 mW). Control indicates the parasitaemia in the sample used prior to SAW microseparation, and the other points are the parasitaemia recorded in samples taken from the periphery of the droplet following SAW microseparation. The data are means of 9 replicates with standard errors of the mean. Statistically significant enrichments are marked with * (95%). (b) The effect of the input power on the enrichment of P. falciparum for a frequency of 10 MHz and solution density of 1.083 g cm^{-3}.

reduced the degree of enrichment.

Enrichment of ring stage of *P. falciparum*-infected erythrocytes

The enrichment methods described above involved an unsynchronised culture of *P. falciparum*. However, in patients, only the ring stage of *P. falciparum* is detectable in the bloodstream, other forms sequestering to vascular endothelia. Hence it is the specific behaviour of the ring stage that will be relevant in developing a diagnostic device. We therefore investigated further the behaviour of ring-stage parasites in the SAW microseparation device. Parasites were synchronised to ring stage only in culture. Several densities were tested at a frequency of 10 MHz and a power of 100 mW as shown in Figure 7.5a. A clear enrichment of the parasites was obtained for densities above 1.08 g cm^{-3}. The enrichment obtained was similar to that obtained using unsynchronised cultures containing all stages of the parasites.

Finally, the limit of detection was investigated to judge its ability to detect low parasitemia (down to 0.0005% of red cells infected) common in infections in malaria-endemic regions. As the initial parasitaemia decreased, the enrichment increased up to 100-fold (Figure 7.5b), allowing the detection of parasitized red cells in a culture at a parasitaemia of 0.0005% (25 parasites μl^{-1}), which is lower than the current limit of detection using a thin smear.

7.4 Conclusion

Here, a novel method was demonstrated for the enrichment of all the stages of *Plasmodium*-iRBCs including the ring stage using a SAW-based isopycnic method. The technique offers a significant enhancement in diagnostic sensitivity over classical microscopy as a means to diagnose the disease. Most simply, enriched samples could be Giemsa-stained and examined microscopically, or the enrichment could be coupled with fluorescent staining of the parasites, and direct examination on the SAW-device. The increasing availability of cheap and easy-to-use LED-based fluorescence microscopes is also facilitating the diagnosis of numerous infectious diseases and the method described here would work alongside LED-based field fluorescence microscopes and lensfree sytsems. This device has the potential to enter use in malaria-endemic areas where very low parasitemia is very common and under the limit of detection of classical microscopy techniques.

Moreover, due to its versatility, low power consumption and portable size, this

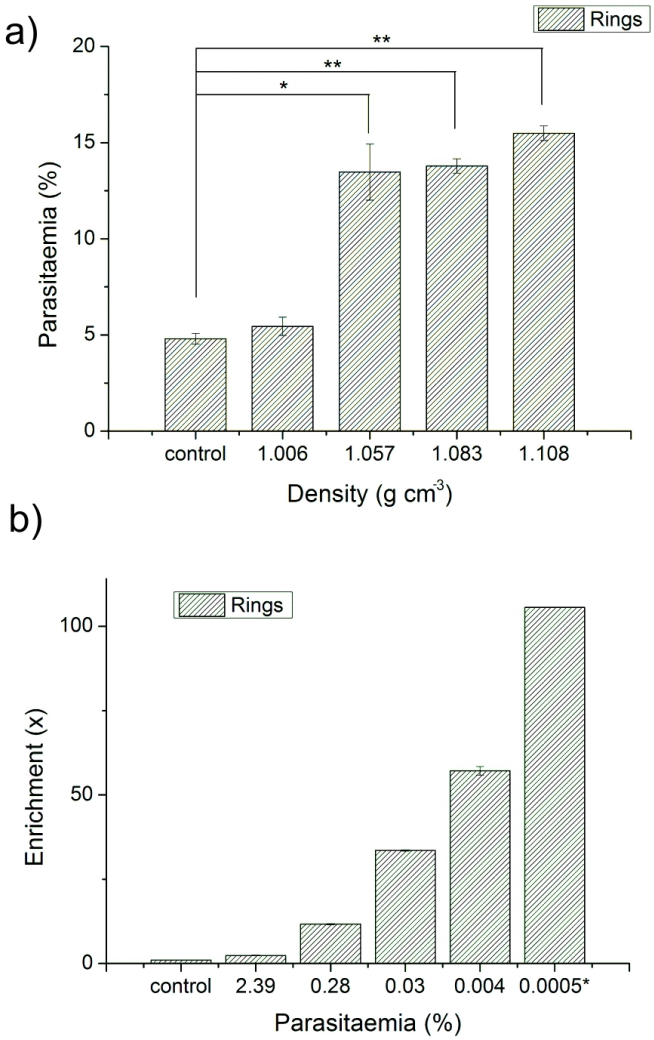

Figure 7.5: (a) The concentration effect of SAW microseparation on P. falciparum ring-stage parasites suspended in Histodenz as a function of the density of the solution for a frequency of 10 MHz and power of 100 mW. Control indicates the parasitaemia in the sample used prior to SAW microseparation. Parasitaemias were determined by Giemsa-staining and microscopy in samples taken from the periphery of the droplet following SAW microseparation. The data are means of 9 replicates and the error bars are standard errors of the mean deviations. Statistically significant enrichments are marked with * (95%) and ** (99%). (b) The fold enrichment achieved following SAW microseparation of samples containing ring-stage parasites at parasitemias from 2.39% to 0.0005% in Histodenz at 15% (ρ=1.08326 g cm^{-3}), input frequency of 10 MHz and power of 100 mW. (*the control for 0.0005 % parasitemia was extrapolated from the dilutions as it was impossible to determine the parasitaemia by microscopy at such low concentration in a thin smear).

method could also be applied to other infectious diseases of the blood, including human African trypanosomiasis, leishmaniasis, microfilarial infections, or to the detection of cancer cells which have also been reported to have densities that distinguish them from normal cells.

Chapter 8

Conclusion and Outlook

In this final Chapter, an overall conclusion is drawn and future paths of the research are proposed.

8.1 General conclusion

A new microfluidic platform, based on SAW, was developped to reduce the dependence of the diagnostic procedure on large laboratory instruments and provide simplicity of use, enabling samples to be processed and diagnosed on a low cost, disposable biochip.

By shaping the SAW using particular designs of electrodes and phononic structures, the control of the positions and amplitudes of the waves required to create complex microfluidc functions was achieved:

- The lateral positioning of the SAW was demonstrated using a slanted finger IDT in a frequency tuneable manner allowing microfluidic function such as mixing, moving and merging, sequentially performed using a single IDT.
- Phononic bandgaps were designed to break the symmetry of the SAW in a tuneable manner.
- GRIN-PC lenses were designed to focus the SAW and successfully increased the amplitude of the wave by a factor 3 while the focal position could be tuned with the frequency.

The potential of SAW techniques in other applications were further demonstrated:

- The amplitude and direction of water jet towers were controlled by shaping the waves on the surface using a phononic strucutre.

- A macrometer scale vehicle was propulsed in water and its direction was controlled using tuneable SAWs.

As a proof of concept of a diagnostic device for the developing world using shaped SAWs:

- An immunoassay for TB was developped using only mobile phone technologies (SAW, LED, CMOS) where all the microfluidic steps (mixing, binding, washing) were performed using tuneable SAWs. The SAWs also allowed the reduction of non-specifc binding, which lowered the detection limit to 1 pM of IFN-γ, which is the limit required in IFN-γ release assay.

- A method to enrich *P. falciparum* infected cells in a microdroplet was demonstrated, using a SAW isopycnic technology. It showed enrichment up to 100x of the ring stage of malaria, in the equivalent of a fingerprick of blood, and has the potential to lower the limit of detection of the current techniques.

8.2 Outlook

The fields of diagnostics and microfluidics have been growing rapidly over the last decade. The techniques developed in this thesis may open new perspectives in these fields. Here, an outlook is given on possible topics that may lead to significant impact.

8.2.1 Towards POC

As introduced in this thesis, SAW devices are wildly used in mobile phones. An immunoassay and a micro separating device have been developed using mobile phone technologies (SAW, CMOS, LED). Mobile phones can be cheap and are available worldwide. In fact, there are around 620 million mobile phones in Africa [45]. Moreover, the recent technological evolution have led to devices that possess notably a microprocessor, a touch screen, a camera, a battery, connecting ports and a versatile operating system.

Although it is not likely that one could control the SAW devices integrated in a mobile phones, the technology required to power a SAW device is available in a mobile phone and this latter could be used to control an external device and analyse data. Moreover, recent works have shown the development of microscope directly integrated on a customized mobile phone [137] using a method similar to the one used in the

Figure 8.1: A lensfree cellphone microscope which operates based on incoherent in-line holography is shown. The additional hardware installed on the cellphone is composed of a LED in front of the source. This cellphone microscope does not utilize any lens or other bulky optical components. The samples to be imaged are loaded from the side through a mechanical sample holder (Tseng, 2010).

immunoassay developed here confirming the great potential of using mobile phone technologies for POC diagnostics [168].

8.2.2 Acoustophoresis

Optical tweezers are so far the most developed and precise single cell manipulation tool. However, they are complex and require expensive optical setup, limiting their accessibility. Moreover, the energy required by the focused laser to trap a particle is so high that heating can cause permanent damage to biological objects. Recently, the field of acoustophoresis has raised significant interest. It has been established that objects in a standing acoustic field will experience an acoustic radiation force that pushes them toward the pressure nodes or anti-nodes of the standing field, depending on the physical properties of the object and the surrounding medium. Several studies have used this phenomenon to move particles in order to separate them by size or to trap a particle [100].

The acoustic pressure nodes were initially created by generating acoustic waves using simple piezoelectric materials and a reflector. In this case, the boundary conditions

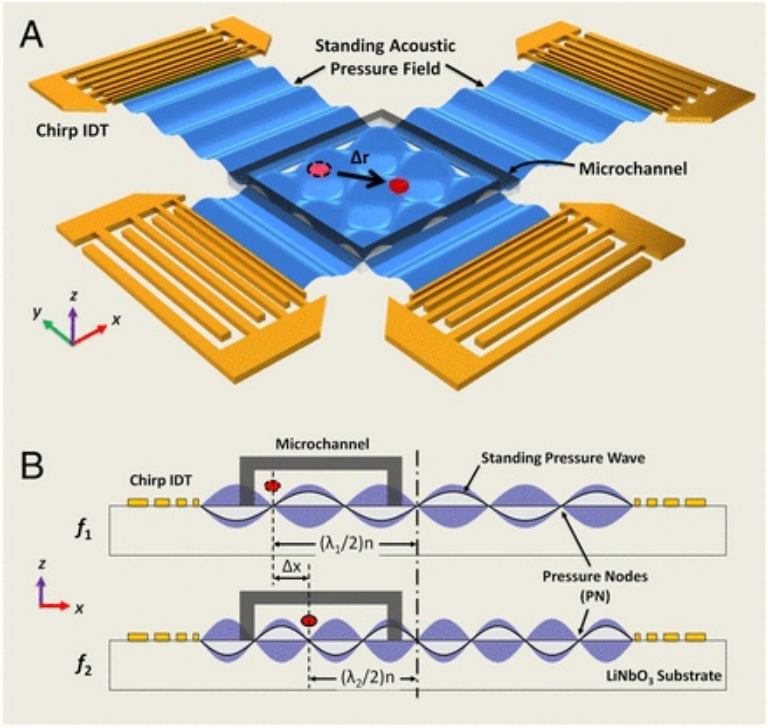

Figure 8.2: Working mechanism of acoustic tweezers, using SAW. (a) Schematic illustrating a microfluidic device with orthogonal pairs of chirped IDTs for generating standing SAW. (b) A standing SAW field generated by driving chirped IDTs at frequency f_1 and f_2. When particles are trapped at the pressure node, they can be translated by switching from f_1 to f_2. (Ding, 2012)

are of great importance. More recently, standing SAWs have been proposed as an alternative. In this case, standing SAWs are generated on the piezoelectric surface using interdigitated electrodes and a chamber is positioned directly on top of the substrate using soft lithography so that the acoustic field on the surface of the substrate define the position of the nodes [73].

The tuneable surface acoustic waves technique developed in this thesis has been adapted to control the position of the beads by tuning the frequency, hence the position of the nodes [27]. This technology has been further developed to manipulate single particles as shown in Figure 8.2 [26]. It is likely that the added level of control provided by phononic crystals will have an impact in acoustophoresis.

8.2.3 Tuneable phononic crystals

In this thesis, phononic crystals made of holes in silicon were presented demonstrating another level of control of the waves. Recently, a great interest in the field of phononics lies with the development of tuneable phononic crystals.

By changing the nature of the phononic crystals, it would be possible to control the bandgap or the group velocity of the wave in a controllable manner. Techniques have

been proposed but they remain theoretical. They rely either on the ability to change the lattice constant [42, 71], for example, or by modifying the Youngs modulus of a material by thermal or electrical input [112].

A practical realization of these techniques would allow the creation of a system that could impact acoustic microfluidics and acoustophoresis in a similar way than holograms have impacted the field of optics through optical tweezers.

Bibliography

[1] K. Abba, J. J. Deeks, P. Olliaro, C.-M. Naing, S. M. Jackson, Y. Takwoingi, S. Donegan, and P. Garner. Rapid diagnostic tests for diagnosing uncomplicated p. falciparum malaria in endemic countries. *Cochrane Database Syst Rev*, (7):CD008122, 2011.

[2] E. M. Allison, G. S. Springer, and J. V. Dam. Ultrasonic propulsion. *AIAA Journal of Propulsion and Power*, 24(3):547–553, 2008.

[3] M. Alvarez, J. Friend, and L. Yeo. Rapid generation of protein aerosols and nanoparticles via surface acoustic wave atomization. *Nanotechnology*, 19(45):455103, 2008.

[4] M. Alvarez, J. R. Friend, and L. Y. Yeo. Surface vibration induced spatial ordering of periodic polymer patterns on a substrate. *Langmuir*, 24(19):10629–10632, 2008.

[5] P. F. Barnes. Diagnosing latent tuberculosis infection. *American Journal of Respiratory and Critical Care Medicine*, 170(1):5–6, 2004.

[6] G. K. Batchelor. Note on a class of solutions of the navier-stokes equations representing steady rotationally-symmetric flow. *Q J Mechanics Appl Math*, 4(1):29–41, 1951.

[7] D. Bell, C. Wongsrichanalai, and J. W. Barnwell. Ensuring quality and access for malaria diagnosis: how can it be achieved? *Nat Rev Microbiol*, 4:S7–20, 2006.

[8] S. Benchabane, A. Khelif, J. Y. Rauch, L. Robert, and V. Laude. Evidence for complete surface wave band gap in a piezoelectric phononic crystal. *Physical Review E*, 73(6):065601, 2006.

[9] H. Bertoni and T. Tamir. Unified theory of rayleigh-angle phenomena for acoustic beams at liquid-solid interfaces. *Applied Physics A: Materials Science & Processing*, 2(4):157–172, 1973.

[10] D. Beyssen, L. Le Brizoual, O. Elmazria, and P. Alnot. Microfluidic device based on surface acoustic wave. *Sensors and Actuators B: Chemical*, 118(1-2):380–385, 2006.

[11] Y. Bourquin, J. Reboud, R. Wilson, and J. M. Cooper. Tuneable surface acoustic waves for fluid and particle manipulations on disposable chips. *Lab on a Chip*, 10(15):1898–1901, 2010.

[12] Y. Bourquin, J. Reboud, R. Wilson, Y. Zhang, and J. M. Cooper. Integrated immunoassay using tuneable surface acoustic waves and lensfree detection. *Lab on a Chip*, 11(16):2725–2730, 2011.

[13] Y. Bourquin, R. Wilson, Y. Zhang, J. Reboud, and J. M. Cooper. Phononic crystals for shaping fluids. *Advanced Materials*, 23(12):1458–1462, 2011.

[14] H. Bow, I. V. Pivkin, M. Diez-Silva, S. J. Goldfless, M. Dao, J. C. Niles, S. Suresh, and J. Han. A microfabricated deformability-based flow cytometer with application to malaria. *Lab Chip*, 11(6):1065–1073, 2011.

[15] D. M. Bruls, T. H. Evers, J. A. H. Kahlman, P. J. W. van Lankvelt, M. Ovsyanko, E. G. M. Pelssers, J. J. H. B. Schleipen, F. K. de Theije, C. A. Verschuren, T. van der Wijk, J. B. A. van Zon, W. U. Dittmer, A. H. J. Immink, J. H. Nieuwenhuis, and M. W. J. Prins. Rapid integrated biosensor for multiplexed immunoassays based on actuated magnetic nanoparticles. *Lab on a Chip*, 9(24):3504–3510, 2009.

[16] P. Brunet, M. Baudoin, O. B. Matar, and F. Zoueshtiagh. Droplet displacements and oscillations induced by ultrasonic surface acoustic waves: a quantitative study. *Phys Rev E Stat Nonlin Soft Matter Phys*, 81:036315, 2010.

[17] G. Burdick, N. Berman, and S. Beaudoin. Describing hydrodynamic particle removal from surfaces using the particle reynolds number. *Journal of Nanoparticle Research*, 3:453–465, 2001.

[18] F. Cervera, L. Sanchis, J. V. Sanchez-Perez, R. Martinez-Sala, C. Rubio, F. Meseguer, C. Lopez, D. Caballero, and J. Sanchez-Dehesa. Refractive acoustic devices for airborne sound. *Physical Review Letters*, 88(2):023902, 2001.

[19] Z. Chen, S. M. Tabakman, A. P. Goodwin, M. G. Kattah, D. Daranciang, X. Wang, G. Zhang, X. Li, Z. Liu, P. J. Utz, K. Jiang, S. Fan, and H. Dai. Protein microarrays with carbon nanotubes as multicolor raman labels. *Nat Biotech*, 26(11):1285–1292, 2008. 10.1038/nbt.1501.

[20] W. Cheng, J. Wang, U. Jonas, G. Fytas, and N. Stefanou. Observation and tuning of hypersonic bandgaps in colloidal crystals. *Nat Mater*, 5(10):830–836, 2006.

[21] C. D. Chin, T. Laksanasopin, Y. K. Cheung, D. Steinmiller, V. Linder, H. Parsa, J. Wang, H. Moore, R. Rouse, G. Umviligihozo, E. Karita, L. Mwambarangwe, S. L. Braunstein, J. van de Wijgert, R. Sahabo, J. E. Justman, W. El-Sadr, and S. K. Sia. Microfluidics-based diagnostics of infectious diseases in the developing world. *Nat Med*, 17(8):1015–1019, 2011.

[22] K. Chono, N. Shimizu, Y. Matsui, J. Kondoh, and S. Shiokawa. Development of novel atomization system based on saw streaming. *Japanese Journal of Applied Physics*, 43:2987, 2004.

[23] S. C. Cowin and J. W. Nunziato. Linear elastic materials with voids. *Journal of Elasticity*, 13:125–147, 1983. 10.1007/BF00041230.

[24] S. Cular, D. W. Branch, V. R. Bhethanabotla, G. D. Meyer, and H. G. Craighead. Removal of nonspecifically bound proteins on microarrays using surface acoustic waves. *Sensors Journal, IEEE*, 8(3):314–320, 2008.

[25] S. Datta. *Surface acoustic wave devices*. Prentice Hall, 1986.

[26] X. Ding, S.-C. S. Lin, B. Kiraly, H. Yue, S. Li, I.-K. Chiang, J. Shi, S. J. Benkovic, and T. J. Huang. On-chip manipulation of single microparticles, cells, and organisms using surface acoustic waves. *Proc Natl Acad Sci U S A*, 109(28):11105–11109, 2012.

[27] X. Ding, J. Shi, S.-C. S. Lin, S. Yazdi, B. Kiraly, and T. J. Huang. Tunable patterning of microparticles and cells using standing surface acoustic waves. *Lab Chip*, 12:2491–2497, 2012.

[28] C. Eckart. Vortices and streams caused by sound waves. *Phys. Rev.*, 73:68–76, 1948.

[29] J. Eggers. Nonlinear dynamics and breakup of free-surface flows. *Reviews of Modern Physics*, 69(3):865, 1997.

[30] K. M. Ehlers and J. Koiller. Could cell membranes produce acoustic streaming? making the case for synechococcus self-propulsion. *Mathematical and Computer Modelling*, 53(7-8):1489–1504, 2011.

[31] K. M. Ehlers, A. D. Samuel, H. C. Berg, and R. Montgomery. Do cyanobacteria swim using traveling surface waves? *Proceedings of the National Academy of Sciences*, 93(16):8340–8343, 1996.

[32] I. Fong. Challenges in the control and eradication of malaria. In I. Fong, editor, *Challenges in Infectious Diseases*, Emerging Infectious Diseases of the 21st Century, pages 203–231. Springer New York, 2013.

[33] T. Franke, A. R. Abate, D. A. Weitz, and A. Wixforth. Surface acoustic wave (saw) directed droplet flow in microfluidics for pdms devices. *Lab Chip*, 9(18):2625–2627, 2009.

[34] T. Franke, S. Braunmller, L. Schmid, A. Wixforth, and D. A. Weitz. Surface acoustic wave actuated cell sorting (sawacs). *Lab Chip*, 10(6):789–794, 2010.

[35] T. A. Franke and A. Wixforth. Microfluidics for miniaturized laboratories on a chip. *ChemPhysChem*, 9(15):2140–2156, 2008.

[36] J. Friend and L. Y. Yeo. Microscale acoustofluidics: Microfluidics driven via acoustics and ultrasonics. *Reviews of Modern Physics*, 83(2):647, 2011.

[37] T. Frommelt, D. Gogel, M. Kostur, P. Talkner, P. Hanggi, and A. Wixforth. Flow patterns and transport in rayleigh surface acoustic wave streaming: combined finite element method and raytracing numerics versus experiments. *Ultrasonics, Ferroelectrics and Frequency Control, IEEE Transactions on*, 55(10):2298–2305, 2008.

[38] E. Galopin, M. Beaugeois, B. Pinchemel, J.-C. Camart, M. Bouazaoui, and V. Thomy. Spr biosensing coupled to a digital microfluidic microstreaming system. *Biosensors and Bioelectronics*, 23(5):746–750, 2007.

[39] P. Gascoyne, C. Mahidol, M. Ruchirawat, J. Satayavivad, P. Watcharasit, and F. F. Becker. Microsample preparation by dielectrophoresis: isolation of malaria. *Lab Chip*, 2(2):70–75, 2002.

[40] L. Gervais, N. de Rooij, and E. Delamarche. Microfluidic chips for point-of-care immunodiagnostics. *Advanced Materials*, 23(24):H151–H176, 2011.

[41] H. Getahun, C. Gunneberg, R. Granich, and P. Nunn. Hiv infection-associated tuberculosis: the epidemiology and the response. *Clin Infect Dis*, 50 Suppl 3:S201–S207, 2010.

[42] C. Goffaux and J. P. Vigneron. Theoretical study of a tunable phononic band gap system. *Phys. Rev. B*, 64:075118, 2001.

[43] J. Gordon and G. Michel. Analytical sensitivity limits for lateral flow immunoassays. *Clinical Chemistry*, 54(7):1250–1251, 2008.

[44] W. H. Grover, A. K. Bryan, M. Diez-Silva, S. Suresh, J. M. Higgins, and S. R. Manalis. Measuring single-cell density. *Proc Natl Acad Sci U S A*, 108(27):10992–10996, 2011.

[45] GSMA. *African Mobile Observatory 2011*. GSM Association, 2011.

[46] C. Guinovart, M. M. Navia, M. Tanner, and P. L. Alonso. Malaria: Burden of disease. *Current Molecular Medicine*, 6:137–140, 2006.

[47] Z. Guttenberg, H. Muller, H. Habermuller, A. Geisbauer, J. Pipper, J. Felbel, M. Kielpinski, J. Scriba, and A. Wixforth. Planar chip device for pcr and hybridization with surface acoustic wave pump. *Lab on a Chip*, 5(3):308–317, 2005.

[48] S. R. Heron, R. Wilson, S. A. Shaffer, D. R. Goodlett, and J. M. Cooper. Surface acoustic wave nebulization of peptides as a microfluidic interface for mass spectrometry. *Analytical Chemistry*, 82(10):3985–3989, 2010.

[49] A. C. Hesseling, M. F. Cotton, T. Jennings, A. Whitelaw, L. F. Johnson, B. Eley, P. Roux, P. Godfrey-Faussett, and H. S. Schaaf. High incidence of tuberculosis among hiv-infected infants: evidence from a south african population-based study highlights the need for improved tuberculosis control strategies. *Clin Infect Dis*, 48(1):108–114, 2009.

[50] J. Ho, M. K. Tan, D. B. Go, L. Y. Yeo, J. R. Friend, and H.-C. Chang. Paper-based microfluidic surface acoustic wave sample delivery and ionization source for rapid and sensitive ambient mass spectrometry. *Analytical Chemistry*, 83(9):3260–3266, 2011.

[51] R. P. Hodgson, M. Tan, L. Yeo, and J. Friend. Transmitting high power rf acoustic radiation via fluid couplants into superstrates for microfluidics. *Applied Physics Letters*, 94(2):024102, 2009.

[52] Y. Hongyu and K. Eun Sok. Ultrasonic underwater thruster. In *Micro Electro Mechanical Systems, 17th IEEE International Conference on.*, pages 486–489, 2004.

[53] K. Hori, T. Miyagawa, and K. Ito. Development of ultra-small sized servo actuator with brushless dc motor, planetary gear drive and optical rotary encoder. *Int. J. Japan Soc. Precis. Eng.*, 31:1, 1997.

[54] H. W. Hou, A. A. S. Bhagat, A. G. L. Chong, P. Mao, K. S. W. Tan, J. Han, and C. T. Lim. Deformability based cell margination–a simple microfluidic design for malaria-infected erythrocyte separation. *Lab Chip*, 10(19):2605–2613, 2010.

[55] M. Jassal and W. R. Bishai. Extensively drug-resistant tuberculosis. *Lancet Infect Dis*, 9(1):19–30, 2009.

[56] M. Jepsen, T. G. Krause, D. Moryl, N. Seersholm, M. Ruhwald, B. Sborg, I. Brock, and P. Ravn. Comparison of quantiferon and tuberculin skin test in possible suspected tuberculosis infection. *Ugeskr Laeger*, 171(37):2625–2631, 2009.

[57] M. Ke, Z. Liu, C. Qiu, W. Wang, J. Shi, W. Wen, and P. Sheng. Negative-refraction imaging with two-dimensional phononic crystals. *Phys. Rev. B*, 72:064306, 2005.

[58] A. Khelif, B. Aoubiza, S. Mohammadi, A. Adibi, and V. Laude. Complete band gaps in two-dimensional phononic crystal slabs. *Phys. Rev. E*, 74:046610, 2006.

[59] J.-W. Kim, Y. Yamagata, M. Takasaki, B.-H. Lee, H. Ohmori, and T. Higuchi. A device for fabricating protein chips by using a surface acoustic wave atomizer and electrostatic deposition. *Sensors and Actuators B: Chemical*, 107(2):535–545, 2005.

[60] J. Kondoh, N. Shimizu, Y. Matsui, and S. Shiokawa. Liquid heating effects by saw streaming on the piezoelectric substrate. *Ultrasonics, Ferroelectrics and Frequency Control, IEEE Transactions on*, 52(10):1881–1883, 2005.

[61] J. Kondoh, N. Shimizu, Y. Matsui, M. Sugimoto, and S. Shiokawa. Development of temperature-control system for liquid droplet using surface acoustic wave devices. *Sensors and Actuators A: Physical*, 149(2):292–297, 2009.

[62] N.-K. Kuo, C. Zuo, and G. Piazza. Microscale inverse acoustic band gap structure in aluminum nitride. *Applied Physics Letters*, 95(9):093501, 2009.

[63] M. Kurosawa, T. Watanabe, A. Futami, and T. Higuchi. Surface acoustic wave atomizer. *Sensors and Actuators A: Physical*, 50(1-2):69–74, 1995.

[64] M. S. Kushwaha, P. Halevi, L. Dobrzynski, and B. Djafari-Rouhani. Acoustic band structure of periodic elastic composites. *Physical Review Letters*, 71(13):2022, 1993.

[65] H. Lamb. On waves in an elastic plate. *Proceedings of the Royal Society of London. Series A*, 93(648):114–128, 1917.

[66] V. Laude, D. Gerard, N. Khelfaoui, C. F. Jerez-Hanckes, S. Benchabane, and A. Khelif. Subwavelength focusing of surface acoustic waves generated by an annular interdigital transducer. *Applied Physics Letters*, 92(9):094104, 2008.

[67] V. Laude, L. Robert, W. Daniau, A. Khelif, and S. Ballandras. Surface acoustic wave trapping in a periodic array of mechanical resonators. *Applied Physics Letters*, 89(8):083515–3, 2006.

[68] H. Li, J. Friend, and L. Yeo. Surface acoustic wave concentration of particle and bioparticle suspensions. *Biomedical Microdevices*, 9(5):647–656, 2007.

[69] M. J. Lighthill. Studies on magneto-hydrodynamic waves and other anisotropic wave motions. *Philosophical Transactions of the Royal Society of London. Series A, Mathematical and Physical Sciences*, 252(1014):397–430, 1960.

[70] S. J. Lighthill. Acoustic streaming. *Journal of Sound and Vibration*, 61(3):391 – 418, 1978.

[71] S.-C. S. Lin and T. J. Huang. Tunable phononic crystals with anisotropic inclusions. *Phys. Rev. B*, 83:174303, 2011.

[72] S.-C. S. Lin, T. J. Huang, J.-H. Sun, and T.-T. Wu. Gradient-index phononic crystals. *Physical Review B*, 79(9):094302, 2009.

[73] S.-C. S. Lin, X. Mao, and T. J. Huang. Surface acoustic wave (saw) acoustophoresis: now and beyond. *Lab Chip*, 12:2766–2770, 2012.

[74] A. Martinez, S. Phillips, M. Butte, and G. Whitesides. Patterned paper as a platform for inexpensive, low-volume, portable bioassays. *Angewandte Chemie International Edition*, 46(8):1318–1320, 2007.

[75] A. W. Martinez, S. T. Phillips, and G. M. Whitesides. Three-dimensional microfluidic devices fabricated in layered paper and tape. *Proceedings of the National Academy of Sciences*, 105(50):19606–19611, 2008.

[76] A. W. Martinez, S. T. Phillips, G. M. Whitesides, and E. Carrilho. Diagnostics for the developing world: Microfluidic paper-based analytical devices. *Analytical Chemistry*, 82(1):3–10, 2010. PMID: 20000334.

[77] R. Martinez-Sala, J. Sancho, J. V. Sanchez, V. Gomez, J. Llinares, and F. Meseguer. Sound attenuation by sculpture. *Nature*, 378:241, 1995.

[78] I. M. Mason and E. A. Ash. Acoustic surface-wave beam diffraction on anisotropic substrates. *Journal of Applied Physics*, 42(13):5343–5351, 1971.

[79] M. L. McMorrow, M. Aidoo, and S. P. Kachur. Malaria rapid diagnostic tests in elimination settings–can they find the last parasite? *Clin Microbiol Infect*, 17(11):1624–1631, 2011.

[80] S. Mohammadi, A. A. Eftekhar, A. Khelif, W. D. Hunt, and A. Adibi. Evidence of large high frequency complete phononic band gaps in silicon phononic crystal plates. *Applied Physics Letters*, 92(22):221905, 2008.

[81] D. Morgan. Surface acoustic wave devices and applications: 1. introductory review. *Ultrasonics*, 11(3):121 – 131, 1973.

[82] D. P. Morgan. *Surface acoustic wave filters [electronic resource] : with applications to electronic communications and signal processing.* Elsevier Science & Technology, 2007.

[83] T. Mori, M. Sakatani, F. Yamagishi, T. Takashima, Y. Kawabe, K. Nagao, E. Shigeto, N. Harada, S. Mitarai, M. Okada, K. Suzuki, Y. Inoue,

K. Tsuyuguchi, Y. Sasaki, G. H. Mazurek, and I. Tsuyuguchi. Specific detection of tuberculosis infection: An interferon-gamma-based assay using new antigens. *American Journal of Respiratory and Critical Care Medicine*, 170(1):59–64, 2004.

[84] O. Mudanyali, C. Oztoprak, D. Tseng, A. Erlinger, and A. Ozcan. Detection of waterborne parasites using field-portable and cost-effective lensfree microscopy. *Lab on a Chip*, 10(18):2419–2423, 2010.

[85] V. Mudenda, S. Lucas, A. Shibemba, J. O'Grady, M. Bates, N. Kapata, S. Schwank, P. Mwaba, R. Atun, M. Hoelscher, M. Maeurer, and A. Zumla. Tuberculosis and tuberculosis/hiv/aids-associated mortality in africa: the urgent need to expand and invest in routine and research autopsies. *J Infect Dis*, 205 Suppl 2:S340–S346, 2012.

[86] J.-M. Nam, C. S. Thaxton, and C. A. Mirkin. Nanoparticle-based bio-bar codes for the ultrasensitive detection of proteins. *Science*, 301(5641):1884–1886, 2003.

[87] G. Nash, E. O'Brien, E. Gordon-Smith, and J. Dormandy. Abnormalities in the mechanical properties of red blood cells caused by plasmodium falciparum. *Blood*, 74(2):855–861, 1989.

[88] W. Nyborg. *Acoustic Streaming*. Academic Press, New York, 1965.

[89] L. B. Ochola, P. Vounatsou, T. Smith, M. L. H. Mabaso, and C. R. J. C. Newton. The reliability of diagnostic techniques in the diagnosis and management of malaria in the absence of a gold standard. *Lancet Infect Dis*, 6(9):582–588, 2006.

[90] R. H. Olsson and I. El-Kady. Microfabricated phononic crystal devices and applications. *Measurement Science and Technology*, 20(1):012002, 2009.

[91] J. L. Osborn, B. Lutz, E. Fu, P. Kauffman, D. Y. Stevens, and P. Yager. Microfluidics without pumps: reinventing the t-sensor and h-filter in paper networks. *Lab on a Chip*, 10(20):2659–2665, 2010.

[92] S. J. Osterfeld, H. Yu, R. S. Gaster, S. Caramuta, L. Xu, S.-J. Han, D. A. Hall, R. J. Wilson, S. Sun, R. L. White, R. W. Davis, N. Pourmand, and S. X. Wang. Multiplex protein assays based on real-time magnetic nanotag sensing. *Proceedings of the National Academy of Sciences*, 105(52):20637–20640, 2008.

[93] O. Oxlade, K. Schwartzman, and D. Menzies. Interferon-gamma release assays and tb screening in high-income countries: a cost-effectiveness analysis. *The International Journal of Tuberculosis and Lung Disease*, 11(1):16–26, 2007.

[94] A. Ozcan and U. Demirci. Ultra wide-field lens-free monitoring of cells on-chip. *Lab on a Chip*, 8(1):98–106, 2008.

[95] M. Pai, S. Kalantri, and K. Dheda. New tools and emerging technologies for the diagnosis of tuberculosis: part i. latent tuberculosis. *Expert Rev Mol Diagn*, 6(3):413–422, 2006.

[96] M. Pai, L. W. Riley, and J. J. M. Colford. Interferon-[gamma] assays in the immunodiagnosis of tuberculosis: a systematic review. *The Lancet Infectious Diseases*, 4(12):761–776, 2004.

[97] M. Pai, L. W. Riley, and J. M. Colford, Jr. Interferon-gamma assays in the immunodiagnosis of tuberculosis: a systematic review. *Lancet Infect Dis*, 4(12):761–776, 2004.

[98] M. Pai, A. Zwerling, and D. Menzies. Systematic review: T-cell-based assays for the diagnosis of latent tuberculosis infection: an update. *Ann Intern Med*, 149(3):177–184, 2008.

[99] Y. Pennec, B. Djafari-Rouhani, J. O. Vasseur, A. Khelif, and P. A. Deymier. Tunable filtering and demultiplexing in phononic crystals with hollow cylinders. *Phys. Rev. E*, 69:046608, 2004.

[100] F. Petersson, L. berg, A.-M. Swrd-Nilsson, and T. Laurell. Free flow acoustophoresis: microfluidic-based mode of particle and cell separation. *Analytical Chemistry*, 79(14):5117–5123, 2007.

[101] J. Plateau. Recherches exprimentales et thorique sur les figures d'quilibre d'une masse liquide sans pesanteur. *Acad. Sci. Bruxelles Mem.*, 23:5, 1849.

[102] E. Purcell. Life at low reynolds number. *American Journal of Physics*, 1977.

[103] A. Qi, J. R. Friend, L. Y. Yeo, D. A. V. Morton, M. P. McIntosh, and L. Spiccia. Miniature inhalation therapy platform using surface acoustic wave microfluidic atomization. *Lab on a Chip*, 9(15):2184–2193, 2009.

[104] A. Qi, L. Y. Yeo, and J. R. Friend. Interfacial destabilization and atomization driven by surface acoustic waves. *Physics of Fluids*, 20(7):074103–14, 2008.

[105] R. Raghavan, J. Friend, and L. Yeo. Particle concentration via acoustically driven microcentrifugation: micropiv flow visualization and numerical modelling studies. *Microfluidics and Nanofluidics*, 8(1):73–84, 2010.

[106] M. Ramam, A. Malhotra, T. Tejasvi, Y. Manchanda, S. Sharma, R. Mittal, and V. Ramesh. How useful is the mantoux test in the diagnosis of doubtful cases of cutaneous tuberculosis? *Int J Dermatol*, 50(11):1379–1382, 2011.

[107] L. Rayleigh. On the capillary phenomena of jets. *Proceedings of the Royal Society of London*, 29(196-199):71–97, 1879.

[108] L. Rayleigh. On waves propagated along the plane surface of an elastic solid. *Proceedings of the London Mathematical Society*, s1-17(1):4–11, 1885.

[109] J. Reboud, Y. Bourquin, R. Wilson, G. S. Pall, M. Jiwaji, A. R. Pitt, A. Graham, A. P. Waters, and J. M. Cooper. Shaping acoustic fields as a toolset for microfluidic manipulations in diagnostic technologies. *Proceedings of the National Academy of Sciences*, 109(38):15162–15167, 2012.

[110] A. Renaudin, V. Chabot, E. Grondin, V. Aimez, and P. G. Charette. Integrated active mixing and biosensing using surface acoustic waves (saw) and surface plasmon resonance (spr) on a common substrate. *Lab on a Chip*, 10(1):111–115, 2010.

[111] L. Richeldi. An update on the diagnosis of tuberculosis infection. *American Journal of Respiratory and Critical Care Medicine*, 174(7):736–742, 2006.

[112] J.-F. Robillard, O. B. Matar, J. O. Vasseur, P. A. Deymier, M. Stippinger, A.-C. Hladky-Hennion, Y. Pennec, and B. Djafari-Rouhani. Tunable magnetoelastic phononic crystals. *Applied Physics Letters*, 95(12):124104 –124104–3, 2009.

[113] P. R. Rogers, J. R. Friend, and L. Y. Yeo. Exploitation of surface acoustic waves to drive size-dependent microparticle concentration within a droplet. *Lab on a Chip*, 10(21):2979–2985, 2010.

[114] J. S. Rothel and P. Andersen. Diagnosis of latent mycobacterium tuberculosis infection: is the demise of the mantoux test imminent? *Expert Rev Anti Infect Ther*, 3(6):981–993, 2005.

[115] P. Sachs, Jeffrey Malaney. The economic and social burden of malaria. *Nature*, 415:680–685, 2002.

[116] S. Sankaranarayanan, S. Cular, V. R. Bhethanabotla, and B. Joseph. Flow induced by acoustic streaming on surface-acoustic-wave devices and its application in biofouling removal: A computational study and comparisons to experiment. *Physical Review E*, 77(6):066308, 2008.

[117] S. Sankaranarayanan, R. Singh, and V. R. Bhethanabotla. Acoustic streaming induced elimination of nonspecifically bound proteins from a surface acoustic wave biosensor: Mechanism prediction using fluid-structure interaction models. *Journal of Applied Physics*, 108(10):104507–11, 2010.

[118] A. Sano, Y. Matsui, and S. Shiokawa. New manipulator based on surface acoustic wave streaming. *Japanese Journal of Applied Physics*, 37:2979, 1998.

[119] S. Seo, T.-W. Su, D. K. Tseng, A. Erlinger, and A. Ozcan. Lensfree holographic imaging for on-chip cytometry and diagnostics. *Lab on a Chip*, 9(6):777–787, 2009.

[120] J. P. Shelby, J. White, K. Ganesan, P. K. Rathod, and D. T. Chiu. A microfluidic model for single-cell capillary obstruction by plasmodium falciparum-infected erythrocytes. *Proceedings of the National Academy of Sciences of the United States of America*, 100(25):14618–14622, 2003.

[121] R. Shilton, M. K. Tan, L. Y. Yeo, and J. R. Friend. Particle concentration and mixing in microdrops driven by focused surface acoustic waves. *Journal of Applied Physics*, 104(1):014910, 2008.

[122] S. Shiokawa, Y. Matsui, and T. Moriizumi. Experimental study on liquid streaming by saw. *Japanese Journal of Applied Physics*, 28S1:126, 1989.

[123] M. Sigalas and E. N. Economou. Band structure of elastic waves in two dimensional systems. *Solid State Communications*, 86(3):141–143, 1993.

[124] M. J. Sinclair. A high force low area mems thermal actuator. *Seventh Intersociety Conf. on Thermal and Thermomechanical Phenomena in Electronic Systems*, page 127, 2000.

[125] W. Smith, H. Gerard, J. Collins, T. Reeder, and H. Shaw. Interdigital surface wave transducers by use of an equivalent circuit model. *IEEE Trans. Microw. Theory Tech.*, 17, 1969.

[126] K. Sritharan, C. J. Strobl, M. F. Schneider, A. Wixforth, and Z. Guttenberg. Acoustic mixing at low reynold's numbers. *Applied Physics Letters*, 88(5):054102–3, 2006.

[127] C. J. Strobl, Z. von Guttenberg, and A. Wixforth. Nano- and pico-dispensing of fluids on planar substrates using saw. *Ultrasonics, Ferroelectrics and Frequency Control, IEEE Transactions on*, 51(11):1432–1436, 2004.

[128] L. L. Su Y-C and A. P. Pisano. A water-powered osmotic microactuator. *J. Microelectromech. Syst.*, 11(6):736, 2002.

[129] A. Sukhovich, L. Jing, and J. H. Page. Negative refraction and focusing of ultrasound in two-dimensional phononic crystals. *Phys. Rev. B*, 77:014301, 2008.

[130] R. Suwanarusk, B. M. Cooke, A. M. Dondorp, K. Silamut, J. Sattabongkot, N. J. White, and R. Udomsangpetch. The deformability of red blood cells parasitized by plasmodium falciparum and p. vivax. *J Infect Dis*, 189(2):190–194, 2004.

[131] T. L. Szabo. 4 - anisotropic surface acoustic wave diffraction. In W. P. MASON and R. THURSTON, editors, *Physical Acoustics Principles and Methods*, volume 13 of *Physical Acoustics*, pages 79 – 113. Academic Press, 1977.

[132] Y.-C. Tai and R. S. Muller. Ic-processed electrostatic synchronous micromotors. *Sensors and Actuators*, 20(1-2):49–55, 1989.

[133] A. C. H. Tan and F. S. Hover. Thrust and wake characterization in small, robust ultrasonic thrusters. In *OCEANS 2010*, pages 1–9, 2010.

[134] M. K. Tan, J. R. Friend, and L. Y. Yeo. Microparticle collection and concentration via a miniature surface acoustic wave device. *Lab on a Chip*, 7(5):618–625, 2007.

[135] M. K. Tan, J. R. Friend, and L. Y. Yeo. Interfacial jetting phenomena induced by focused surface vibrations. *Physical Review Letters*, 103(2):024501, 2009.

[136] Y. Tanaka and S.-i. Tamura. Surface acoustic waves in two-dimensional periodic elastic structures. *Phys. Rev. B*, 58:7958–7965, 1998.

[137] D. Tseng, O. Mudanyali, C. Oztoprak, S. O. Isikman, I. Sencan, O. Yaglidere, and A. Ozcan. Lensfree microscopy on a cellphone. *Lab on a Chip*, 10(14):1787–1792, 2010.

[138] J. O. Vasseur, P. A. Deymier, B. Chenni, B. Djafari-Rouhani, L. Dobrzynski, and D. Prevost. Experimental and theoretical evidence for the existence of absolute acoustic band gaps in two-dimensional solid phononic crystals. *Phys. Rev. Lett.*, 86:3012–3015, 2001.

[139] I. A. Viktorov. *Rayleigh and Lamb waves: Physical theory and applications*. Plenum Press, 1967.

[140] R. E. Vines, S.-i. Tamura, and J. P. Wolfe. Surface acoustic wave focusing and induced rayleigh waves. *Phys. Rev. Lett.*, 74:2729–2732, 1995.

[141] B. Watson, J. Friend, and L. Yeo. Piezoelectric ultrasonic resonant motor with stator diameter less than 250 m: the proteus motor. *Journal of Micromechanics and Microengineering*, 19(2):022001, 2009.

[142] R. M. White and F. W. Voltmer. Direct piezoelectric coupling to surface elastic waves. *Applied Physics Letters*, 7(12):314–316, 1965.

[143] WHO. *Towards quality testing of malaria rapid diagnostic tests*. WHO Press, 2006.

[144] WHO. *World Health Report 2006, Millenium Goals*. WHO Press, 2006.

[145] WHO. *World Malaria Report 2011*. WHO Press, 2011.

[146] WHO. *Global tuberculosis report 2012*. WHO Press, 2012.

[147] R. Wilson, J. Reboud, Y. Bourquin, S. L. Neale, Y. Zhang, and J. M. Cooper. Phononic crystal structures for acoustically driven microfluidic manipulations. *Lab on a Chip*, 11(2):323–328, 2011.

[148] A. Wixforth, C. Strobl, C. Gauer, A. Toegl, J. Scriba, and Z. v. Guttenberg. Acoustic manipulation of small droplets. *Analytical and Bioanalytical Chemistry*, 379(7):982–991, 2004.

[149] T.-C. Wu, T.-T. Wu, and J.-C. Hsu. Waveguiding and frequency selection of lamb waves in a plate with a periodic stubbed surface. *Physical Review B*, 79(10):104306, 2009.

[150] T.-T. Wu and I.-H. Chang. Actuating and detecting of microdroplet using slanted finger interdigital transducers. *Journal of Applied Physics*, 98(2):024903, 2005.

[151] T.-T. Wu, Y.-T. Chen, J.-H. Sun, S.-C. S. Lin, and T. J. Huang. Focusing of the lowest antisymmetric lamb wave in a gradient-index phononic crystal plate. *Applied Physics Letters*, 98(17):171911, 2011.

[152] T.-T. Wu, J.-C. Hsu, and J.-H. Sun. Phononic plate waves. *Ultrasonics, Ferroelectrics and Frequency Control, IEEE Transactions on*, 58(10):2146 –2161, 2011.

[153] T.-T. Wu, Z.-G. Huang, and S. Lin. Surface and bulk acoustic waves in two-dimensional phononic crystal consisting of materials with general anisotropy. *Phys. Rev. B*, 69:094301, 2004.

[154] T.-T. Wu, H.-T. Tang, Y.-Y. Chen, and P.-L. Liu. Analysis and design of focused interdigital transducers. *IEEE Trans Ultrason Ferroelectr Freq Control*, 52(8):1384–1392, 2005.

[155] T.-T. Wu, H.-T. Tang, Y.-Y. Chen, and P.-L. Liu. Analysis and design of focused interdigital transducers. *Ultrasonics, Ferroelectrics and Frequency Control, IEEE Transactions on*, 52(8):1384 –1392, 2005.

[156] T.-T. Wu, W.-S. Wang, J.-H. Sun, J.-C. Hsu, and Y.-Y. Chen. Utilization of phononic-crystal reflective gratings in a layered surface acoustic wave device. *Applied Physics Letters*, 94(10):101913, 2009.

[157] X. Xia, S. Xing-Meng, and L. Ya-Liang. Evaluating of adhesion property of ulsi interconnect films by the surface acoustic waves. *Chinese Physics Letters*, 27:018502, 2010.

[158] X. Xiao, N. Hata, K. Yamada, and T. Kikkawa. Mechanical properties of periodic porous silica low-k films determined by the twin-transducer surface acoustic wave technique. *Review of Scientific Instruments*, 74(10):4539–4541, 2003.

[159] P. Yager, G. J. Domingo, and J. Gerdes. Point-of-care diagnostics for global health. *Annual Review of Biomedical Engineering*, 10(1):107–144, 2008.

[160] P. Yager, T. Edwards, E. Fu, K. Helton, K. Nelson, M. R. Tam, and B. H. Weigl. Microfluidic diagnostic technologies for global public health. *Nature*, 442(7101):412–418, 2006.

[161] S. Yang, J. H. Page, Z. Liu, M. L. Cowan, C. T. Chan, and P. Sheng. Focusing of sound in a 3d phononic crystal. *Phys. Rev. Lett.*, 93:024301, 2004.

[162] H. Yatsuda, K. Noguchi, and K. Yamanouchi. Surface acoustic wave filter using floating electrode slanted finger unidirectional transducers. *Japanese Journal of Applied Physics*, 39:3041–3044, 2000.

[163] H. Yatsuda and K. Yamanouchi. Automatic computer-aided design of saw filters using slanted finger interdigital transducers. *Ultrasonics, Ferroelectrics and Frequency Control, IEEE Transactions on*, 47(1):140–147, 2000.

[164] L. Y. Yeo and J. R. Friend. Ultrafast microfluidics using surface acoustic waves. *Biomicrofluidics*, 3(1):012002, 2009.

[165] A. Zhang, W. Liu, Z. Jiang, and J. Fei. Rapid concentration of particle and bioparticle suspension based on surface acoustic wave. *Applied Acoustics*, 70(8):1137–1142, 2009.

[166] X. Zhang, T. Jackson, E. Lafond, P. Deymier, and J. Vasseur. Evidence of surface acoustic wave band gaps in the phononic crystals created on thin plates. *Applied Physics Letters*, 88(4):041911–3, 2006.

[167] X. Zhang and Z. Liu. Negative refraction of acoustic waves in two-dimensional phononic crystals. *Applied Physics Letters*, 85(2):341–343, 2004.

[168] H. Zhu, S. O. Isikman, O. Mudanyali, A. Greenbaum, and A. Ozcan. Optical imaging techniques for point-of-care diagnostics. *Lab Chip*, 2013.